LHC EFFECTIVE MODEL FOR OPTICS CORRECTIONS

Measurements and corrections of high-order non-linear optics

Dissertation
zur Erlangung des Doktorgrades
der Naturwissenschaften

Vorgelegt beim Fachbereich Physik
der Johann Wolfgang Goethe-Universität
in Frankfurt am Main

von
Maël Le Garrec
aus Obernai, Elsàss, Frankreich.

Frankfurt am Main 2024
(D30)

Vom Fachbereich Physik der Johann Wolfgang Goethe-Universität als Dissertation angenommen.

Dekan:

Gutachter:

Datum der Disputation:

Abstract

This thesis explores the impact of higher-order magnetic fields on the optics and stability of the Large Hadron Collider at CERN, with a focus on octupolar, decapolar, dodecapolar, and decatetrapolar fields. These fields significantly influence beam dynamics, particularly at injection energy, where precise correction is critical for optimal performance.

A key aspect of the research is the development of correction methods for Resonance Driving Terms (RDTs), crucial for managing dynamic aperture limitations. Additionally, the work addresses discrepancies between measurements and models of beam observables, identifying the major contributors. New corrective strategies for RDTs have led to measurable improvements in beam lifetime and stability.

The findings underscore the importance of accurate modeling and correction of these fields to enhance the LHC's operational efficiency and beam stability.

Extended Summary

The Large Hadron Collider (LHC) at CERN, situated in a 27-kilometer tunnel beneath the Swiss-French border, is the world's largest and most powerful particle accelerator. Its primary mission is to recreate the conditions of the universe just moments after the Big Bang, enabling scientists to explore the fundamental forces and particles that constitute the cosmos. This remarkable facility accelerates protons and heavy ions to nearly the speed of light before colliding them with immense energy, providing profound insights into the building blocks of matter and the fundamental interactions that govern our universe. The LHC represents not only a monumental engineering achievement but also a crucial tool for advancing our understanding of high-energy physics.

Operating such a complex and powerful machine requires overcoming numerous technical challenges, particularly in maintaining the precise control and stability of its particle beams. One significant challenge lies in managing the effects of higher-order magnetic fields, which often arise from field errors in the multipoles used to guide and focus the particle beams. These field errors, including from quadrupolar up to decahexapolar components, can profoundly impact beam dynamics and stability. Addressing these challenges is essential to ensuring that the LHC operates effectively and continues to produce valuable scientific results. The following extended summary synthesizes findings from three detailed studies investigating various aspects of higher-order multipole effects and their implications for the LHC's performance.

This thesis employs the Hamiltonian formalism to describe particle motion in the transverse planes under the influence of various multipole fields. In non-linear lattices, the complexity of beam dynamics increases significantly, necessitating the use of advanced mathematical tools such as Lie Algebra and Poisson Brackets to accurately characterize non-linear effects. The study derives explicit higher-order non-linear transfer maps and provides a comprehensive summary of multipole combinations. These non-linearities in the lattice lead to intricate phenomena such as chromaticity, amplitude detuning, chromatic amplitude detuning, and resonances driven by Resonance Driving Terms (RDTs), all of which are thoroughly derived and supported by detailed measurement techniques.

Optics measurements are conducted using a range of software tools and techniques. Turn-by-turn data acquisition via Beam Position Monitors (BPMs) is emphasized as a crucial method for evaluating beam optics, where an AC-dipole excites the beam, and the resulting oscillations are analyzed using Fourier transforms to extract tunes and identify resonances. Further treatment is done via the oscillation amplitudes and the magnitude of spectral lines to retrieve linear and non-linear observables such as the phase advance, beta function, dispersion, coupling, orbit, and RDTs. Chromaticity measurements involve inducing momentum offsets by varying the RF frequency and observing the corresponding tune shifts. The thesis also introduces a custom tool, the Non-Linear Chromaticity GUI, which streamlines the analysis and correction of chromaticity by fitting measured data to higher-order chromaticity functions and implementing necessary adjustments. A key correction strategy discussed is the response matrix, a linear equation system that describes how variations in multipole strengths impact observables, which has proven effective in correcting both linear and non-linear observables in the LHC.

The first study explores the origins and consequences of skew octupolar fields within the LHC. These fields significantly influence the dynamic aperture of the accelerator, a critical parameter that defines the range within which the particle beam remains stable. Skew octupolar correctors are installed around key detectors, such as ATLAS and CMS, to manage these fields and mitigate their effects on beam stability. The study focuses on measuring these fields with optics designed for top energy, 6.8 TeV per particle. Corrections were performed using a response matrix method, a different approach than what was used a few years prior. This method effectively addresses skew octupolar RDTs using the available corrector magnets, although its performance is limited by the absence of one corrector, which constrains the achievable correction strength. Consequently, certain RDTs, like f_{1012} and f_{1210}, can either be effectively corrected or maintained at a constant level depending on the corrector configuration. The level of correction achieved is comparable to that obtained using a different method in the last LHC Run.

Additionally, the study investigates the unexpected influence of Landau octupoles on skew octupolar RDTs at injection energy, 450 GeV per particle. Landau octupoles are powerful octupoles used at injection energy to introduce damping through a tune spread. During measurements, a significant shift in skew octupolar RDTs was observed with various powerings of the Landau octupoles. Initially, these octupoles were expected to generate skew fields only with misalignments, specifically roll errors. However, simulations indicate that octupole misalignments have minimal impact on skew octupolar fields. Instead, coupling has been identified as a crucial factor. The combination of coupling and Landau octupoles is expected to be a major contributor to skew octupolar RDTs at injection energy, where octupoles are strongly powered. Accurate modeling of coupling is thus essential for predicting the behavior of skew octupolar RDTs and managing their impact on beam stability.

The second study focuses on decapolar fields in the LHC, particularly at injection energy. This study addresses previously observed discrepancies between measurements and models related to third-order chromaticity, a critical parameter that describes how particles with an energy deviation experience different oscillation frequencies than the reference particle. Accurate control of chromaticity is vital for maintaining beam stability. The introduction of previously unobserved observables, has provided a clearer understanding of these discrepancies. Among these observables are the bare chromaticity, which represents the chromaticity of the machine without any correctors powered on to observe the bare influence of field errors, and chromatic amplitude detuning, a detuning function of both momentum deviations and amplitude. Several approaches to measuring the same fields help clarify the various contributions. The research reveals that the decay of the decapolar component in the main dipoles is a significant factor contributing to these discrepancies. When the LHC was designed, this decay was deemed too small to be significant and thus was not included in the magnetic error tables used for simulation. However, as the machine's parameters are pushed further each year and the effects of higher-order fields become better understood, it becomes clear that accurate control and modeling of these fields are necessary.

For the first time, measurements and corrections of the decapolar Resonance Driving Term f_{1004} were carried out at injection energy. Implementing combined corrections for third-order chromaticity, chromatic amplitude detuning, and RDT f_{1004} led to a 3% improvement in beam lifetime. Conversely, deliberately degrading the RDT alone resulted in a 10% decrease in beam lifetime, underscoring the importance of this resonance corrections for stable beam operation. The study also explored how sextupoles and octupoles interact to generate decapolar-like fields. It was found that sextupoles, both alone and in combination with Landau octupoles, produce a substantial f_{1004} decapolar RDT when powered to small currents. Therefore, in an operational context, decapolar resonances, largely generated by strong octupoles, would benefit from adapted corrections. These findings suggest that further advancements in correction methods could lead to even greater improvements in beam stability.

The third study investigates higher-order fields in the LHC, specifically dodecapolar and decatetrapolar fields. Using a newly implemented collimation setup and custom post-processing techniques, this study successfully observed these higher-order fields. Studies were conducted to estimate the effect of the non-linearity of the momentum compaction factor on the chromaticity function during its computation from the RF frequency. The results indicate that while the momentum compaction factor shows a second order in the LHC, its effects on the resulting chromaticity are negligible even at large momentum offsets. Several chromaticity measurements with varying configurations of octupolar and decapolar corrections then revealed the presence of fourth and fifth-order terms ($Q^{(4)}$ and $Q^{(5)}$). These measurements consistently identified these higher-order terms with similar values, demonstrating their robustness. Additionally, it is emphasized that accurately characterizing the lower-order terms requires good measurement of these higher-order terms. The study identifies, through simulations, dodecapolar and decatetrapolar fields as primary contributors to these higher-order effects, originating from field errors in the main dipoles and quadrupoles. The LHC's field error model appears to be in relative agreement with the measurements once the decay of decatetrapolar components is considered.

For the first time at injection energy, the dodecapolar Resonance Driving Term f_{0060} was measured. This measurement shows clear repeatability, even when performed with different configurations of octupolar and decapolar corrections. The measured values were found to be in good agreement with the model. The research concludes that further investigations are needed to address limitations in the measurement range of the chromaticity function and to refine estimates of higher-order chromaticity terms. Additionally, studying the impact of lower-order multipoles on the dodecapolar RDT and its effect on beam lifetime would be valuable for optimizing the LHC's performance.

In summary, the research detailed in these studies underscores the critical importance of understanding and managing higher-order multipole effects in the LHC. Skew octupolar fields, decapolar fields, and other higher-order terms have a significant impact on beam stability and performance. Developing and implementing advanced diagnostic techniques and correction methods are essential for enhancing simulation accuracy and operational strategies. The insights gained from these studies are not only crucial for optimizing the LHC's performance but also for guiding the design and operation of future accelerator projects.

As particle accelerators continue to evolve, the challenges associated with higher-order multipole components will persist. Ongoing research in this field is vital for addressing these challenges and ensuring that future accelerators achieve the precision required for groundbreaking scientific discoveries. The lessons learned from the LHC's experience with the complex interactions of multipole fields will inform the design and operation of next-generation accelerators, ensuring they remain at the forefront of exploring fundamental questions about the universe.

The work presented in these chapters represents a significant contribution to the field of accelerator physics by offering practical solutions for current operational challenges and paving the way for future advancements.

Zusammenfassung

Der Large Hadron Collider (LHC) am CERN, der sich in einem 27 Kilometer langen Tunnel unter der Schweizer-französischen Grenze befindet, ist der weltweit größte und leistungsstärkste Teilchenbeschleuniger. Seine Hauptmission ist es, die Bedingungen des Universums kurz nach dem Urknall nachzubilden und den Wissenschaftlern zu ermöglichen, die fundamentalen Kräfte und Teilchen zu erforschen, die das Kosmos ausmachen. Diese bemerkenswerte Einrichtung beschleunigt Protonen und schwere Ionen auf nahezu Lichtgeschwindigkeit, bevor sie mit enormer Energie kollidieren, was tiefgreifende Einblicke in die Bausteine der Materie und die grundlegenden Wechselwirkungen bietet, die unser Universum regieren. Der LHC stellt nicht nur ein monumentales Ingenieurwerk dar, sondern auch ein entscheidendes Werkzeug zur Weiterentwicklung unseres Verständnisses der Hochenergiephysik.

Der Betrieb einer so komplexen und leistungsstarken Maschine erfordert die Überwindung zahlreicher technischer Herausforderungen, insbesondere bei der Aufrechterhaltung der präzisen Kontrolle und Stabilität der Teilchenstrahlen. Eine wesentliche Herausforderung besteht darin, die Auswirkungen höherer magnetischer Felder zu managen, die oft aus Feldfehlern in den Multipolen resultieren, die zur Lenkung und Fokussierung der Teilchenstrahlen verwendet werden. Diese Feldfehler, von quadrupolaren bis hin zu dekahexapolaren Komponenten, können die Strahldynamik und Stabilität erheblich beeinflussen. Die Bewältigung dieser Herausforderungen ist entscheidend, um sicherzustellen, dass der LHC effektiv arbeitet und weiterhin wertvolle wissenschaftliche Ergebnisse liefert. Die folgende ausführliche Zusammenfassung synthetisiert Ergebnisse aus drei detaillierten Studien, die verschiedene Aspekte der höherordentlichen Multipol-Effekte und deren Auswirkungen auf die Leistung des LHC untersuchen.

Diese Dissertation verwendet das Hamiltonsche Formalismus zur Beschreibung der Teilchenbewegung in den transversalen Ebenen unter dem Einfluss verschiedener Multipolfelder. In nichtlinearen Lattices steigt die Komplexität der Strahldynamik erheblich, was den Einsatz fortgeschrittener mathematischer Werkzeuge wie Lie-Algebren und Poisson-Klammern erforderlich macht, um nichtlineare Effekte genau zu charakterisieren. Die Studie leitet explizite höherordentliche nichtlineare Übertragungsabbildungen ab und bietet eine umfassende Zusammenfassung von Multipol-Kombinationen. Diese Nichtlinearitäten im Lattice führen zu komplexen Phänomenen wie Chromatizität, Amplitudenabstimmung, chromatischer Amplitudenabstimmung und Resonanzen, die durch Resonance Driving Terms (RDTs) verursacht werden, die gründlich abgeleitet und durch detaillierte Messtechniken unterstützt werden.

Optikmessungen werden mit einer Reihe von Software-Tools und Techniken durchgeführt. Die Datenerfassung Turn-by-Turn über Beam Position Monitors (BPMs) wird als entscheidende Methode zur Bewertung der Strahloptik hervorgehoben, wobei ein AC-Dipol den Strahl anregt und die resultierenden Oszillationen mittels Fourier-Transformationen analysiert werden, um Tunes zu extrahieren und Resonanzen zu identifizieren. Weitere Behandlungen erfolgen über die Oszillationsamplituden und die Größe der Spektrallinien, um lineare und nichtlineare Observable wie die Phasenadvance, die Beta-Funktion, Dispersion, Kopplung, Orbit und RDTs abzuleiten. Chromatizitätsmessungen beinhalten die Erzeugung von Impulsabweichungen durch Variation der RF-Frequenz und Beobachtung der entsprechenden Tune-Verschiebungen. Die Dissertation führt auch ein benutzerdefiniertes Werkzeug, das Non-Linear Chromaticity GUI, ein, das die Analyse und Korrektur der Chromatizität vereinfacht, indem gemessene Daten an höherordentliche Chromatizitätsfunktionen angepasst und notwendige Anpassungen vorgenommen werden. Eine wichtige Korrekturstrategie, die diskutiert wird, ist die Reaktionsmatrix, ein lineares Gleichungssystem, das beschreibt, wie Variationen in den Multipolstärken die Observablen beeinflussen, und sich als effektiv bei der Korrektur sowohl linearer als auch nichtlinearer Observablen im LHC erwiesen hat.

Die erste Studie untersucht die Ursprünge und Konsequenzen von schiefen Oktupolfeldern innerhalb des LHC. Diese Felder beeinflussen erheblich die dynamische Apertur des Beschleunigers, ein kritischer Parameter, der den Bereich definiert, innerhalb dessen der Teilchenstrahl stabil bleibt. Schiefe Oktupol-Korrektoren sind um wichtige Detektoren wie ATLAS und CMS installiert, um diese Felder zu managen und ihre Auswirkungen auf die Strahlinstabilität zu mindern. Die Studie konzentriert sich auf die Messung dieser Felder mit Optiken, die für die Höchstenergie von 6,8 TeV pro Teilchen ausgelegt sind. Korrekturen wurden unter Verwendung der Reaktionsmatrixmethode durchgeführt, einem anderen Ansatz als der, der vor einigen Jahren verwendet wurde. Diese Methode adressiert effektiv schiefe Oktupol-RDTs unter Verwendung der verfügbaren Korrektormagnete, obwohl ihre Leistung durch das Fehlen eines Korrektors begrenzt ist, was die erreichbare Korrekturstärke einschränkt. Folglich können bestimmte RDTs wie f_{1012} und f_{1210} je nach Korrektorkonfiguration entweder effektiv korrigiert oder auf konstantem Niveau gehalten werden. Das erreichte Korrekturniveau ist vergleichbar mit dem, das mit einer anderen Methode im letzten LHC-Betrieb erreicht wurde.

Zusätzlich untersucht die Studie den unerwarteten Einfluss von Landau-Oktupolen auf schiefe Oktupol-RDTs bei der Injektionsenergie von 450 GeV pro Teilchen. Landau-Oktupole sind leistungsstarke Oktupole, die bei der Injektionsenergie verwendet werden, um Dämpfung durch eine Tune-Streuung einzuführen. Während der Messungen wurde eine signifikante Verschiebung in den schiefen Oktupol-RDTs bei verschiedenen Stromstärken der Landau-Oktupole beobachtet. Zunächst wurde erwartet, dass diese Oktupole nur durch Fehlanpassungen, insbesondere Rollfehler, schiefe Felder erzeugen. Simulationen zeigen jedoch, dass Oktupol-Fehlanpassungen minimale Auswirkungen auf schiefe Oktupolfelder haben. Stattdessen wurde die Kopplung als entscheidender Faktor identifiziert. Die Kombination von Kopplung und Landau-Oktupolen wird als wesentlicher Beitrag zu schiefen Oktupol-RDTs bei der Injektionsenergie erwartet, wo Oktupole stark betrieben werden. Eine genaue Modellierung der Kopplung ist daher entscheidend für die Vorhersage des Verhaltens von schiefen Oktupol-RDTs und die Verwaltung ihrer Auswirkungen auf die Strahlinstabilität.

Die zweite Studie konzentriert sich auf dekapolare Felder im LHC, insbesondere bei der Injektionsenergie. Diese Studie behandelt zuvor beobachtete Diskrepanzen zwischen Messungen und Modellen im Zusammenhang mit der dritthöchsten Chromatizität, einem kritischen Parameter, der beschreibt, wie Teilchen mit einer Energieabweichung unterschiedliche Oszillationsfrequenzen als das Referenzteilchen erleben. Eine genaue Kontrolle der Chromatizität ist entscheidend für die Aufrechterhaltung der Strahlinstabilität. Die Einführung zuvor unbeobachteter Observablen hat ein klareres Verständnis dieser Diskrepanzen ermöglicht. Zu diesen Observablen gehören die rohe Chromatizität, die die Chromatizität der Maschine ohne eingeschaltete Korrektoren darstellt, um den reinen Einfluss der Feldfehler zu beobachten, und die chromatische Amplitudenabstimmung, eine Abstimmungsfunktion sowohl für Impulsabweichungen als auch für Amplituden. Mehrere Ansätze zur Messung derselben Felder helfen, die verschiedenen Beiträge zu klären. Die Forschung zeigt, dass der Zerfall der dekapolaren Komponente in den Hauptdipolen ein wesentlicher Faktor für diese Diskrepanzen ist. Als der LHC entworfen wurde, wurde dieser Zerfall als zu gering angesehen, um signifikant zu sein, und daher nicht in die für Simulationen verwendeten Magnetfehler-Tabellen aufgenommen. Da jedoch die Parameter der Maschine jedes Jahr weiter erhöht werden und die Auswirkungen höherordentlicher Felder besser verstanden werden, wird klar, dass eine genaue Kontrolle und Modellierung dieser Felder notwendig sind.

Erstmals wurden Messungen und Korrekturen des dekapolaren Resonance Driving Term f_{1004} bei der Injektionsenergie durchgeführt. Die Implementierung kombinierter Korrekturen für die dritthöchste Chromatizität, chromatische Amplitudenabstimmung und RDT f_{1004} führte zu einer Verbesserung der Strahllaufzeit um 3 %. Im Gegensatz dazu führte eine absichtliche Verschlechterung des RDTs allein zu einem Rückgang der Strahllaufzeit um 10 %, was die Bedeutung dieser Resonanzkorrekturen für einen stabilen Betrieb des Strahls unterstreicht. Die Studie untersuchte auch, wie Sextupole und Oktupole interagieren, um dekapolarähnliche Felder zu erzeugen. Es wurde festgestellt, dass Sextupole, sowohl allein als auch in Kombination mit Landau-Oktupolen, bei kleinen Strömen einen erheblichen f_{1004}-dekapolaren RDT erzeugen. Daher würden in einem betrieblichen Kontext dekapolare Resonanzen, die größtenteils durch starke Oktupole erzeugt werden, von angepassten Korrekturen profitieren. Diese Erkenntnisse legen nahe, dass weitere Fortschritte bei den Korrekturmethoden zu noch größeren Verbesserungen der Strahlinstabilität führen könnten.

Die dritte Studie untersucht höherordentliche Felder im LHC, insbesondere dodecapolare und decatetrapolare Felder. Durch den Einsatz eines neu implementierten Kollimationssystems und maßgeschneiderter Nachbearbeitungstechniken konnte diese Studie erfolgreich diese höherordentlichen Felder beobachten. Studien wurden durchgeführt, um den Effekt der Nichtlinearität des Impulskompaktionsfaktors auf die Chromatizitätsfunktion während ihrer Berechnung aus der RF-Frequenz zu schätzen. Die Ergebnisse zeigen, dass der Impulskompaktionsfaktor zwar zweiter Ordnung im LHC zeigt, seine Auswirkungen auf die resultierende Chromatizität jedoch selbst bei großen Impulsabweichungen vernachlässigbar sind. Mehrere Chromatizitätsmessungen mit unterschiedlichen Konfigurationen von Oktupol- und Dekapolarkorrekturen offenbarten dann die Präsenz von vierten und fünften Ordnungsterminen ($Q^{(4)}$ und $Q^{(5)}$). Diese Messungen identifizierten konsequent diese höherordentlichen Terme mit ähnlichen Werten und demonstrierten ihre Robustheit. Darüber hinaus wird betont, dass eine genaue Charakterisierung der niedrigerordentlichen Terme eine gute Messung dieser höherordentlichen Terme erfordert. Die Studie identifiziert durch Simulationen dodecapolare und decatetrapolare Felder als Hauptbeiträge zu diesen höherordentlichen Effekten, die von Feldfehlern in den Hauptdipolen und Quadrupolen ausgehen. Das Fehler-Modell des LHC scheint im Vergleich zu den Messungen in relativer Übereinstimmung zu stehen, sobald der Zerfall der decatetrapolaren Komponenten berücksichtigt wird.

Erstmals wurde bei der Injektionsenergie der dodecapolare Resonance Driving Term f_{0060} gemessen. Diese Messung zeigt eine klare Wiederholbarkeit, selbst bei unterschiedlichen Konfigurationen von Oktupol- und Dekapolarkorrekturen. Die gemessenen Werte erwiesen sich als gut mit dem Modell übereinstimmend. Die Forschung kommt zu dem Schluss, dass weitere Untersuchungen erforderlich sind, um Einschränkungen im Messbereich der Chromatizitätsfunktion zu adressieren und Schätzungen höherordentlicher Chromatizitäts-Terme zu verfeinern. Darüber hinaus wäre es wertvoll, den Einfluss niedrigerer Multipole auf den dodecapolaren RDT und dessen Auswirkungen auf die Strahllaufzeit zu untersuchen, um die Leistung des LHC zu optimieren.

Zusammenfassend betont die Forschung, die in diesen Studien detailliert beschrieben wird, die entscheidende Bedeutung des Verständnisses und Managements höherordentlicher Multipol-Effekte im LHC. Schiefe Oktupolfelder, dekapolare Felder und andere höherordentliche Terme haben einen signifikanten Einfluss auf die Strahlinstabilität und -leistung. Die Entwicklung und Implementierung fortschrittlicher Diagnoseverfahren und Korrekturmethoden sind entscheidend für die Verbesserung der Simulationsgenauigkeit und operativen Strategien. Die Erkenntnisse aus diesen Studien sind nicht nur entscheidend für die Optimierung der LHC-Leistung, sondern auch für die Gestaltung und den Betrieb zukünftiger Beschleunigerprojekte.

Da sich Teilchenbeschleuniger weiterentwickeln, werden die Herausforderungen im Zusammenhang mit höherordentlichen Multipolkomponenten bestehen bleiben. Laufende Forschung auf diesem Gebiet ist unerlässlich, um diese Herausforderungen zu bewältigen und sicherzustellen, dass zukünftige Beschleuniger die Präzision erreichen, die für bahnbrechende wissenschaftliche Entdeckungen erforderlich ist. Die aus den Erfahrungen des LHC mit den komplexen Wechselwirkungen der Multipol-Felder gewonnenen Lektionen werden die Gestaltung und den Betrieb von Beschleunigern der nächsten Generation informieren und sicherstellen, dass sie an der Spitze der Erforschung fundamentaler Fragen zum Universum bleiben.

Die in diesen Kapiteln präsentierte Arbeit stellt einen bedeutenden Beitrag zum Bereich der Beschleunigerphysik dar, indem sie praktische Lösungen für aktuelle betriebliche Herausforderungen bietet und den Weg für zukünftige Fortschritte ebnet.

Acknowledgements

Ok, so this is the place where I get to talk about my life and where you'll be looking for you name to see what I've got to say about you. This would need to be a blog post given how many things I want to say, so it will be *relatively* brief. Let's start first by saying that I'm incredibly happy to have to done this thesis at CERN, which I honestly found quite fun. Not only because the subject was interesting, but also because I have been surrounded by kind, caring and smart people through all these years.

To give a little perspective, I have originally studied computer science at EPITA (École Pour l'Informatique et les Techniques Avancées) in Paris and earned an engineering degree in that field. Nothing really predestined me to work in any field related to physics, let alone to do a PhD on accelerator physics, but here we are! After my degree, I applied for a trainee position at CERN, basically working on software development for optics measurements and corrections. After two years of training, I was proposed with a PhD on the topics I've been learning, which I gladly accepted. This is how I embarked on a 3-year journey about accelerator physics. For this, I would never be thankful enough to Rogelio Tomas, who recruited and trusted me for that first contract, without which my life would probably be vastly different. I am also immensely grateful to Ewen Maclean, who has been a fantastic supervisor, even probably the best I've had yet to meet. He has always been present to help with me accelerator concepts in a very intelligible manner. Being kind, following up with my studies and always proposing new ideas made me feel like a complete member of the OMC team. On the university side, at Goethe-Universität Frankfurt, I would like to thank Giuliano Franchetti for his guidance and ideas about this thesis.

Through my now five years at CERN, I have had the privilege to meet incredible people who changed not only my career path but also who I am for the best. And even if it sounds a bit weird, I am incredibly happy you have all been there.

Upon starting my very first contract, I was paired with Max Mihailescu and Sébastien Joly in an office, all three beginning our journey at CERN. I am very thankful to Max for having been a good friend during his short stay here, and for his insights on mathematics. I consider myself remarkably lucky to have met Sébastien, who probably should be listed as a supervisor here given how much he helped me when I struggled to learn the basics of accelerator physics. I would also like to thank

Michael Hofer and Félix Carlier, who were there to answer my countless questions, be it when I started or even now at the end of my PhD. Closely related to my thesis subject were Félix Soubelet and Joschua Dilly who greatly helped me in various ways. Thanks a lot as well to Jacqueline Keintzel and Frank Zimmerman, to have given me the opportunity to work for a month at KEK in Japan, and expand my knowledge of lepton accelerators.

Many thanks to all the members of the OMC team who were great colleagues, be it in the office or during barely-legal night and week-end shifts in the control room. Specifically, I would like to thank Wietse Van Goethem, Leon Van Riesen-Haupt, Elena Fol, Andreas Wegscheider, Vittorio Ferrentino and Tobias Persson. Talking about the control room, I want to thank the LHC operation team and specifically Michi Hostettler for our conversations and his deep knowledge of CERN and the LHC.

CERN being a vast laboratory, I had the pleasure to meet remarkable people who I enjoyed to be around. I cannot detail how much you all mean to me as this is already quite long, but you get the idea. For this, thanks a lot to Sofia, Christophe, David, Jean-Baptiste, Lisa, Joanna, Roxana, Dora, Joséphine, Jack, Ellie, Tirsi, Kostas, Björn, Christian, Laura, Roland, Luca, Wainer, Tiziana and Pierre.

This thesis would not have been possible without the support of people from outside of CERN. Namely I would like to thank my IRC friends, bonswouar, WhatIsGoingDown, pankkake, ShameOnYou, href and bishop. Special thanks to a large friend group I have always loved to be part of, *la crème de la crème de la cataphilie.* Thanks a ton as well to Clotilde, Matthias, Alpha, Paul, Antoine, Nicolas, Youness, Ksenia, Gérard, Vivien, Baptiste, Félix, Benjamin, Fabian and Tsu for everything that happened during those years, making them memorable. I would like to thank a lot my parents and family who have always been there to support me in every possible way, no matter my decisions. Thanks Antje, Michel, and Yoann.

Il faut savoir douter où il faut,
se soumettre où il faut,
croire où il faut.

Blaise Pascal

Contents

Glossary

Nomenclature

AC-Dipole Dipole magnet capable of generating variable oscillating fields. Used to increase the transverse amplitude via forced oscillations for optics measurements.

Amplitude detuning Tune shift dependent on the amplitude of transverse oscillations. Corrected via octupoles.

Aperture Physical aperture, i.e. where the beam can pass, of an element in the accelerator.

Beam Short for "Particle beam". Beam 1 and Beam 2 refer to either of the two beams travelling in opposite directions in the LHC.

Beta-beating Relative difference of the beta function between measurement and model. Often expressed in percents: $(\beta_{meas.} - \beta_{mdl})/\beta_{mdl.} \cdot 100$.

Beta-function Twiss parameter β as a function of s, the longitudinal position. Related to the amplitude of transverse oscillations of the beam and its size.

Chromatic Amplitude Detuning Tune shift dependent on both the amplitude of transverse oscillations and the momentum offset. Corrected via decapoles.

Chromaticity Tune shift dependent on the momentum offset. Corrected via sextupoles to the first order.

Closed orbit Path of the reference particle through the accelerator.

Coupling Coupling of a particle's motion in the transverse planes. Corrected via skew quadrupoles.

Crosstalk Unwanted magnetic interference between adjacent multipoles.

Drift Drift space, a field-free region.

Dynamic Aperture Maximum region in phase space where particle motion remains stable over time, beyond which particles may be lost.

Feed-down Lower-order-like effects induced by a particle passing off-center through a multipole.

Feed-up Higher-order-like effects induced by a combination of multipoles.

Laundau Octupole Strong octupoles present in the LHC to introduce Landau Damping. The tune spread created via amplitude detuning helps damping the particles oscillations.

MAD-X Current version of the Methodical Accelerator Design framework developed in BE-ABP. Used for beam dynamics simulations.

Acronyms

ABP Accelerators and Beam Physics group – Responsible for studies and optimizations of beam dynamics over the complete CERN accelerator complex. Part of BE.

BBQ Base Band Tune – Precise tune measurement system consisting of a pick-up and filters.

BCH Baker-Campbell-Hausdorff theorem – Formula for the combination of exponentials in a Lie algebra, $e^X \cdot e^Y = e^Z$.

BE Beams department – Responsible for all aspects related to the production and delivery of particles, including beam physics, mechatronics, metrology, software development and operational management.

BPM Beam Position Monitor – Intrumentation used to retrieve both position and intensity of the beam via its induced electric field.

IP Interaction Point – Center of the straight arcs of the LHC. Beams collides in four of them where they cross (IP1, 2, 5, 8).

IR Interaction Region – Vicinity of the interaction point. Often used interchangeably with ”IP”.

LHC Large Hadron Collider – Largest and most powerful particle collider in the world.

LNO Linear and Non-Linear Optics section – In charge of optics studies for current and future accelerators at CERN. Part of BE-ABP.

LSA LHC Software Architecture – Software used to operate the particle accelerators at CERN. Based on an online database to manage high and low level parameter settings.

MAD-X Methodical Accelerator Design – Current version of the framework developed in BE-ABP. Used for beam dynamics simulations.

MD Machine Development – Dedicated studies aimed at improving the accelerator parameters or testing new operational configurations.

OMC Optics Measurements and Corrections – Name of the team dedicated to optics studies on the main CERN accelerators. Part of BE-ABP-LNO.

PTC Polymorphic Tracking Code – Framework used by MAD-X to perform calculations in the non-linear regime.

RDT Resonance Driving Term – Coefficients related to the strength of a resonance.

RF Radio Frequency – Shorthand for the acceleration system of the accelerator.

Symbols

$B\rho$ Magnetic rigidity – Quantifies the ability of a field to deviate a particle [Tm].

J_n Skew magnetic field strength – Skew field component of a multipole of order n, normalized to the magnetic rigidity [$\mathrm{m}^{-\mathrm{n}}$].

$J_{x,y}$ Action – Phase space coordinate in the Courant-Snyder normalization [m].

K_n Normal magnetic field strength – Normal field component of a multipole of order n, normalized to the magnetic rigidity [$\mathrm{m}^{-\mathrm{n}}$].

Q Tune – Number of betatron oscillations per turn in a circular accelerator [1].

$Q^{(n)}$ Chromaticity of order n – Orders up to three are generally denoted Q', Q'' and Q''' [1].

[,] Poisson brackets operator – Commonly used in accelerator physics as commutator in the Lie algebra.

α_c Momentum compaction factor – Characterizes the change of particles' path length with the momentum offset [1].

β^* β-function at a given IP [m].

δ Momentum offset – Deviation of a particle's momentum relative to the reference one [1].

f_{jklm} Resonance Driving Term – Specific term related to a multipole of order $n = j+k+l+m$ [$\mathrm{m}^{-n/2}$].

$|C^-|$ Minimum tune separation – Global quantification of the linear coupling [1].

1 Introduction

1.1. Motivations

The motivation for this PhD research arises from the necessity to address higher-order non-linearities in the Large Hadron Collider (LHC). Nonlinear corrections are essential for the stable operation of circular colliders like the LHC, as they play a critical role in suppressing resonances, improving dynamic aperture, and enhancing beam lifetime. As the LHC continues to push the boundaries of its operational parameters, the influence of higher-order magnetic field errors, particularly those beyond octupoles, becomes increasingly significant, leading to potential degradation in performance.

One specific challenge highlighted during the LHC's Run 2 is the observed discrepancy at injection energy between the measured third-order chromaticity Q''' and the predictions made by existing models. The magnetic measurements of the LHC's magnets, conducted during its construction phase, have served as the foundation for simulations, beam steering, and nonlinear correction computations. However, this discrepancy suggests the presence of previously unaccounted-for field errors that are not captured by the initial magnetic measurements. Identifying and addressing these unknown sources of higher-order magnetic errors is crucial for improving the LHC's operational parameters, particularly during beam injection, to ensure optimal performance and stability.

To tackle these challenges, this research is driven by the need to develop and refine methods for measuring and characterizing higher-order non-linearities and understanding their impacts on beam dynamics. A key motivation is also to explore and improve techniques for measuring and characterizing higher-order magnetic fields, such as dodecapolar fields. These efforts are crucial for accurately modeling the complex interactions within the LHC and for implementing effective correction strategies that enhance the collider's performance. By advancing the understanding of these higher-order effects, this research aims to contribute to the continued success of the LHC and inform the design of future accelerators.

1.2. Thesis Outline

The thesis starts by giving an introduction to the field of accelerator physics in Chapter 1. The CERN accelerator complex and the LHC are then detailed. Key concepts of accelerator physics are presented in Chapter 2. Measurement and correction techniques are presented in Chapter 3.

The first results chapter, Chapter 4 examines the skew octupolar fields which have been shown to limit the dynamic aperture, especially during beam excitation with the AC-Dipole. A response matrix method was developed to correct skew octupolar Resonance Driving Terms (RDTs) at top energy. The study also explores the influence of Landau octupoles on skew octupolar RDTs at injection energy, revealing the importance of accurate coupling modeling in predicting these effects.

The second chapter, Chapter 5, delves into the decapolar fields at injection energy, addressing discrepancies between measurements and model predictions of third-order chromaticity. Through a series of novel measurements and simulations, including the introduction of chromatic amplitude detuning, the research identifies the decay of the decapolar component in the main dipoles as a key factor in these discrepancies. Corrective strategies were developed for decapolar RDTs, leading to measurable improvements in beam lifetime and stability.

The final chapter, Chapter 6, focuses on the measurement and analysis of dodecapolar and decatetrapolar fields, using an tailored post-processing technique. The study successfully measures higher-order chromaticity terms and dodecapolar RDTs, demonstrating their significant contribution to the overall field errors in the LHC. The findings underscore the need for further investigation into these higher-order fields and their impact on beam dynamics to optimize the LHC's performance.

Finally, conclusions for these studies are drawn in Chapter 7.

2

Concepts of Accelerator Physics

2.1. Particle Accelerators

Particle accelerators are a relatively recent development, driven by the particle physics field [1]. The first accelerators, at the beginning of the 20th century, were able to accelerate particles up to energies of a few MeV using electric fields.

The Cockcroft Walton generator was powerful enough to split an atom for the first time in 1932 [2], less than 100 years ago. Its design used capacitors and diodes to double the voltage at each stage, with its main limitation being the breakdown voltage of the capacitors. The Van de Graaff generator, created around the same time, was able to accelerate particles up to tens of MeV. They are still in use today [3] due to their capability of producing a wide variety of ion beams with energies ranging from hundreds of KeV to hundreds of MeV in the *Tandem* form [4].

Radiofrequency generators with alternating electric fields and drift tubes, first created by Rolf Wideröe in the late 1920s, mark the beginning of modern accelerator technology [5]. Rapidly evolving, particle accelerators progressed from accelerating particles to a few keV in linear accelerators to now TeV in circular accelerators, called synchrotrons.

While single-beam synchrotrons can be used for fixed-target experiments, only a fraction of the energy is available on impact. Dual-beam machines were more suitable for high energy physics experiments. The first hadron collider, the ISR, was built at CERN in 1971 with an energy of 62 GeV, taking its beam from the Proton Synchrotron (PS) [6].

Particle accelerators are still rapidly evolving. Several have been built in the past, and several are now either under construction or in the design study phase. New acceleration and focusing techniques are being developed, making the machines smaller. It is an exciting time for all fields that might benefit from energetic particles, whether in fundamental research, medical, industrial or security applications.

2.1.1. The CERN Complex

CERN is a large laboratory located on the border of France and Switzerland, near Geneva. Although well-known for discoveries in particle physics, studies are also conducted on medical applications, biology, radiation hardness or material science. Several accelerators are part of the accelerator complex, as illustrated in Fig. 2.1. A large number of fixed target experiments exist, whose beams are delivered by various accelerators depending on their needs. These experiments are often renewed [1].

The largest part of the CERN accelerator complex is the LHC. The LINAC4, PSB, PS and SPS accelerators serve as pre-injectors to the LHC, taking priority over their other experiments.

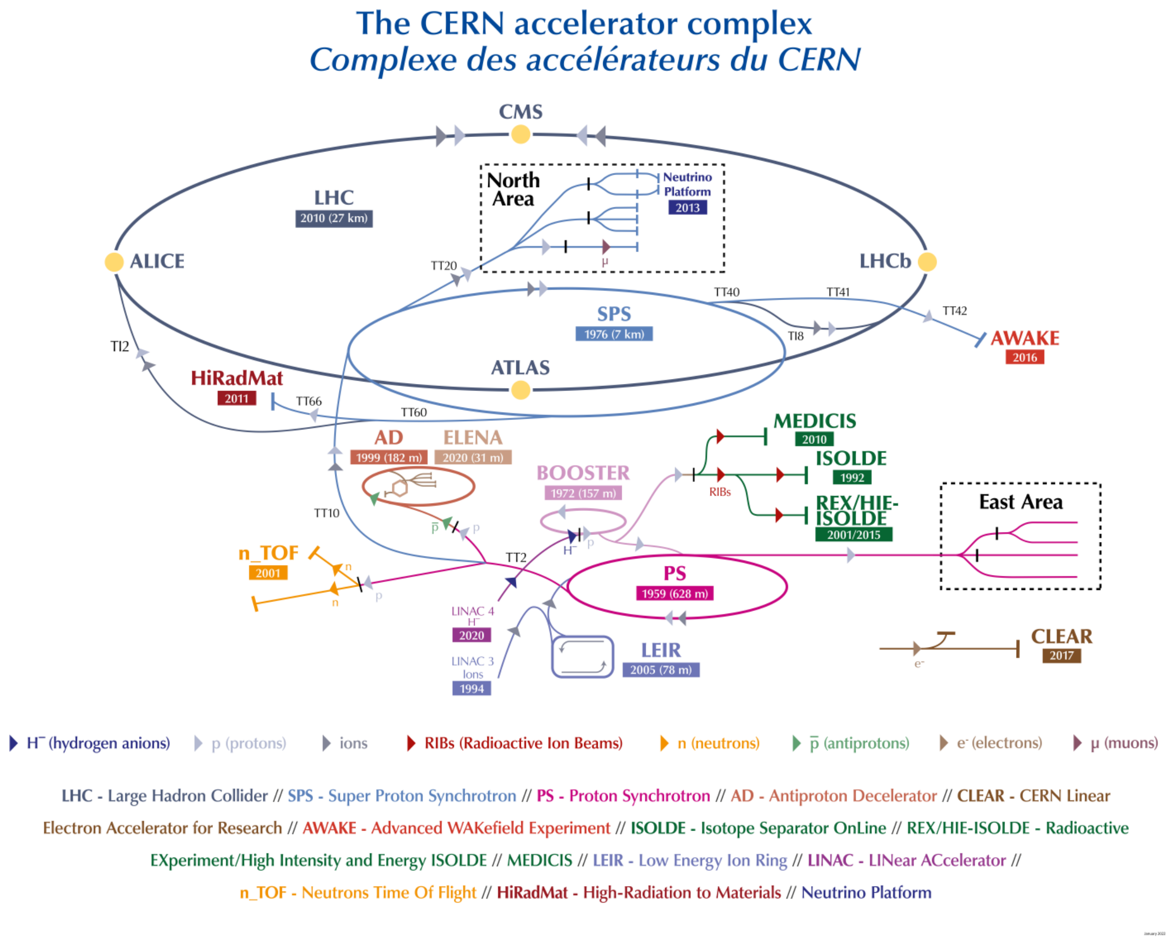

Figure 2.1.: Schematic illustration of the accelerator complex at CERN. Most accelerators are both used as injectors for the LHC or to provide beams to fixed target experiments [7].

[1] Up to date information can be found on https://home.cern/science/experiments.

2.1.2. The Large Hadron Collider

The Large Hadron Collider (LHC) is a circular particle accelerator primarily designed to collide protons for fundamental particle physics research. It can also occasionally collide ions such as oxygen or lead for specific studies. At the time of writing, in 2024, it holds several records, such as being the largest and most powerful accelerator in the world, at nearly 27 km long. The LHC is composed of two beam pipes, capable of accelerate two particle beams from an injection energy of 450 GeV to an energy of $6,800$GeV, before colliding them in four detectors: ATLAS, CMS, Alice and LCHb.

Well-publicized, the LHC is often depicted via its superconducting dipole magnets, housed in blue cryostats, aimed at cooling the coils. Figure 2.2 shows a 3D cut of such magnets. The LHC is mostly composed of these *main* dipoles, holding $1,232$ of them, each about 14 meters long. Superconducting materials like niobium-titanium (NbTi) are utilized, as conventional materials such as copper would melt under the current strain. Around $12,000$ amperes are supplied to generate the magnetic fields necessary for bending the trajectory of the particles. These particles travel at nearly the speed of light (99.99999905% of it), effectively going around the tunnel about $11,200$ times per second.

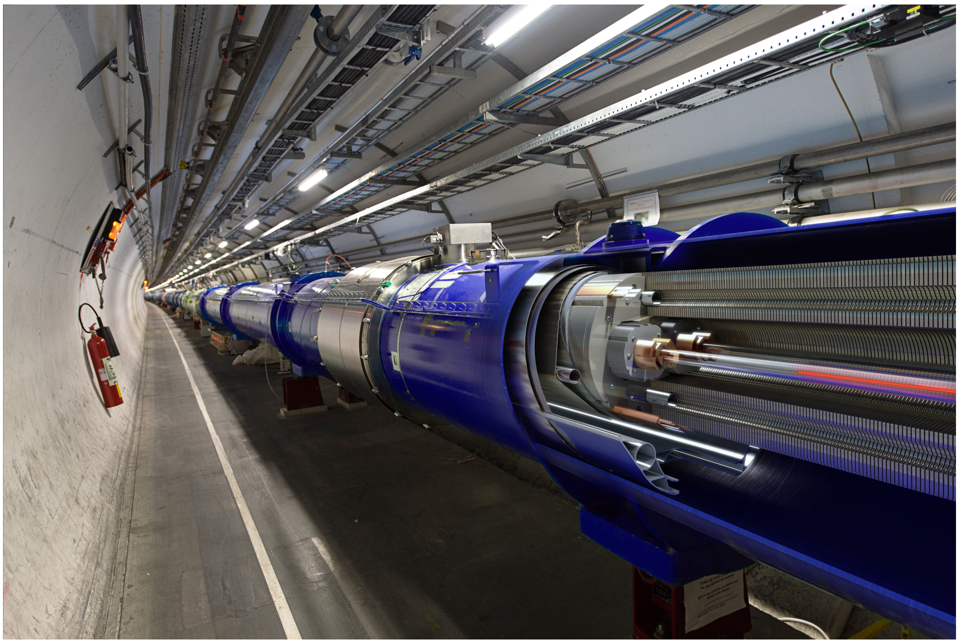

Figure 2.2.: 3D cut of a main LHC dipole [8]. Both beam pipes can be seen surrounded by the coils, strongly clamped by the yokes.

2

Straight Sections and Arcs

The LHC is not a perfect circle. It is indeed composed of four *straight* sections, called the *Interaction Regions* (IPs) where detectors or specific instrumentation are placed. Connecting those sections, the *arcs* are where the majority of the magnets and their correctors are located, along with some instrumentation like beam position monitors. Figure 2.3 shows the arcs as well as the purpose of each straight section, housing either specific instrumentation or detectors.

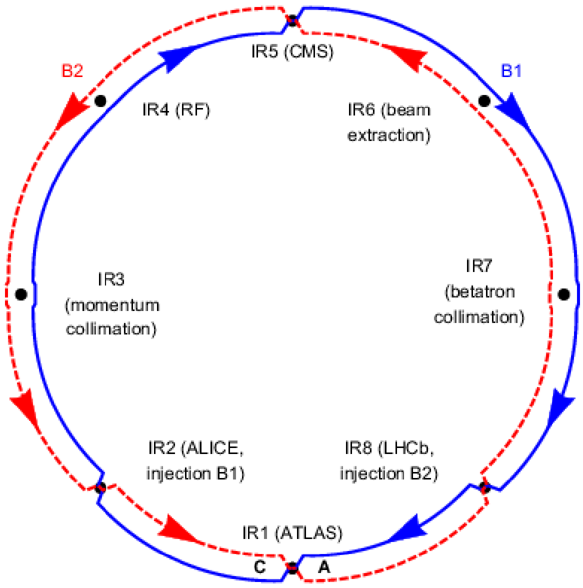

Figure 2.3.: Schematic of the LHC layout.

Arc Cells

Each arc is made up of 23 cells. Magnets are organized in a standard FODO structure (see Section 2.3.1), as shown in Fig. 2.4. *Dipoles* are responsible for bending the trajectory of the particles. Their associated correctors, the orbit correctors, mitigate any possible drift in the path. *Quadrupoles* are used to control the beam size along the ring. Their effect is focusing in one plane and defocusing in the other. Their associated correctors control the oscillations of the beam (see tune, Section 2.3.1) and possible field imperfections. *Sextupoles* correct chromaticity, a misfocus from quadrupoles due to particles having a different momentum than the reference particle. *Octupoles* are used to stabilize the beam by introducing Landau Damping [9]. The associated correctors correct higher-order chromaticity effects as well as amplitude-dependant tune shifts. *Decapoles* correctors aim at correcting an even higher chromaticity order.

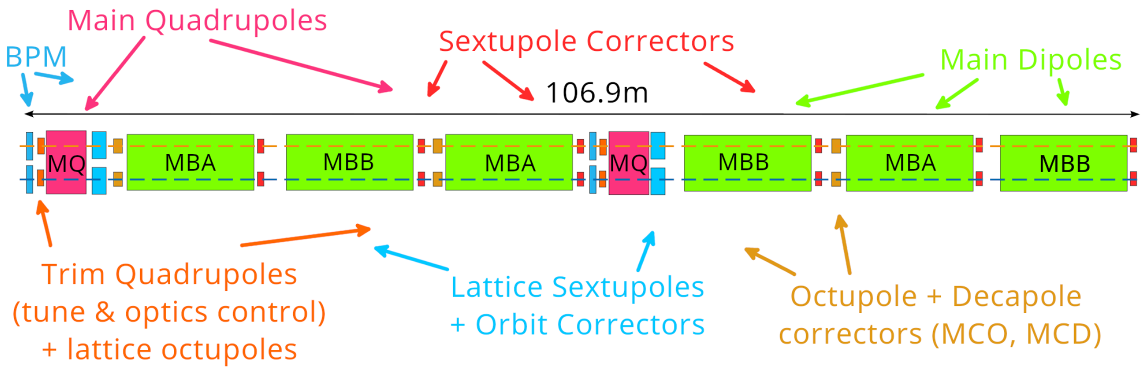

Figure 2.4.: Schematic of an LHC Arc cell [10].

Cycles

During the operation of the LHC, the machine goes through several states, each defined for specific scenarios [11].

A common example is the operational cycle of the LHC, illustrated in Fig. 2.5. Initially, the magnets are pre-cycled [12] without any beam circulating, to get them back to a reproducible state. Their current is then increased to accept particles at the injection energy of 450GeV. To verify the machine's proper functioning, a probe bunch of reduced intensity is first injected The number of bunches and their intensity are then gradually increased to attain the desired scheme needed for collisions, which varies throughout the year based on experimental demands. The number of bunches and their intensity can be adjusted as needed to ensure the machine's safety. A common scheme in 2024 is to inject about 2350 bunches with around 10^{11} particles each for collisions. Optics measurements, due to their destructive nature, typically use between one and three *pilot* bunches at a lower intensity of 10^{10} particles.

The magnets' current is then ramped along with the voltage in the RF system, to accelerate particles to an energy of 6.8 TeV. During this process, the beam is first squeezed at the Interaction Points. After completing the ramp-up, a second pass is performed to achieve a $\beta* = 30$cm at the ATLAS and CMS experiments, resulting in a smaller beam size. Crossing-angles are then introduced to make the beams collide.

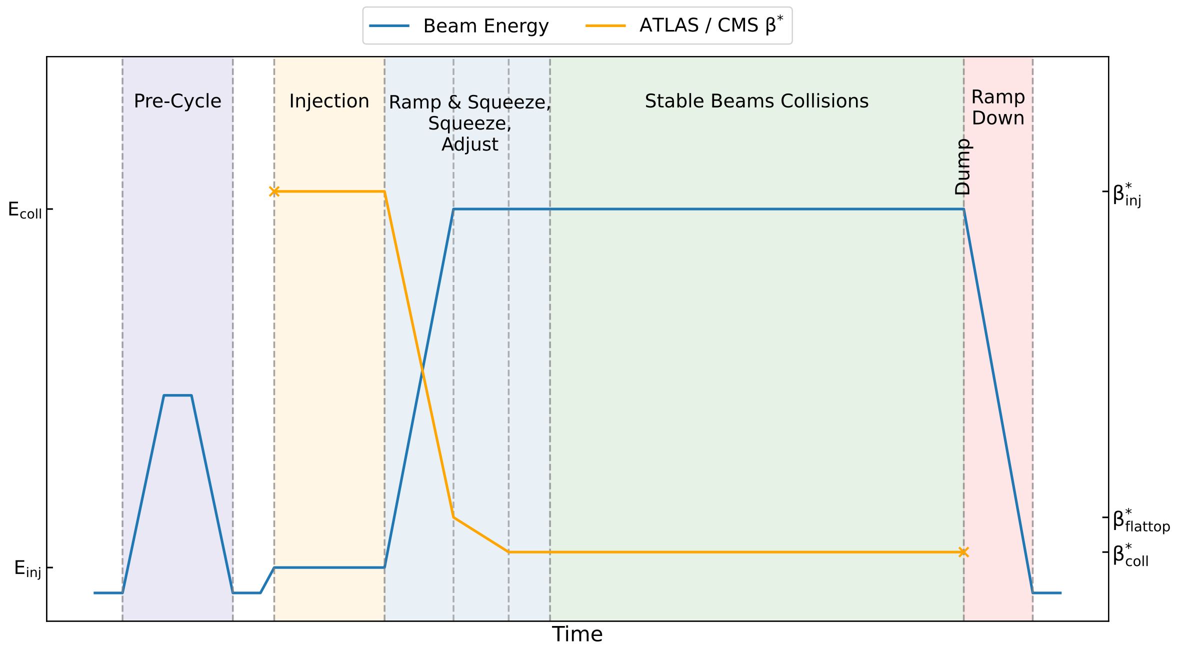

Figure 2.5.: Simplified illustration of a standard LHC cycle. Courtesy of Félix Soubelet [13].

2.2. Magnetic Fields

2.2.1. Nomenclature

Several notations coexist to denote magnetic fields. In this thesis, the *European Convention* [14] is used for field indices, as shown in Table 2.1. MAD-X, and MAD-NG, however, use the *American Convention*.

Multipole	Index	MAD-X
Dipole	1	0
Quadrupole	2	1
Sextupole	3	2
Octupole	4	3
Decapole	5	4
Dodecapole	6	5
Decatetrapole	7	6
Decahexapole	8	7

Table 2.1.: Relation between the field indices used in this thesis and multipoles.

As such, unless explicitly stated, quantities such as the magnetic strength b and normalized strength K presented latter will be expressed with this notation. A schematic representation of magnets up to dodecapole, order 6, is given in Fig. 2.6.

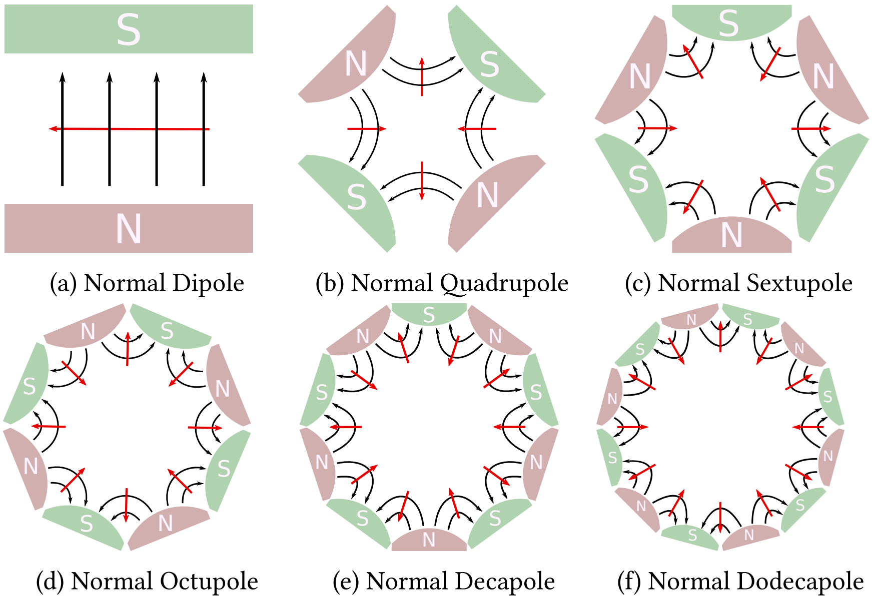

Figure 2.6.: Schematics of magnetic multipoles. In black the magnetic field lines, which extend also to the inner part of the magnets, but drawing them there has been omitted for clarity of the figure. Red arrows indicate the direction of force on a positive charge moving out of the page towards the reader. Courtesy of Joschua Dilly [14].

2.2.2. Multipole Expansion

In order to force the particles to form a closed orbit, they are subjected to magnetic fields that deflect their trajectories. The force exerted on a charged particle via electromagnetic fields is the Lorentz force $\vec{F}$ [15],

$$\vec{F} = \frac{\mathrm{d}\vec{p}}{\mathrm{d}t} = q\left(\vec{E} + \vec{v} \times \vec{B}\right), \tag{2.1}$$

where $\vec{p}$ is the momentum of the particle, q its charge, $\vec{v}$ its charge, $\vec{E}$ the electric field and $\vec{B}$ the magnetic field. With particles close to the speed of light, it becomes apparent that magnetic fields are dominant in the resulting force and are thus used to act on the particles trajectories. The guiding magnetic field in the transverse planes x and y can be described using a *multipole expansion*, where the components of the magnetic field can be written as a series of terms corresponding to different orders of multipoles. The multipole expansion is then given in terms of the normal and skew field gradients $\mathcal{B}$ and $\mathcal{A}$ with multipoles of order n [16],

$$B_y + iB_x = \sum_{n=1}^{\infty} (\mathcal{B}_n + i\mathcal{A}_n)\,(x + iy)^{n-1}. \tag{2.2}$$

The normal and skew field gradients $\mathcal{B}$ and $\mathcal{A}$ for a multipole of order n can then be calculated from this complex field,

$$\mathcal{B}_n + i\mathcal{A}_n = \frac{1}{(n-1)!} \cdot \left.\frac{\partial^{n-1}\left(B_y + iB_x\right)}{\partial(x+iy)^{n-1}}\right|_{x=0,\,y=0}. \tag{2.3}$$

For instance, expanded up to octupoles, the magnetic field acting on the horizontal plane reads,

$$B_y = \underbrace{B_{y0}}_{\text{dipole}} + \underbrace{\frac{\partial B_y}{\partial x} \cdot x}_{\text{quadrupole}} + \underbrace{\frac{1}{2!}\frac{\partial^2 B_y}{\partial x^2} \cdot x^2}_{\text{sextupole}} + \underbrace{\frac{1}{3!}\frac{\partial^3 B_y}{\partial x^3} \cdot x^3}_{\text{octupole}} + \cdots \tag{2.4}$$

An ideal magnet would often produce either a sole normal or skew field. However, this is not applicable to real-life magnets that are imperfect, due to design and manufacturing constraints. Field errors are thus introduced, relative to the main field of the ideal 2N-pole magnet at a reference radius r_{ref}, as shown in Eq. (2.5). The coefficients of the normal and skew relative field errors, referred to as a_n and b_n, are dimensionless but often given in *units* of 10^{-4}.

$$B_y + iB_x = \begin{cases} \mathcal{B}_N \cdot \sum_{n+1}^{\infty}(b_n + ia_n)\left(\frac{x+iy}{r_{ref}}\right)^{n-1}, \text{ for normal magnets} \\ \mathcal{A}_N \cdot \sum_{n+1}^{\infty}(b_n + ia_n)\left(\frac{x+iy}{r_{ref}}\right)^{n-1}, \text{ for skew magnets} \end{cases} \tag{2.5}$$

The total normal and skew field components of order n for an imperfect 2N-pole magnet is thus given by the following equation:

$$\begin{aligned} \mathcal{B}_n &= \mathcal{B}_N \cdot \frac{b_n}{r_{ref}^{n-1}}, \\ \mathcal{A}_n &= \mathcal{A}_N \cdot \frac{a_n}{r_{ref}^{n-1}}. \end{aligned} \tag{2.6}$$

The unit of the field is relative to the multipole order n: $[\mathrm{Tm}^{1-n}]$.

2.2.3. Beam Rigidity and Normalization

Beam Rigidity

In order to bend particles to form a ring, the force acting on the particles given by the Lorentz force must be equal to the centrifugal force [15, 17]:

$$q(\vec{E} + \vec{v} \times \vec{B}) = \frac{mv^2}{\rho}, \tag{2.7}$$

with q the charge of the particle, $\vec{E}$ and $\vec{B}$ respectively the electric and magnetic field strengths, $\vec{v}$ the velocity of the particle, m its mass and ρ the radius of the circular path. The beam rigidity is a quantification of the ability of a magnetic field to bend the trajectory of a particle. It is derived from the previous equation and relates the magnetic field B, the radius of curvature ρ to the momentum p and charge q of the particle. By neglecting the electrical force and using $p = mv$,

$$\begin{aligned} & qvB & & = \frac{mv^2}{\rho}, \\ \rightarrow\quad & qB & & = \frac{p}{\rho}, \\ \rightarrow\quad & B\rho & [\mathrm{T.m}] & = \frac{p}{q}. \end{aligned} \tag{2.8}$$

It is of interest when designing an accelerator to set the maximum field as well as the required radius of curvature for a specific momentum and particle. An interesting metric of an accelerator is also its *filling factor*, or percentage of dipoles in the machine. It can be calculated via the radius of curvature: $f = \rho/r$. A low filling factors means more space for other magnets, collimators, beam instrumentation, etc.

Field Normalization

The Beam Rigidity is also used as a way to normalize magnetic field strengths in particle accelerators where the momentum of the particle changes (i.e. acceleration or deceleration). The normalized Normal and Skew magnetic strengths K and J for a multipole of order n are thus given by [16] the following,

$$\begin{aligned} K_n &= \frac{q}{p}(n-1)!\mathcal{B}_n, \\ J_n &= \frac{q}{p}(n-1)!\mathcal{A}_n, \end{aligned} \tag{2.9}$$

with p the momentum of the particle, q its charge and $\mathcal{B}$ and *mathcalA* the field gradients.

2.2.4. Hamiltonian

2

The Hamiltonian describing the motion of relativistic particles in static electromagnetic fields is given by [18],

$$H = c\sqrt{(\mathbf{p} - q\mathbf{A})^2 + m^2c^2} + q\phi. \tag{2.10}$$

where ϕ is the scalar potential, $\mathbf{A}$ the vector potential, q, $\mathbf{p}$ and m respectively the charge, canonical momentum and mass of the particle and c the celerity of light.

After having changed this Hamiltonian to be dependent on curved coordinates, the motion in the transverse planes for a given multipole of order n (other than dipoles) can be described by the following [18],

$$\begin{aligned} H &= \frac{q}{p}\Re\left[\sum_{n>1}(\mathcal{B}_n + i\mathcal{A}_n)\frac{(x+iy)^n}{n}\right] \\ &= \Re\left[\sum_{n>1}(K_n + iJ_n)\frac{(x+iy)^n}{n!}\right]. \end{aligned} \tag{2.11}$$

Quite often, when studying the effect of a magnet on the beam, only one component is required, and the sum can thus be dropped. The normal and skew fields can also be isolated in order to consider their the sole effect as shown in the following,

$$\begin{aligned} N_n &= \frac{1}{n!}K_n\Re\left[(x+iy)^n\right], \\ S_n &= -\frac{1}{n!}J_n\Im\left[(x+iy)^n\right]. \end{aligned} \tag{2.12}$$

2.2.5. Harmonics

The magnetic fields in the LHC are generated by the coils of its magnets. However, real-world magnets never produce a perfect, single field as desired. Instead, some field errors, known as *allowed harmonics*, naturally arise due to the geometric symmetries of the coils. As a result, the main dipoles of the LHC can generate fields resembling those of sextupoles, decapoles, decatetrapoles, and so on [19]. Additionally, manufacturing imperfections contribute to field errors beyond the allowed ones, an example being octupolar errors seen in the LHC dipoles.

During the design of the LHC, the main dipoles have been identified to generate significant field errors. Magnetic measurements of those various fields were thus taken and magnetic tables built based on real-life magnets nowadays installed in the machine. Those magnetic tables, computed for each LHC configuration by *WISE* [20] are used by simulation softwares. Predictions of field errors and compensating strength for the correctors is computed by the Field Description for the LHC (*FiDeL*, [21]). FiDeL is used in the LHC control system in operation to compensate the field errors depending on the current configuration of the machine.

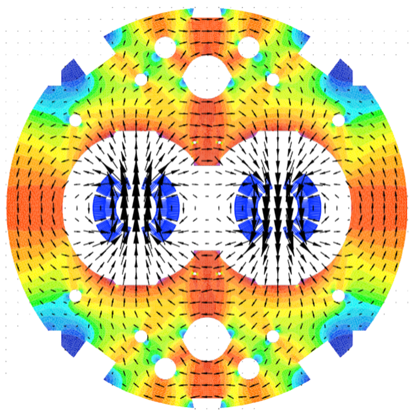

Figure 2.7.: Magnetic field in a dipole magnet [19].

2.3. Coordinate Systems

In circular accelerators, particle dynamics are represented using a traveling coordinate system. A reference orbit is determined by the lattice and its magnet strengths, forming the *optics*. In the case of a synchrotron, like the LHC, the reference orbit is also called the closed orbit.

The Frenet-Serret coordinate system moves along the ring on the reference orbit. The coordinates are then transverse: x and y, and longitudinal in the direction of travel: s. Figure 2.8 shows those coordinates.

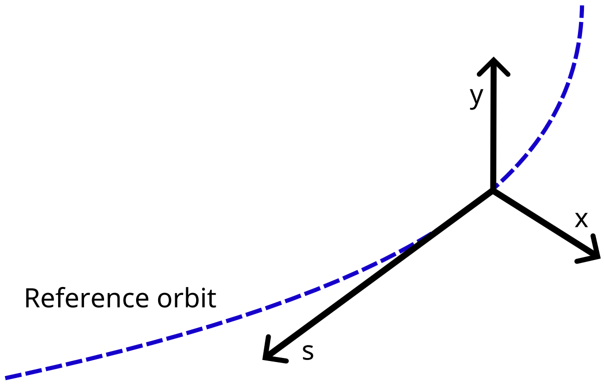

Figure 2.8.: Frenet-Serret coordinate system, commonly used in accelerator physics. The system moves along the reference orbit.

This coordinate system is widely used to simply describe a either an element's or a particle's position in the accelerator. Without any explicit mention, those are coordinates used in this thesis. It is frequent to use the variable z to refer to either x or y in equations. In order to describe the motion of particles through a lattice, different coordinate systems can be used. To better describe the motion of particles through a lattice, various coordinate systems can be employed. First, the formalism for a linear lattice will be introduced, followed by an explanation of how motion in a machine with non-linear elements can be characterized.

Linear optics refers to the regime where the forces acting on particles, such as those from dipoles and quadrupoles, are directly proportional to the particle's displacement from the reference trajectory, resulting in simple, predictable motion described by linear equations and transfer matrices. Non-linear optics, on the other hand, involves higher-order magnetic elements like sextupoles and octupoles, where the forces are non-linear with respect to displacement. This leads to more complex particle motion, which can result in phase-space distortions and chaotic trajectories.

2.3.1. Linear Lattice

Courant-Snyder Parameters

A circular accelerator is composed of many multipoles of different orders. A very basic design only requires dipoles and quadrupoles in order to operate. Dipoles are used to bend the particles in order to form the ring, whereas quadrupoles are used to focus the beam to a focal point, similar to light optics. Those elements can be arranged in a particular order, to form a FoDo cell. Such cells present an alternating placement of focusing an defocusing quadrupoles with dipoles in between, as shown in Fig. 2.9, and are usually repeated many times along the ring.

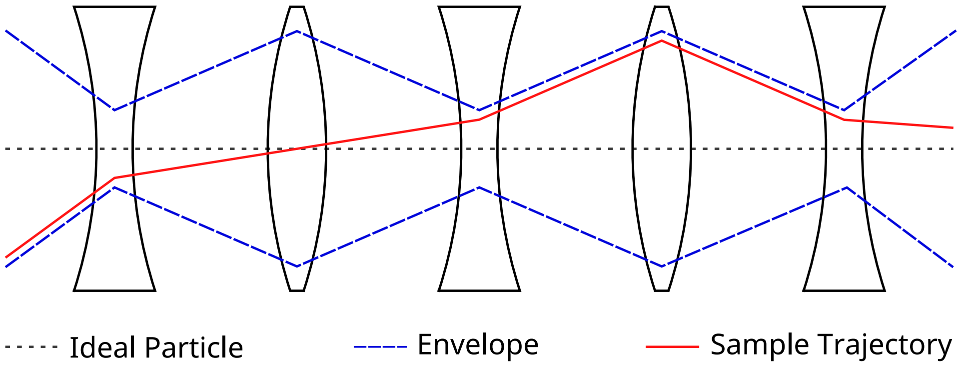

Figure 2.9.: Line composed of FoDo cells, a basic cell present in most accelerators, composed of a Focusing and a Defocusing quadrupole. The envelope is a factor of the β-function and the action J.

A lattice composed of only dipoles and quadrupoles, is referred to as a *linear* lattice. In a synchrotron, a circular particle accelerator, particles undergo transverse and longitudinal oscillations. Taking into account those oscillations, the phase-space ellipse of a particle at a position s in the ring can be described with a new system: the Courant-Snyder parameters, also know as Twiss parameters or the *optics functions* [22], as shown in Fig. 2.10.

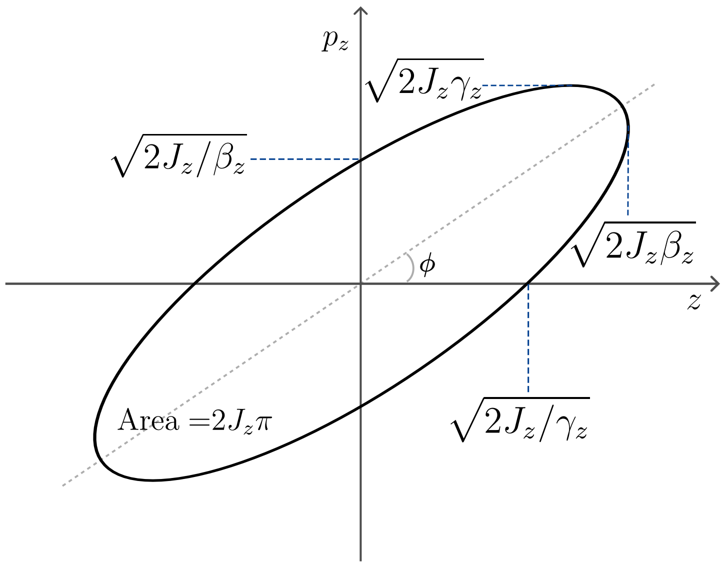

Figure 2.10.: Phase-space ellipse of a linear machine, parametrized by the Courant-Snyder parameters α, β and γ.

J, the action, an invariant of linear motion at a given energy, is related to the other quantities by:

$$J_z = \frac{1}{2}(\gamma_z \cdot z^2 + 2\alpha_z p_z \cdot z + \beta_z p_z^2). \tag{2.13}$$

The action can be related to the area in phase space, called the single particle emittance: $\epsilon = 2J$. As the β parameter varies along the ring, it is referred to as the β-function and is related to the amplitude of the oscillations. Thus, the smaller is the β-function, the smaller is also the envelope of the beam. The number of oscillations per turn is called the *tune*, and is closely related to the β-function:

2

$$Q_{x,y} = \frac{1}{2\pi} \oint \frac{1}{\beta_{x,y}(s)} \mathrm{d}s. \tag{2.14}$$

It is common to express the position of a particle using *action-angle* variables, allowing to switch between the Courant-Snyder parameters and the Frenet-Serret system:

$$\begin{aligned} z &= \sqrt{2J_z\beta_z} \cos\phi_z \\ p_z &= -\sqrt{\frac{2J_z}{\beta_z}} \left(sin\phi_z + \alpha_z \cos\phi_z\right). \end{aligned} \tag{2.15}$$

Normalized Coordinates

In order to simplify the description of the linear motion in a ring, a transformation can be applied to the previously seen coordinates. Figure Fig. 2.11 shows a phase-space described in both coordinates. The new coordinates, $\hat{z}$, and $\hat{p}_z$, are then expressed as factors of the α and β functions:

$$\begin{pmatrix} \hat{z} \\ \hat{p}_z \end{pmatrix} = \begin{pmatrix} \frac{1}{\sqrt{\beta_z}} & 0 \\ \frac{\alpha_z}{\sqrt{\beta_z}} & \sqrt{\beta_z} \end{pmatrix} \begin{pmatrix} z \\ p_z \end{pmatrix}. \tag{2.16}$$

This allows to describe the motion as a simple rotation, the new coordinates being only dependent on the invariant J_z and the phase ϕ_z:

$$\begin{aligned} \hat{z} &= \sqrt{2J_z} \cos(\phi_z), \\ \hat{p}_z &= \sqrt{2J_z} \cos(\phi_z). \end{aligned} \tag{2.17}$$

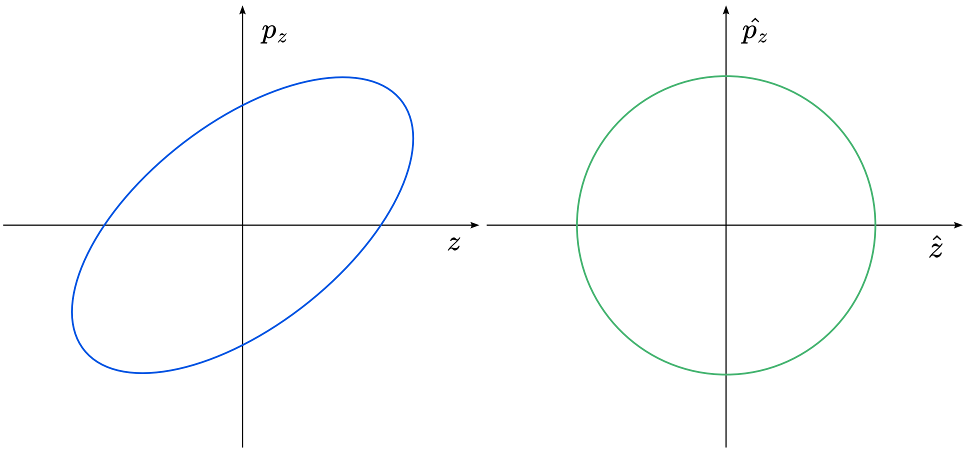

Figure 2.11.: Phase space described in both regular and normalized coordinates

Linear Transfer Maps

The final position of a particle after passing through an accelerator element can be described using *transfer maps*. In the case of linear optics, these maps take the form of matrices. Importantly, these maps are symplectic, meaning they preserve the area of phase space, ensuring that the particle's motion is accurately represented. Symplecticity guarantees that key properties of the beam, such as its emittance, remain consistent, which is crucial for maintaining the stability and integrity of particle trajectories in the accelerator. For a matrix $\mathcal{M}$ and positions z at the initial location and s, the general formula reads [23]:

$$\begin{pmatrix} z \\ z' \end{pmatrix}_s = M \cdot \begin{pmatrix} z \\ z' \end{pmatrix}_0 \tag{2.18}$$

This formalism assumes that the magnetic field is constant along the element in the longitudinal direction. Basic elements such as drifts, dipoles, quadrupoles can then be described be a simple 2×2 matrix:

$$M_{drift} = \begin{pmatrix} 1 & L \\ 0 & 1 \end{pmatrix}, \tag{2.19}$$

$$M_{dipole} = \begin{pmatrix} \cos(L/\rho) & \rho \sin(L/\rho) \\ -1/\rho \sin(L/\rho) & \cos(L/\rho) \end{pmatrix}, \tag{2.20}$$

$$M_{focusing\ quad.} = \begin{pmatrix} \cos\left(\sqrt{k_2}L\right) & 1/\sqrt{k_2}\sin\left(\sqrt{k_2}L\right) \\ -\sqrt{k_2}\sin\left(\sqrt{k_2}L\right) & \cos\left(\sqrt{k_2}L\right) \end{pmatrix}, \tag{2.21}$$

$$M_{defocusing\ quad.} = \begin{pmatrix} cosh\left(\sqrt{|k_2|}L\right) & 1/\sqrt{|k_2|}sinh\left(\sqrt{|k_2|}L\right) \\ \sqrt{|k_2|}sinh\left(\sqrt{|k_2|}L\right) & cosh\left(\sqrt{|k_2|}L\right) \end{pmatrix}, \tag{2.22}$$

where L is the length of the element, ρ the radius of curvature of the orbit and k_2 the normalized strength of quadrupoles. In the case of quadrupoles, a focusing matrix should be used in the horizontal plane for focusing quadrupoles, where defocusing matrices should be used in the vertical plane. The opposite goes for defocusing quadrupoles.

Transfer matrices can be combined together to describe a larger group of elements, as the FoDo cell seen previously. Its transfer matrix can then be expressed as:

$$M_{FoDo} = M_{focusing\ quad} \cdot M_{drift} \cdot M_{defocusing\ quad} \cdot M_{drift}. \tag{2.23}$$

For a closed machine, a full revolution can be described by a so-called *one-turn map*, being the transfer matrix of the whole machine, denoted $\mathcal{M}$. Such a map can potentially contain thousands of elements.

2.3.2. Non-Linear Lattice

So far, Courant-Snyder parameters were a good way to describe the distribution of positions and velocities of particles in the transverse plane. One caveat of using this formalism is that it is restrained to linear optics and does not address non-linear elements, like octupoles. These elements generate forces that are not directly proportional to a particle's displacement from the reference trajectory. Effects such as resonances or those arising from an arrangement of several multipoles together can be described by the concepts introduced in this section. An overview of the needed mathematical tools is first given, before introducing maps.

Lie Algebra

One way to describe non-linear effects is to introduce Lie Algebra [24], a powerful algebra able to describe transformations, symmetries and their associated conserved quantities. The Lie algebra is a vector space, denoted $\mathfrak{g}$, equipped with a binary operation called the *Lie bracket* and denoted $[x, y]$ for two vectors x and y. Any vector space equipped with a Lie bracket (or commutator) satisfying the following conditions is called a Lie algebra:

- Bilinearity:

$$
\begin{aligned}
[ax + by, z] &= a[x, z] + b[y, z], \\
[z, ax + by] &= a[z, x] + b[z, y], \quad \forall x, y, z \in \mathfrak{g} \text{ and } a, b \text{ scalars}
\end{aligned}
\tag{2.24}
$$

- Alternativity:

$$
[x, x] = 0, \quad \forall x \in \mathfrak{g} \tag{2.25}
$$

- Anticommutativity:

$$
[x, y] = -[y, x], \quad \forall x, y \in \mathfrak{g} \tag{2.26}
$$

- The Jacobi identity:

$$
[x, [y, z]] + [y, [z, x]] + [z, [x, y]] = 0, \quad \forall x, y, z \in \mathfrak{g} \tag{2.27}
$$

The *Lie bracket*, plays a central role in the Lie algebra. It describes how dynamical variables evolve under infinitesimal symplectic transformations.

Poisson Brackets

In accelerator physics, following the Hamiltonian formalism and classical mechanics, the commutator is represented by the *Poisson brackets*, which satisfy the necessary conditions for describing particle motion [24, 25]. Poisson brackets are used to express continuous symmetries, conserved quantities, and the time evolution of dynamical variables within the system.

Let's consider position and momentum coordinates $q_i \cdots q_n$ and $p_i \cdots p_n$ of a 2n-dimensional phase space. Usually, those would be x, y, p_x and p_y for transverse coordinates. The Poisson brackets of two functions f and g is then defined by:

$$
[f, g] = \sum_{i=1}^{n} \frac{\partial f}{\partial q_i} \frac{\partial g}{\partial p_i} - \frac{\partial f}{\partial p_i} \frac{\partial g}{\partial q_i}. \tag{2.28}
$$

The evolution of coordinates and momenta in time is described by Hamilton's equations of motion, which can be naturally expressed with Poisson brackets:

$$
\begin{aligned}
\frac{\partial H}{\partial p_i} = \frac{\mathrm{d}q_i}{\mathrm{d}t} &= [q_i, H] \\
-\frac{\partial H}{\partial q_i} = \frac{\mathrm{d}p_i}{\mathrm{d}t} &= [p_i, H].
\end{aligned}
\tag{2.29}
$$

2

Lie Operator

Given a function f, a differential operator called *Lie operator* is defined, and is closely related to the previously seen Poisson bracket:

$$:f: = \sum_{i=1}^{n} \frac{\partial f}{\partial q_i}\frac{\partial}{\partial p_i} - \frac{\partial f}{\partial p_i}\frac{\partial}{\partial q_i}. \tag{2.30}$$

The action of this operator on a function g is equivalent to the Poisson brackets, as in:

$$:f:g = [f, g]. \tag{2.31}$$

A particular power series of this Lie operator can now be defined, called *Lie transformation*:

$$\begin{aligned} e^{:f:}g &= \sum_{l=0}^{\infty} \frac{1}{l!} :f:^l g \\ &= g + [f, g] + \frac{1}{2!}[f, [f, g]] + \cdots . \end{aligned} \tag{2.32}$$

Non-Linear Transfer Maps

As introduced in Section 2.3.1, the dynamics of a particle beam in a circular accelerator can be described by *transfer maps*. A symplectic *One Turn Map* $\mathcal{M}$ that includes N non-linear elements is defined [24] as:

$$\mathcal{M} = e^{:h_N:} \cdot e^{:h_{N-1}:} \cdots e^{:h_1:} \cdot \mathcal{R} \tag{2.33}$$

where $\mathcal{R}$ is a matrix describing the linear motion over one turn and the h_i terms representing the Hamiltonian of each non-linear elements of the machine. Via the Baker-Campbell-Hausdorff (BCH) theorem [26, 27], previous Lie transformations can be combined and simplified via Eq. (2.34) and Eq. (2.35). Further orders can be found and computed via [27].

$$e^{:h_1:} \cdot e^{:h_2:} = e^{:h:} \tag{2.34}$$

with

$$\begin{aligned} h =& h_1 + h_2 && \Rightarrow 1^{\text{st}} \text{ order} \\ &+ \frac{1}{2}[h_1, h_2] && \Rightarrow 2^{\text{ nd}} \text{ order} \\ &+ \frac{1}{12}[h_1, [h_1, h_2]] - \frac{1}{12}[h_2, [h_1, h_2]] && \Rightarrow 3^{\text{rd}} \text{ order} \\ &+ \cdots . \end{aligned} \tag{2.35}$$

The one turn map is thus expressed as a single Lie transformation:

$$\mathcal{M} = e^{:h:} \cdot \mathcal{R}. \tag{2.36}$$

In most cases, where the non-linear perturbations are small, the above series converges quickly and only the first order of Eq. (2.35) is used [28]. The resulting expression is then more elegant, being a simple sum of the Hamiltonians of the N non-linear elements:

$$\mathcal{M} = e^{:h_1 + h_2 + \cdots + h_N:} \cdot \mathcal{R}. \tag{2.37}$$

It is though to be noted that in this thesis experimental measurements show the evidence of higher order contributions. In order to fully understand the combined effect of multipoles, the BCH expansion needs to be expended further than the first two terms.

When transporting coordinates from one point to another, the length of the elements must be taken into account:

$$\begin{aligned} e^{:LH:} x_0 &= x_1, \\ e^{:LH:} p_0 &= p_1. \end{aligned} \tag{2.38}$$

Normal Form

As non-linearities are introduced in the machine, the phase-space becomes distorted, resulting in J_z no longer being an invariant of motion. The previously seen normalization does not work anymore and the phase-space is no longer a simple circle. A new normalization is then introduced, called the *normal form*, with complex coordinates ζ, depending on new action and angle coordinates I_z and ψ_z:

$$\zeta_{z,\pm} = \sqrt{2I_z} e^{\mp i\psi_z}. \tag{2.39}$$

An exaggerated vision of such a phase-space in Courant-Snyder, normalized, and normal form coordinates can be seen in Fig. 2.12.

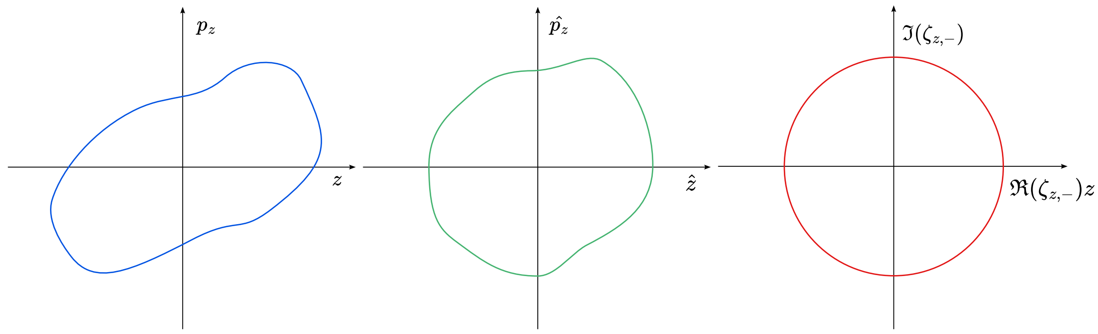

Figure 2.12.: Exaggerated phase space distorted by non-linearities described in regular (left), normalized (middle) and normal form (right) coordinates.

The map defined previously in Eq. (2.36) can be rewritten in order to retrieve an invariant of motion I_z by introducing a generating function F:

$$\tilde{\mathcal{M}} = e^{:-F:}\mathcal{M}e^{:F:} \tag{2.40}$$

Such a generating function includes all the non-linearities, simplifying the calculations. Going back and forth from normalized to normal forms coordinates is then straightforward, as depicted in Fig. 2.13. The hamiltonian H is now only dependent on the action I_z.

$$\begin{tikzcd}
(\hat{z} \pm i\hat{p}_z)_N \arrow[r, "\hat{\mathcal{M}}"] \arrow[d, "e^{:-F:}"'] & (\hat{z} \pm i\hat{p}_z)_{N+1} \\
\zeta_N \arrow[r, "e^{:H:} \cdot \mathcal{R}"'] & \zeta_{N+1} \arrow[u, "e^{:F:}"']
\end{tikzcd}$$

Figure 2.13.: A one turn map from turn N to N+1 solved using a generating function F, transforming to normal form coordinates ζ, applying the linear rotation R and transforming back to normalized coordinates.

The function F is defined as

$$F = \sum_{jklm} f_{jklm}\zeta_{x,+}^{j}\zeta_{x,-}^{k}\zeta_{y,+}^{l}\zeta_{y,-}^{m}, \tag{2.41}$$

where f_{jklm} are the so-called Resonance Driving Terms (RDTs). The summation $jklm$ is done over all the combinations of j, k, l and m with $j + k + l + m = n$ for a multipole of order n, as shown in

Eq. (2.42):

$$\sum_{jklm} = \sum_{j=0}^{n}\sum_{k=0}^{n}\sum_{l=0}^{n}\sum_{m=0}^{n} \quad ; \quad j+k+l+m=n. \tag{2.42}$$

The expression of the resonance driving terms is given by the global hamiltonian term h_jklm by

$$f_{jklm} = \frac{h_{jklm}}{1-e^{i2\pi\left[(j-k)Q_x+(l-m)Q_y\right]}}, \tag{2.43}$$

where this coefficient is a summation over the hamiltonian terms of elements w in the lattice,

$$h_{jklm} = \sum_w h_{w,jklm} e^{i\left[(j-k)\Delta\phi_x+(l-m)\Delta\phi_y\right]}. \tag{2.44}$$

The expression of $h_{w,jklm}$ is itself derived from the general hamiltonian of Eq. (2.11) by applying a multinomial expansion on the coordinates [29] as shows Eq. (2.45). Derivations and more information on resonance driving terms can be found in Appendix C.

$$h_{w,jklm} = -\Re\left[\frac{K_{w,n}+iJ_{w,n}}{j!k!l!m!2^{j+k+l+m}} i^{l+m} \beta_{w,x}^{\frac{j+k}{2}} \beta_{w,y}^{\frac{l+m}{2}}\right] \tag{2.45}$$

Transforming from the normal form coordinates back to the original normalized coordinates can be done using the right side of Fig. 2.13. Which is written, to second order, as:

$$\begin{aligned} h_z^{\pm} &= e^{:F:}\cdot\zeta_z^{\pm} \\ &\simeq \zeta_z^{\pm} + \left[F,\zeta_z^{\pm}\right] + \frac{1}{2!}\left[F,\left[F,\zeta_z^{\pm}\right]\right]. \end{aligned} \tag{2.46}$$

Using this equation to the first order and Eq. (2.39), the normalized coordinates can be expressed after N turns in Eq. (2.47).

$$\begin{aligned} (x-ip_x)(N) = &\sqrt{2I_x}e^{i(2\pi Q_x N+\psi_{x_0})} - \\ &2i\sum_{jklm} jf_{jklm}(2I_x)^{\frac{j+k-1}{2}}(2I_y)^{\frac{l+m}{2}} e^{i\left[(1-j+k)(2\pi Q_x N+\psi_{x_0})+(m-l)(2\pi Q_y N-\psi_{y_0})\right]} \\ (y-ip_y)(N) = &\sqrt{2I_y}e^{i(2\pi Q_y N+\psi_{y_0})} - \\ &2i\sum_{jklm} lf_{jklm}(2I_x)^{\frac{j+k}{2}}(2I_y)^{\frac{l+m-1}{2}} e^{i\left[(k-j)(2\pi Q_x N+\psi_{x_0})+(1-l+m)(2\pi Q_y N-\psi_{y_0})\right]}. \end{aligned} \tag{2.47}$$

This equation highlights the contribution of the non-linear elements to the motion of the particles.

Spectral lines arising from these contributions are discussed in Section 2.7.2. It is though to be observed that some f_{jklm} terms will not contribute to the motion in a given plane due to the dependence on j or l.

2

2.4. Examples of Maps

It is important to remember that two expansions are used when creating non linear transfer maps. When referring to the order of a map, it is the order of the BCH formula, used to combine Hamiltonians, that is referred to. The Lie transformation to transport the coordinates themselves is usually only taken to the first order.

2.4.1. Non-Linear Transfer of a Single Sextupole

Here, we are interested on the effect of a single sextupole on the regular frenet-serret coordinates x, y, p_x and p_y. Let's consider a sextupole with strength K_3 and a normal field,

$$H_3 = \frac{1}{6}K_3(x^3 - 3xy^2). \tag{2.48}$$

A transfer map, from longitudinal coordinate s_0 to s_1, consisting of only this element is the following:

$$\begin{pmatrix} x \\ p_x \\ y \\ p_y \end{pmatrix}_{s_1} = e^{L:H_3:} \begin{pmatrix} x \\ p_x \\ y \\ p_y \end{pmatrix}_{s_0}, \tag{2.49}$$

where L is the length of the multipole. Using Eq. (2.32) to expand the Lie transformation to the first order, it can be rewritten as

$$\begin{aligned} e^{L:H_3:}x &= x + [L \cdot H_3, x], \\ e^{L:H_3:}p_x &= p_x + [L \cdot H_3, p_x], \\ e^{L:H_3:}y &= y + [L \cdot H_3, y], \\ e^{L:H_3:}p_y &= p_y + [L \cdot H_3, p_y]. \end{aligned} \tag{2.50}$$

Applying the poisson bracket of Eq. (2.28) on x or y yields 0, as neither the Hamiltonian nor x and y are dependent on p_x and p_y.

$$[L\cdot H_3, x] = \overbrace{\frac{\partial(L\cdot H_3)}{\partial x}\frac{\partial x}{\partial p_x}}^{0} - \overbrace{\frac{\partial(L\cdot H_3)}{\partial p_x}\frac{\partial x}{\partial x}}^{0} + \underbrace{\frac{\partial(L\cdot H_3)}{\partial y}\frac{\partial x}{\partial p_y}}_{0} - \underbrace{\frac{\partial(L\cdot H_3)}{\partial p_y}\frac{\partial x}{\partial y}}_{0} \tag{2.51}$$
$$= 0.$$

The poisson bracket applied on p_x or p_y though evaluates to a non-zero value, as the momentum is present in $p_{x,y}$ while x, y are present in the Hamiltonian:

$$[L\cdot H_3, p_x] = \frac{\partial(L\cdot H_3)}{\partial x}\frac{\partial p_x}{\partial p_x} - \overbrace{\frac{\partial(L\cdot H_3)}{\partial p_x}\frac{\partial p_x}{\partial x}}^{0} + \underbrace{\frac{\partial(L\cdot H_3)}{\partial y}\frac{\partial p_x}{\partial p_y}}_{0} - \underbrace{\frac{\partial(L\cdot H_3)}{\partial p_y}\frac{\partial p_x}{\partial y}}_{0} \tag{2.52}$$
$$= \frac{1}{2}K_3L(x^2 - y^2)$$

The same method is used for p_y. The final form of the transfer map Eq. (2.49) is then the following:

$$\begin{pmatrix} x \\ p_x \\ y \\ p_y \end{pmatrix}_{s_1} = \begin{pmatrix} 1 & & & \\ & 1 + \left(\frac{1}{2p_x}K_3L(x^2 - y^2)\right) & & \\ & & 1 & \\ & & & 1 - \left(\frac{1}{p_y}K_3Lxy\right) \end{pmatrix} \begin{pmatrix} x \\ p_x \\ y \\ p_y \end{pmatrix}_{s_0}. \tag{2.53}$$

It is not necessary to go higher than the first order, as the second order of the expansion of the Lie transformation is 0 ; p_x is indeed not present in the result of the first poisson bracket:

$$\begin{aligned} \frac{1}{2!}[L\cdot H_3, [L\cdot H_3, p_x]] &= \frac{1}{2!}\left[L\frac{1}{6}K_3(x^3 - 3xy^2), \left[L\frac{1}{6}K_3(x^3 - 3xy^2), p_x\right]\right] \\ &= \frac{1}{2!}\left[L\frac{1}{6}K_3(x^3 - 3xy^2), \frac{1}{2}K_3L(x^2 - y^2)\right] \\ &= \frac{1}{2!}\cdot 0 \\ &= 0 \end{aligned} \tag{2.54}$$

2.4.2. Non-Linear Transfer of Two Sextupoles

We saw previously that a single sextupole only acts as a sextupole when it is alone in the transfer map, which is expected. Let's now consider two sextupoles which hamiltonians are denoted H_1 and H_2.

2

Creating a map consisting of only two sextupoles does not make much sense, as it finally results in one sextupole as their coordinates are the same. Instead, a drift is added between the two elements. The Hamiltonian of a drift of length L_D is given by [30],

$$D = -\frac{L_D}{2}(p_x^2 + p_y^2). \tag{2.55}$$

The application of the lie transformation on the canonical coordinates is then very simple, as no higher orders arise ($[D, [D, x]] = 0$):

$$\begin{aligned} e^{:D:}x &= x + L_D p_x, \\ e^{:D:}p_x &= p_x. \end{aligned} \tag{2.56}$$

The transfer map of such a line is then the following,

$$\mathcal{M} = e^{:Z:} = e^{:H_2:} \cdot e^{D:H_1:}, \tag{2.57}$$

describing the evolution of coordinates from a longitudinal position s_0 to s_1,

$$\begin{pmatrix} x \\ p_x \\ y \\ p_y \end{pmatrix}_{s_1} = \mathcal{M} \cdot \begin{pmatrix} x \\ p_x \\ y \\ p_y \end{pmatrix}_{s_0} \tag{2.58}$$

In order to combine those elements, the BCH formula from Eq. (2.35) is used, presented here to the third order for two elements,

$$Z = \underbrace{H_2 + H_1}_{\text{First order}} + \underbrace{\frac{[H_2, H_1]}{2}}_{\text{Second order}} + \underbrace{\frac{[H_2, [H_2, H_1]]}{12} - \frac{[H_1, [H_2, H_1]]}{12}}_{\text{Third order}} \tag{2.59}$$

First Order To the first order, the resulting effective hamiltonian is only the summation of two sextupoles.

Second Order The drift added to change the coordinates of H_1 allows the poisson bracket to evaluate to a non-zero value. Octupolar-like terms indeed appear in the effective hamiltonian. From this, it can be inferred that two sextupoles will interact together and introduce effects like amplitude detuning, second order chromaticity and RDTs. Details of the derivation can be found in Appendix A.

Third Order To the third order, even higher orders such as decapolar-like effects appear. Such effects include the third order chromaticity, chromatic amplitude detuning and RDTs.

Remark It is to be noted that while sextupoles do introduce higher-order terms, these are often designed to be small in comparison to those brought by the actual higher-order multipoles, making them thus often negligible. Such is the case in the LHC.

2.5. Observables

2.5.1. Dispersion

Treating a beam as a single particle having the design momentum p_0 leads to a machine with no apparent ill effect related to that momentum. However, when considering a particle beam where each particle follows a distribution in momentum, a few effects arise from this deviation, called the *momentum offset*, δ. It is defined as a relative difference to the design momentum:

$$\delta = \frac{p - p_0}{p_0}. \tag{2.60}$$

Those effects are referred to as *chromatic aberrations*. The first and most important to consider is the *dispersion*. Dispersion results from a particle with a momentum offset being deflected differently by the dipoles compared to a particle at the design momentum. Figure 2.14 shows an example of deflection. The particle is still subject to the other properties of the lattice, but with a different orbit, described by the dispersion function in Eq. (2.61).

$$\begin{aligned} D_x(s) &= \frac{\Delta x(s)}{\delta} \\ D_y(s) &= \frac{\Delta y(s)}{\delta}. \end{aligned} \tag{2.61}$$

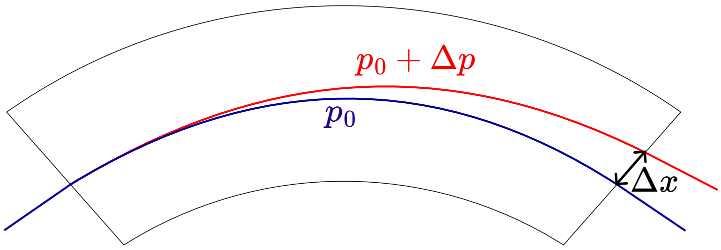

Figure 2.14.: Particles with a momentum offset will be deflected differently by dipoles. This offset in position can be described by the dispersion function.

Momentum Compaction Factor In synchrotrons, particles with a deviation in momentum with respect to the reference particle will experience a different path length due to the bending of the dipoles. This effect is characterized by the *momentum compaction factor* [15],

$$\alpha_c = \frac{\Delta C/C}{\delta}, \tag{2.62}$$

relating the circumference of the ring C to the momentum offset δ. A positive momentum compaction factor indicates a longer path traveled by particles with a positive momentum offset, and vice versa.

The momentum compaction factor can also be broken down into orders as an infinite sum, where the constant term is often referred to as the first order,

$$\alpha_c = \underbrace{\alpha_{c,0}}_{\text{Constant term}} + \underbrace{\sum_{i\geq 1} \alpha_{c,i}\delta^i}_{\text{Linear and non linear terms}} . \tag{2.63}$$

In the LHC, the contribution from the non constant terms is negligible [31]. Further details can be found in Section 6.2.1.

2.5.2. β-function

As seen previously in Section 2.3.1, the β-function is related to the amplitude of oscillations of the beam. Figure 2.15 shows how the β-function oscillates along the ring due to quadrupoles focusing and defocusing properties. The β-function is an important quantity found as a factor in several other observables that will be described later in this thesis.

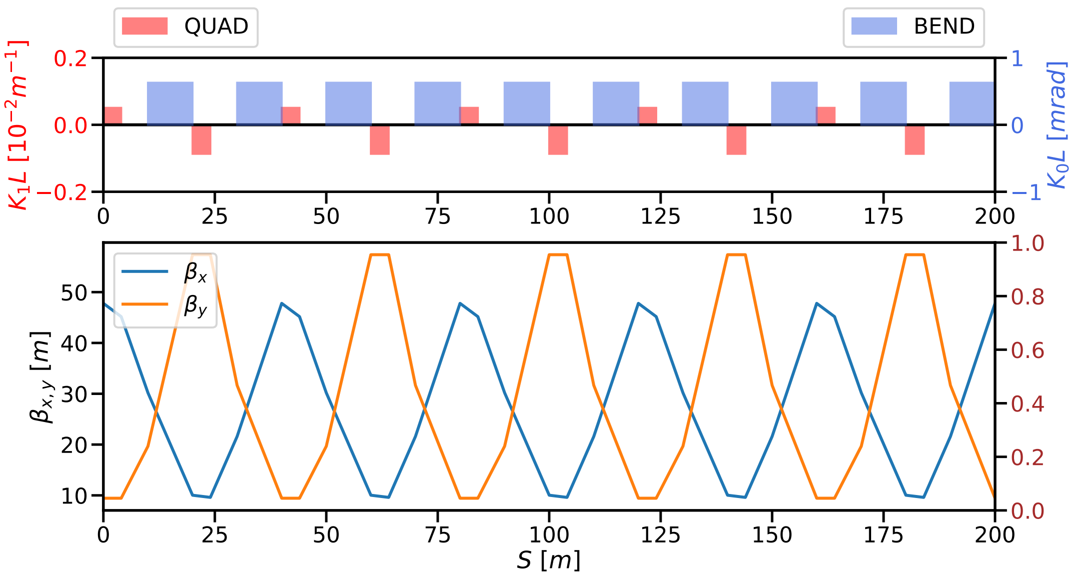

Figure 2.15.: Evolution of the β-function along the lattice. Horizontal and vertical beatings are usually opposite given the focusing and defocusing properties of quadrupoles in each plane.

A difference in β-function compared to the design leads to possibly unstable and larger beams, degrading its properties and making it harder to control. The relative difference in β-function is called the beta-beating, expressed in percents:

$$\beta - \text{beating}\ [\%] = \frac{\beta_z(s) - \beta_z(s)_{model}}{\beta_z(s)_{model}}. \tag{2.64}$$

2.5.3. Coupling

In a perfect scenario, the particle motion of each transverse plane is independent, or *uncoupled*. In practice, this transverse motion can be altered by some magnetic elements, giving rise to *betatron coupling* where the motion of each plane is not independent anymore. Such elements can be quadrupoles, mounted with a roll error introducing skew-quadrupolar fields, which are the main source of linear coupling in the LHC [13]. Field imperfections, solenoids and feed-down from higher orders can also contribute to coupling.

The resonances $Q_x + Q_y$ and $Q_x - Q_y$, called the *sum* and *difference* resonances, are mainly excited by skew quadrupoles. When coupling is present in the machine, the former may lead to unstable motion while the latter introduces an periodic exchange of emittance between the planes, keeping it stable. They can be characterized by the RDTs f_{1010} and f_{1001}.

Effects of normal multipoles start showing their skew counterpart (and vice versa) as the motion of transverse planes become coupled. This is demonstrated in Chapter 4 with octupoles.

2.6. Detuning Effects

2

2.6.1. Chromaticity

Chromaticity is the tune change ΔQ relative to the momentum offset δ. Chromaticity can be described by a Taylor expansion, given by

$$Q(\delta) = Q_0 + Q'\delta + \frac{1}{2!}Q''\delta^2 + \frac{1}{3!}Q'''\delta^3 + O(\delta^4). \tag{2.65}$$

Or, more generally, rewritten as a sum to include all orders up to n:

$$Q(\delta) = Q_0 + \sum_{i=1}^{n} \frac{1}{i!} Q^{(i)} \delta^i. \tag{2.66}$$

The first order of the chromaticity expansion, Q', is generally simply referred to as *chromaticity*, sometimes as *linear chromaticity*. The other terms are thus referred to as *non-linear chromaticity*.

The chromaticity change induced by a single element of order n and length L can be derived from the Hamiltonian of Eq. (2.11), averaging over the phase variables and differentiating relative to the actions $J_{x,y}$ and the momentum offset δ:

$$\Delta Q^{(n)}_{x,y} = \frac{\partial^n Q_{x,y}}{\partial^n \delta} = \frac{1}{2\pi} \int_L \left\langle \frac{\partial^{(n+1)} H}{\partial J_{x,y} \partial^n \delta} \right\rangle \mathrm{d}s. \tag{2.67}$$

Detailed derivations are provided in [32], and an example is presented in the following section.

Linear Chromaticity from Sextupoles The first order chromaticity Q' is contributed to by sextupoles in the presence of off-momentum particles. The normal field of a sextupole, following Eq. (2.12) is given by

$$\mathcal{N}_3(x, y) = \frac{1}{3!}(x^3 - 3xy^2). \tag{2.68}$$

As the momentum offset δ introduces a change in orbit via dispersion [33], a variable change can be operated on both x and y, as shown in Eq. (2.69). In this thesis, vertical dispersion will be though neglected.

$$\begin{aligned} x &\longrightarrow x + \Delta x = x + D_x\delta \\ y &\longrightarrow y + \Delta y = y + D_y\delta \end{aligned} \tag{2.69}$$

The positions x and y can once be replaced, using the twiss parameters, giving the full expression:

$$\begin{aligned} \mathcal{N}_3(x+\Delta x, y) = \frac{1}{6}K_3\Bigg[&\left(\sqrt{2J_x\beta_x}\cos\phi_x\right)^3 \\ &+ 3\left(\sqrt{2J_x\beta_x}\cos\phi_x\right)^2 D_x\delta \\ &+ 3\left(\sqrt{2J_x\beta_x}\cos\phi_x\right) D_x^2\delta^2 \\ &+ D_x^3\delta^3 \\ &- 3\left(\sqrt{2J_x\beta_x}\cos\phi_x\right)\left(\sqrt{2J_y\beta_y}\cos\phi_y\right)^2 \\ &- 3D_x\delta(\sqrt{2J_y\beta_y}\cos\phi_y)^2\Bigg] \end{aligned} \tag{2.70}$$

Averaging over the phase variables removes any odd cosine:

$$\begin{aligned} \langle\mathcal{N}_3(x+\Delta x, y)\rangle = \frac{1}{6}K_3\Big(&3J_x\beta_x D_x\delta \\ &+ D_x^3\delta^3 \\ &- 3D_x\delta J_y\beta_y\Big) \end{aligned} \tag{2.71}$$

The chromaticity can then be obtained by differentiating relative to the action $J_{x,y}$ to retrieve the tune, and finally by the momentum offset δ, as presented in Eq. (2.72). In the presence of second order dispersion [33], sextupoles will generate some amount of Q'', usually negligible in the LHC.

$$\begin{aligned} \Delta Q'_x &= \frac{1}{2\pi}\int_L \frac{\partial^2\langle\mathcal{N}_3\rangle}{\partial J_x\partial\delta}\,\mathrm{d}s \quad ; \quad & \Delta Q'_y &= \frac{1}{2\pi}\int_L \frac{\partial^2\langle\mathcal{N}_3\rangle}{\partial J_y\partial\delta}\,\mathrm{d}s \\ &= \frac{1}{2\pi}L\frac{1}{2}K_3\beta_x D_x & &= -\frac{1}{2\pi}L\frac{1}{2}K_3\beta_y D_x \\ &= \frac{1}{4\pi}K_3 L\beta_x D_x & &= -\frac{1}{4\pi}K_3 L\beta_y D_x \end{aligned} \tag{2.72}$$

Non-Linear Chromaticity Higher orders of the chromaticity function are described in [32] and follow the same logic as for the linear chromaticity from sextupoles. A general formula can be found for the chromaticity of order n, $n > 2$, relating a chromaticity of order n with a multipole of order $n+2$:

$$\begin{aligned} \Delta Q_x^{(n)} &= \frac{1}{4\pi} K_{n+2} L \beta_x D_x^n \\ \Delta Q_y^{(n)} &= -\frac{1}{4\pi} K_{n+2} L \beta_x D_x^n \end{aligned} \tag{2.73}$$

2.6.2. Amplitude Detuning

Amplitude detuning is a tune shift induced by the amplitude of oscillations of a particle. This detuning is directly related to the single particle emittance and can be described via a Taylor expansion around the emittance of both planes, ϵ_x and ϵ_y. Equation (2.74) shows this expansion up to the second order. Further expansions can be found in [32].

$$\begin{aligned} Q_z(\epsilon_x, \epsilon_y) = Q_{z0} &+ \left(\frac{\partial Q_z}{\partial \epsilon_x} \epsilon_x + \frac{\partial Q_z}{\partial \epsilon_y} \epsilon_y \right) \\ &+ \frac{1}{2!} \left(\frac{\partial^2 Q_z}{\partial \epsilon_x^2} \epsilon_x^2 + 2 \frac{\partial^2 Q_z}{\partial \epsilon_x \partial \epsilon_y} \epsilon_x \epsilon_y + \frac{\partial^2 Q_z}{\partial \epsilon_y^2} \epsilon_y^2 \right) + \ldots \end{aligned} \tag{2.74}$$

The first order terms of amplitude detuning are generated by octupoles, and to some extent by sextupoles when considering their higher order contributions. Those higher contributions are usually measurable but small compared to the ones of normal octupoles in the LHC. Further derivations can be found in Appendix B.

2.6.3. Chromatic Amplitude Detuning

Similar to amplitude detuning, *chromatic amplitude detuning* is a tune shift induced by the amplitude of oscillations of a particle but with an additional dependence on the momentum offset. This effect can be described by a Taylor expansion around the emittance of both planes ϵ_x, ϵ_y, and the momentum offset δ. Equation (2.75) shows this expansion up to the second order. Both the emittance ϵ and the action J can be seen to describe the chromatic amplitude detuning as terms are interchangeable with $\epsilon_{x,y} = 2J_{x,y}$. This expansion being more general than the ones of chromaticity or amplitude detuning, is it to be expected to retrieve those terms here as well.

$$
\begin{aligned}
Q_z(\epsilon_x, \epsilon_y, \delta) = Q_{z0} &+ \left[\frac{\partial Q_z}{\partial \epsilon_x}\epsilon_x + \frac{\partial Q_z}{\partial \epsilon_y}\epsilon_y + \frac{\partial Q_z}{\partial \delta}\,\delta\right] \\
&+ \frac{1}{2!}\left[\frac{\partial^2 Q_z}{\partial \epsilon_x^2}\epsilon_x^2 + \frac{\partial^2 Q_z}{\partial \epsilon_y^2}\epsilon_y^2 + \frac{\partial^2 Q_z}{\partial \delta^2}\,\delta^2 \right.\\
&\qquad \left. + 2\frac{\partial^2 Q_z}{\partial \epsilon_x \partial \epsilon_y}\epsilon_x\epsilon_y + 2\frac{\partial^2 Q_z}{\partial \epsilon_x \partial \delta}\epsilon_x\delta + 2\frac{\partial^2 Q_z}{\partial \delta \partial \epsilon_y}\delta\epsilon_y\right] \\
&+ \ldots
\end{aligned}
\tag{2.75}
$$

Sextupolar contributions To the first order of the expansion, the only term coming from sextupoles is the linear chromaticity, seen previously in Section 2.6.1.

Octupolar contributions To the first order, the amplitude detuning terms $\frac{\partial Q_z}{\partial \epsilon_x}\epsilon_x$ and $\frac{\partial Q_z}{\partial \epsilon_y}\epsilon_y$ are contributed to by octupoles. The second order chromaticity Q'' appears when expanding to the second order.

Decapolar contributions The terms highlighted in orange, in Eq. (2.76), are the terms contributed to the first order by decapoles. Terms depending on both the emittance and the momentum offset are present, as well as the third order chromaticity Q'''. Further derivations can be found in Appendix B.

$$
\begin{aligned}
Q_z(\epsilon_x, \epsilon_y, \delta) = Q_{z0} &+ \left[\frac{\partial Q_z}{\partial \epsilon_x}\epsilon_x + \frac{\partial Q_z}{\partial \epsilon_y}\epsilon_y + \frac{\partial Q_z}{\partial \delta}\delta\right] \\
&+ \frac{1}{2!}\left[\frac{\partial^2 Q_z}{\partial \epsilon_x^2}\epsilon_x^2 + \frac{\partial^2 Q_z}{\partial \epsilon_y^2}\epsilon_y^2 + \frac{\partial^2 Q_z}{\partial \delta^2}\delta^2 \right.\\
&\qquad \left. + 2\frac{\partial^2 Q_z}{\partial \epsilon_x \partial \epsilon_y}\epsilon_x\epsilon_y + 2\frac{\partial^2 Q_z}{\partial \epsilon_x \partial \delta}\epsilon_x\delta + 2\frac{\partial^2 Q_z}{\partial \delta \partial \epsilon_y}\delta\epsilon_y\right] \\
&+ \frac{1}{3!}\left[\frac{\partial^3 Q_z}{\partial \delta^3}\delta^3 + \frac{\partial^3 Q_z}{\partial \epsilon_x^3}\epsilon_x^3 + \frac{\partial^3 Q_z}{\partial \epsilon_y^3}\epsilon_y^3 + \cdots\right]
\end{aligned}
\tag{2.76}
$$

2.6.4. Feed-Down

When a particle passes off-center through a magnet, an effect called *feed-down* appears. Feed-down is a lower order contribution created by ether mis-aligned magnets or an off-center orbit of the beam. A particle with an orbit offset will then experience the main field of the magnet and effects similar to those of lower order multipoles. The combined contributions of multipoles up to order P on a field of order n is given by the following and greatly detailed in [14]:

$$(K_n + iJ_n)^{w/feed-down} = \sum_{p=0}^{P} (K_{n+p} + iJ_{n+p}) \frac{(\Delta x + i\Delta y)^p}{p!} \tag{2.77}$$

Opposed to feed-down is feed-up, the higher order effects introduced by combinations of multipoles. This effect is though not a consequence of the beam position in a given field. This effect is explained in great details in Appendix A.

2.7. Resonances

2.7.1. Tune Diagram

The resonances discussed in this thesis are related to the optics of the accelerator. Such resonances create unstable motion and can lead to loosing particles.

Figure 2.16a shows a tune diagram where the fractional part of tunes Q_x and Q_y can be related to resonance lines excited by multipoles up to decapoles ($n = 5$). It becomes apparent that the diagram fills quickly when considering further orders, as shows Fig. 2.16b. Thankfully, the higher the multipole order, the weaker the resonances usually are as their introduced perturbations are usually smaller. This makes choosing a working point possible, even if some particles are hitting resonance lines.

When considering the resonance driving terms f_{jklm} from Eq. (2.43), it can be noted that the term diverges for particular tune values. This leads to a disproportionate increase in particles position in phase-space, eventually leading to loosing them. Resonant conditions due to the tunes can thus be described by the following condition:

$$(j - k)Q_x + (l - m)Q_y = p \quad , \quad j, k, l, m, p \in \mathcal{Z}. \tag{2.78}$$

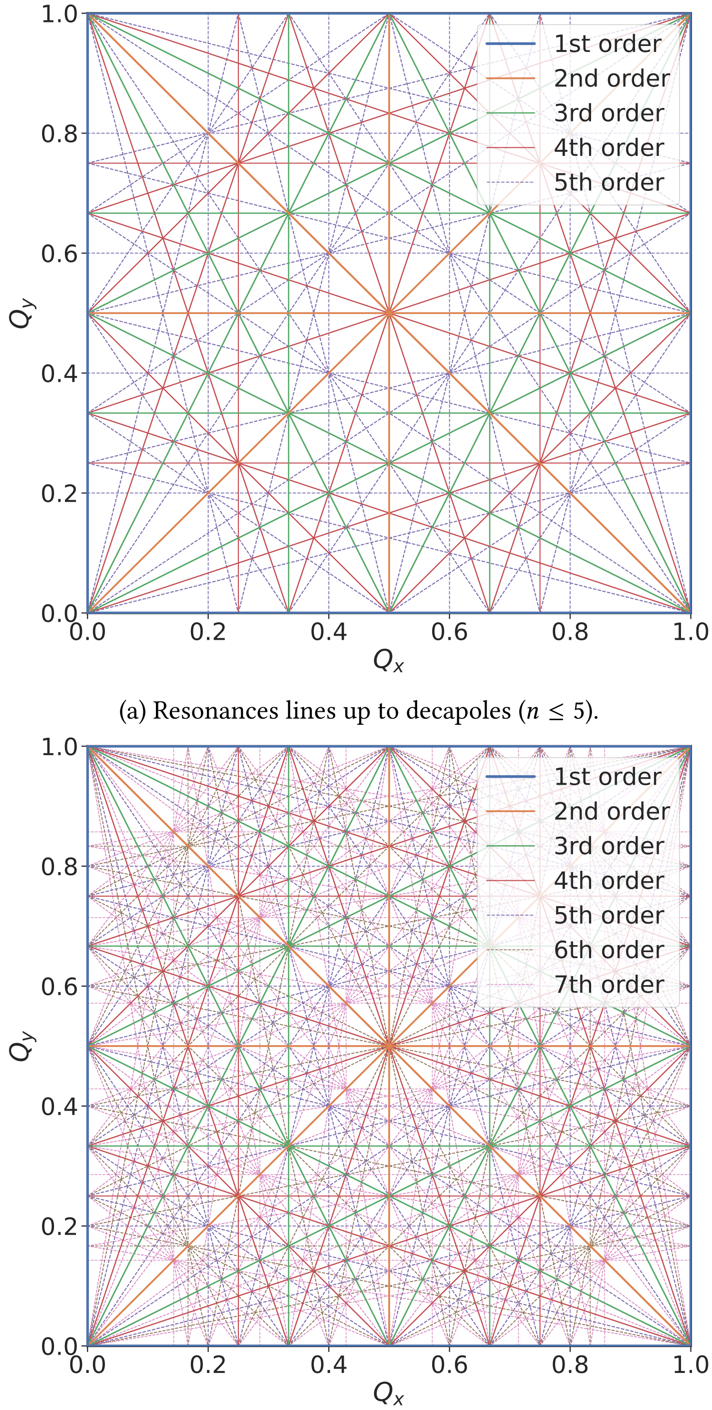

(a) Resonances lines up to decapoles ($n \leq 5$).

(b) Resonances lines up to decatetrapole ($n \leq 7$).

Figure 2.16.: Tune diagram with resonance lines excited by different multipole orders. The working point is chosen in an area where few lines are present. When considering higher orders, it becomes apparent that the beam will inevitably hit several resonances.

2

2.7.2. Frequency Spectrum

As seen in Eq. (2.47), resonance driving terms have an impact on the transverse motion of a particle. This means that performing a FFT on the turn-by-turn signal will reveal spectral lines linked to specific resonance driving terms. Each RDT f_{jklm} can thus be observed in either one or both the frequency spectrums of the horizontal and vertical planes, at multiples of $Q_x \pm Q_y$. Equation (2.79) shows where those lines would appear:

$$\begin{aligned} &H_{jklm} \quad \text{at } (1-j+k)Q_x + (m-l)Q_y \quad ; \quad j \neq 0 \\ &V_{jklm} \quad \text{at } (k-j)Q_x + (1-l+m)Q_y \quad ; \quad l \neq 0. \end{aligned} \tag{2.79}$$

The RDT f_{3000} coming from sextupoles can for example be seen in the horizontal spectrum at $(1-3+0)Q_x + (0-0)Q_y = -2Q_x$. For a value $Q_x = 0.27$, the line is seen at 0.46. No line can be seen in the vertical spectrum due to $l = 0$. Detailed tables of such lines for RDTs up to order 6 can be found in Appendix C.

The amplitude of each line will depend on the action I_z and the amplitude of the RDT [34]:

$$\begin{aligned} |H_{f_{jklm}}| &= 2j(2I_x)^{\frac{j+k-1}{2}}(2I_y)^{\frac{l+m}{2}}|f_{jklm}| \\ |V_{f_{jklm}}| &= 2l(2I_x)^{\frac{j+k}{2}}(2I_y)^{\frac{l+m-1}{2}}|f_{jklm}|. \end{aligned} \tag{2.80}$$

By reworking the previous Eq. (2.80), it can be seen that RDTs are factors of the line amplitude and the actions I_x and I_z:

$$\begin{aligned} |f_{jklm}| &= \frac{|H_{f_{jklm}}|}{2j(2I_x)^{\frac{j+k-1}{2}}(2I_y)^{\frac{l+m}{2}}} \\ |f_{jklm}| &= \frac{|V_{f_{jklm}}|}{2l(2I_x)^{\frac{j+k}{2}}(2I_y)^{\frac{l+m-1}{2}}}. \end{aligned} \tag{2.81}$$

In practice, an approximation of $J = I$ is done. The RDT is then related to the fit of the line amplitude versus the action.

3

Optics Measurements and Corrections

3.1. Beam Instrumentation

3.1.1. Beam Position Monitors

Beam Position Monitors (BPMs) are one of the most utilized and essential elements of beam diagnostics in particle accelerators. In the LHC, most of the BPMs are dual plane, and thus composed of four electrodes, distributed as two per plane. The BPM system consists of over than 550 BPMs pear beam, positioned along the ring, in the arcs and the IPs. The most common type, the *curved-button*, shown in Fig. 3.1a, is typically placed near quadrupoles [35].

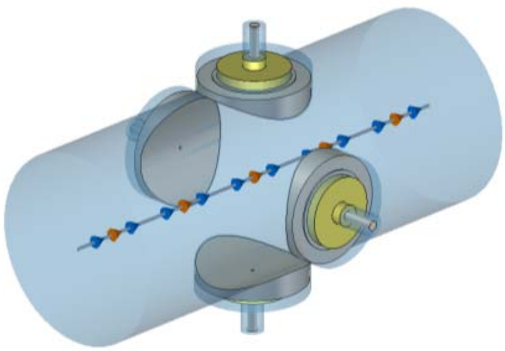

(a) Button *"BPM"* type BPM of the LHC [35].

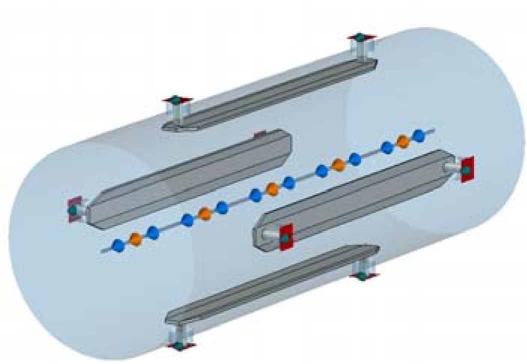

(b) Stripline *"BPMSW"* type BPM of the LHC [35].

Other pickups such as the *stripline*, shown in Fig. 3.1b, albeit more complex and expensive, offer a better signal to noise ratio and are capable of identifying the direction of the beam [35]. Such features are essential for the LHC, were both beams travel through the same aperture at the IPs.

3.1.2. Collimators

Collimators are a crucial part of the LHC. Their purpose is to protect the machine against beam losses and clean the outer parts of the beam [36]. The energy of the beams in the LHC is high enough to not only quench the magnets, but to also damage the elements.

At injection energy, with a low intensity pilot bunch, the consequences of a loss are though less severe. During Run 3, in 2022, a new collimator sequence was introduced, making a safe exploitation of the machine possible with more retracted collimators. This made measurements with higher kick amplitudes and larger orbit offsets, and thus momentum offsets, possible.

3.1.3. Beam Loss Monitors

Beam Loss Monitors are detectors mounted on various elements of the accelerator, such as magnets or collimators, to detect abnormal losses of particles. They play a crucial role in the protection of the machine, triggering a dump when losses exceed the threshold set for their respective element. BLMs use ionization chambers, working on the same principle as simple Geiger counters: a tube filled with gas, in presence of a high voltage [37]. A picture of BLMs mounted on the LHC is given in Fig. 3.2.

Dashboards in the control room are regularly used to monitor the losses along the ring when performing optics measurements, as those prove to often be destructive. An example of such a dashboard is given in Fig. 3.3.

Figure 3.2.: Beam Loss Monitors (BLM), in yellow, on the LHC [37].

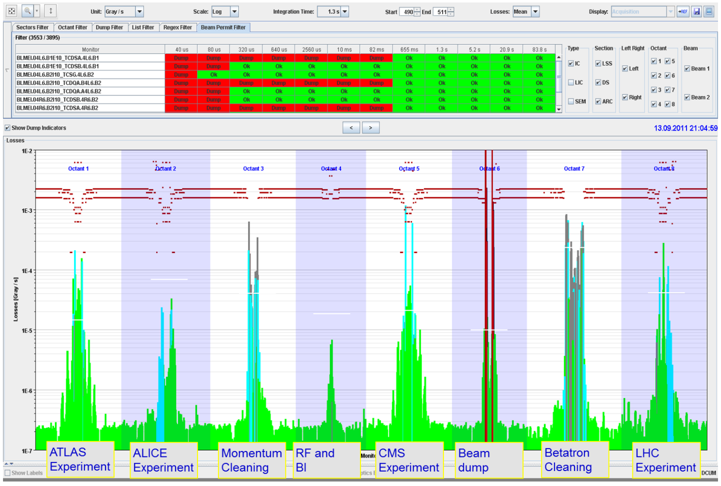

Figure 3.3.: Graphical interface used in the CERN Control Cernter (CCC) for instantaneous losses in the LHC [37]. Different parts of the accelerator have varying dump thresholds.

3.1.4. Beam Current Transformer

The Beam Current Transformer (BCT) is a device used to measure the intensity of a particle beam by detecting the current induced by the moving charge of the beam as it passes through the coil of the BCT. The beam effectively acts as a primary coil and induces a current in the secondary coil of the transformer. The BCTs are designed to be able to measure intensities from pilots bunches of 8µA to total beams of more than 860mA [38]. During optics measurements, beam intensity is often closely monitored to ensure data quality, as certain observables may not be detectable at low intensities.

3.1.5. BBQ System

The Base-Band Tune (BBQ) system in the LHC is designed to measure the beam's tune via its turn-by-turn signal. It operates by detecting and analyzing the signals of diode peak-detectors [39, 40]. The system further implements processing hardware and software, transmitting the acquired data to the control and logging systems. The system can operate with no explicit excitation, relying on the residual beam oscillations, or by using tune kickers or frequency sweeps [39].

3.1.6. AC-Dipole

The AC dipole of the LHC is a crucial component for optics studies. Its primary function is to excite the beam into large coherent oscillation, achieved by applying a sinusoidally oscillating dipole field [41]. By ramping up and down adiabatically the field, large coherent oscillations can be produced without

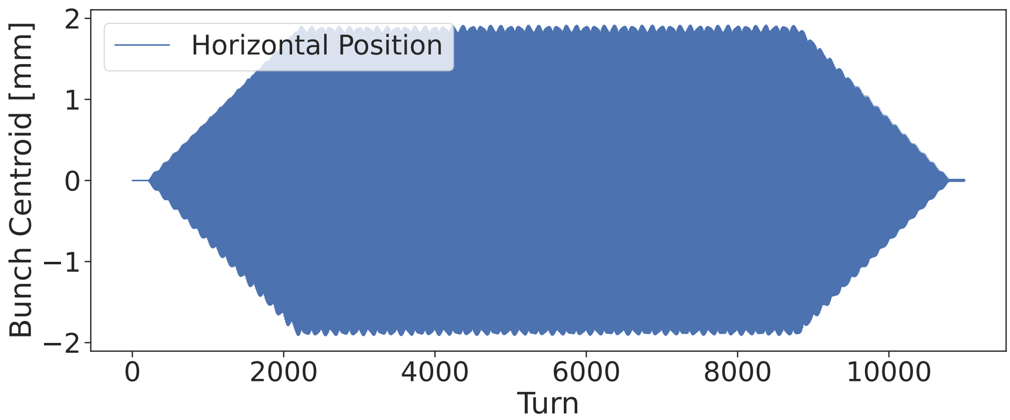

Figure 3.4.: Simulated turn by turn data with an AC-Dipole first ramping up then down.

any decoherence or emittance growth. Figure 3.4 shows an example of a simulation made with an AC-Dipole. Exciting the beam to large amplitudes make the study of linear optics, such as beta-beating easier, and that of non linear optics such as resonances possible.

The AC-Dipole is set to oscillate at a frequency Q_d, different from the natural tune of the machine Q and thus introduces systematic effects that needs to be compensated during the optics analysis. The new orbit of a particle under the influence of the AC-Dipole, at turn number n and observation point s, is given by [42]:

$$z(s,n) = \frac{BL}{4\pi\rho\delta_z} \cdot \sqrt{\beta_z(s)\beta_{z,0}} \cdot \cos\left(2\pi Q_{d,z}n + \phi_z(s) + \phi_{z,0}\right), \tag{3.1}$$

where B is the amplitude of the oscillating magnetic field, L the length of the AC-Dipole, $B\rho$ the magnetic rigidity, δ the difference between Q_d and Q, β and β_0 the beta function at the observed point and the AC-Dipole, ϕ and ϕ_0 the phase advance at the observed point and of the AC-Dipole.

3.2. Optics Measurements

To perform optics measurements, several tools and techniques are used. This section details the various implemented methods to measure specific observables.

3.2.1. Tools and Softwares

In order to perform the measurements, analysis and simulations presented in this thesis, various tools and softwares have been developed, used and contributed to.

Optics simulations have been done mainly in MAD-X [43] and PTC. MAD-NG [44] and Xsuite [45] have also been explored for specific tasks such as free RDT simulations and GPU tracking.

Analysis of chromaticity measurements are done via a newly developed graphical interface [46] written in Python. This tool makes cleaning of the raw signal data, its analysis and results export more reliable and easier.

Overall, analysis of turn-by-turn measurements is supported by a large panel of libraries written by the OMC team in Python and Java. Contributions have mainly been made to extend the following packages:

- **Beta-Beat GUI** [47], Graphical interface for turn-by-turn measurements visualization and analysis.
- **OMC3** [48], Main optics analysis and corrections software.
- **Beta-Beat.src** [49], Old analysis software, now replaced by OMC3.
- **pylhc.github.io** [50], Website of the OMC team with package documentation, examples and useful resources.

3.2.2. Turn-by-Turn Signal

One of the key data acquisition methods for optics measurements in the LHC is turn-by-turn acquisition, where beam position is collected on a per-turn basis. This process involves exciting the beam using an AC-Dipole to induce forced oscillations. Typically, a pilot bunch is used for this purpose, containing a reduced intensity of 10^{10} protons, compared to the standard operational bunch intensity of 10^{11}. The lower intensity allows for larger amplitude oscillations, enabling more precise measurements while ensuring the safety of the machine and minimizing the risk of damaging components.

A spectral analysis is then performed via a *FFT* on the signal, making apparent the driven tunes from the AC-Dipole, the transverse tunes and the possible resonance lines, as shown in Fig. 3.5.

From these oscillations and spectral lines, the optics observables, such as β-beating, dispersion, coupling, and resonance driving terms, can be reconstructed [51]. These key quantities provide valuable insights into the beam's dynamics and will be detailed further in the following sections.

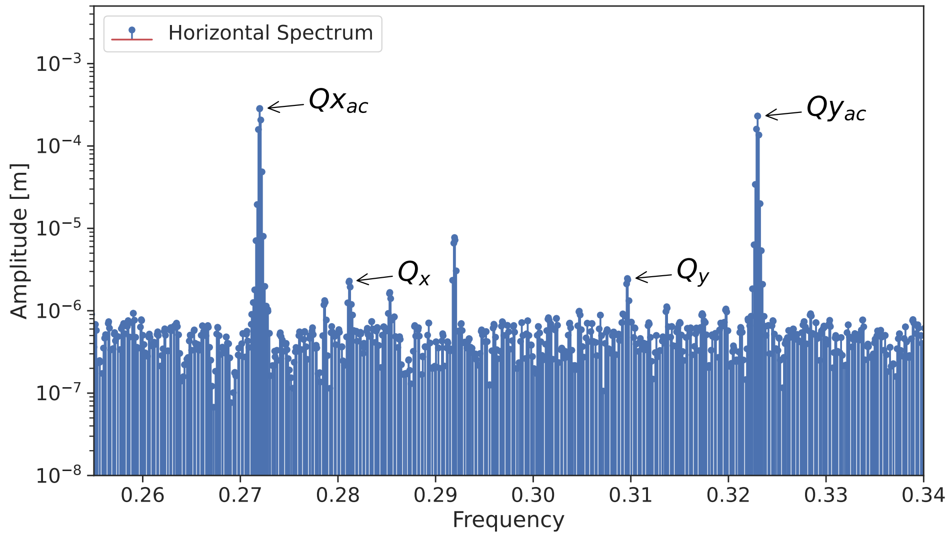

Figure 3.5.: Horizontal frequency spectrum of a turn-by-turn measurement in the LHC. The *driven* tunes of the AC-Dipoles have the highest amplitudes while the natural tune can be seen close to it. Other lines are often created by resonances.

Betatron Phase The betatron phase can be determined at a given BPM by performing an FFT on the turn-by-turn data. The angle of the main peak, the tune, is then taken to obtain the phase. The phase advance between two BPMs is simply their phase difference.

β-Beating The β-beating can be reconstructed via the phase advance between BPMs. The computation involves using a model created via a simulation software such as MAD-X. The $beta$-function at a given BPM can be calculated from the measured phases of 3 BPMs denoted i, j, k [52],

$$\beta(s_i) = \beta^{model}(s_i) \cdot \frac{\cot(\Delta\phi_{i,j}) + \cot(\Delta\phi_{i,k})}{\cot\left(\Delta\phi_{i,j}^{model}\right) + \cot\left(\Delta\phi_{i,k}^{model}\right)} \tag{3.2}$$

with $\Delta_{i,j}$ being the phase advance between BPMs i and j. Using specific phase advances between BPMs enhances the precision of the β-function measurement. This approach can also be extended to use an arbitrary number N of BPMs [53, 54]. The measurement of the β-function via phase advance is independent from BPM calibration and relies solely on the accuracy of the phase measurement.

Dispersion To retrieve the linear dispersion, turn-by-turn measurements are performed at certain momentum offsets. This allows the computation of the dispersion via the shift in mean orbit Δz and the momentum offset δ,

$$D_z = \frac{\Delta z}{\delta}. \tag{3.3}$$

In the LHC, measurements are typically taken at ±100Hz, corresponding to a momentum offset $\delta \approx \mp 0.7$.

Action The action in a given plane and BPM, located at position s is calculated from the amplitude $\mathcal{A}$ of the main peak in the frequency spectrum, which corresponds to the tune, along with the beta-function at that BPM derived from the model,

$$2J_{BPM} = \frac{\mathcal{A}^2_{BPM}}{\beta_{model,BPM}}. \tag{3.4}$$

This method of action computation is directly influenced by BPM calibration errors [55]. The overall action is then the average over n BPMs:

$$2J = \frac{1}{n}\sum_n \frac{\mathcal{A}^2_n}{\beta_{model,n}}. \tag{3.5}$$

Coupling Coupling can be calculated by comparing the amplitude of the tune in the frequency spectrum of a plane to the same tune in the other plane. The coupling RDTs f_{1001} and f_{1010} can be reconstructed with these amplitudes [56, 57],

$$\begin{aligned} |f_{1001}| &= \frac{1}{2}\sqrt{\frac{H(0,1)V(1,0)}{V(0,1)H(1,0)}}, \\ |f_{1010}| &= \frac{1}{2}\sqrt{\frac{H(0,-1)V(0,-1)}{V(0,1)H(1,0)}}, \end{aligned} \tag{3.6}$$

where H(1, 0) is the amplitude of Q_x in the horizontal spectrum while H(0, 1) corresponds to Q_y in the same spectrum. The phases of these RDTs is given by,

$$\begin{aligned} q_{1001} &= \phi_{V(1,0)} - \phi_{H(1,0)} + \frac{\pi}{2}, \\ q_{1010} &= \phi_{H(0,-1)} - \phi_{V(0,1)} + \frac{\pi}{2}. \end{aligned} \tag{3.7}$$

The final expression of the coupling RDTs is then,

$$
\begin{aligned}
f_{1001} &= |f_{1001}| e^{i \cdot q_{1001}}, \\
f_{1010} &= |f_{1010}| e^{i \cdot q_{1010}}.
\end{aligned}
\tag{3.8}
$$

Amplitude Detuning Amplitude detuning measurements in the LHC are usually taken with varying AC-Dipole kick amplitudes. A linear function is then fitted on the natural tunes Q_x and Q_y versus the action of either planes $2J_x$ or $2J_y$.

Resonance Driving Terms Resonance Driving Terms are measured in the LHC with varying AC-Dipole kick amplitudes. The amplitude of the resonance line of interest in the frequency spectrum can then be fitted to the corresponding action dependence of the RDT, as detailed in Section 2.7.2 and C. As a reminder, the amplitude of the RDT will be given by,

3

$$
\begin{aligned}
|f_{jklm}| &= \frac{|H_{f_{jklm}}|}{2j(2I_x)^{\frac{j+k-1}{2}}(2I_y)^{\frac{l+m}{2}}} \\
|f_{jklm}| &= \frac{|V_{f_{jklm}}|}{2l(2I_x)^{\frac{j+k}{2}}(2I_y)^{\frac{l+m-1}{2}}}.
\end{aligned}
$$

The phase of the RDT can then be reconstructed via the momentum and phase advances. In practice, *forced resonance driving terms* are actually measured, as the oscillations are driven by the AC-Dipole. Simulations are thus always made via tracking with an AC-Dipole to match. Studies linking *forced* RDTs to *free* RDTs is though ongoing to better understand the machine without excitation [58].

Lifetime The beam lifetime is a measure of how long the beam can remain circulating without significant losses of particles. It is typically expressed in hours and is related to the rate at which particles are lost from the beam. The beam intensity is measured via the BCTs. The lifetime τ relates then the number N of particles at a time t to its rate of change,

$$
\tau = N(t) \cdot \frac{\mathrm{d}N}{\mathrm{d}t}^{-1}.
\tag{3.9}
$$

Additionally, Beam Loss Monitors (BLMs) provide local information about beam quality by detecting and localizing particle losses. These losses can as well be integrated to give a lifetime estimate. At injection energy in the LHC, the beam lifetime with a pilot bunch is typically around 3 hours. Sudden particle losses can significantly reduce the measured lifetime, even if the remaining beam stabilizes and does not lose particles as rapidly. This introduces challenges in accurately measuring the lifetime, as the signal needs to stabilize and saturate after any trim to ensure reliable data.

3.2.3. Chromaticity

Contrary to the previously seen observables, chromaticity measurements are performed by varying the RF frequency to induce a change of momentum offset δ, while measuring the tune. The momentum offset δ being related to the RF frequency, the Lorentz factor γ and the momentum compaction factor α_c [31]:

$$\delta = -\left(\frac{1}{\gamma^{-2} + \alpha_c}\right) \cdot \frac{\Delta f_{\mathrm{RF}}}{f_{\mathrm{RF,nominal}}} \tag{3.10}$$

In the LHC, the Lorentz factor γ^{-2} is here negligible, as the energy is large even at injection. At 450GeV, $\gamma^{-2} \approx 10^{-6}$, which is two orders of magnitude smaller than α_c.

During operation, where the linear chromaticity often needs to be measured, a sinusoid function is applied on the RF frequency. This induces a short range of momentum offset, but enough to measure the first order of the chromaticity function. For non-linear measurements, a larger range is required. In order to do so, a new procedure has been developed. Dense frequency scans with steps of 20Hz every 30 seconds are usually taken to compromise between number of data points, precision of the tune estimate, and duration of the measurement. Once beam losses, registered by the BLMs are deemed too high, the frequency is reverted back to its nominal value in larger steps. Attaining the limits of the BLMs ensures a large momentum-offset range. The same procedure is then re-applied in the negative. Figure 3.6 shows a typical RF scan performed to measure chromaticity in the LHC.

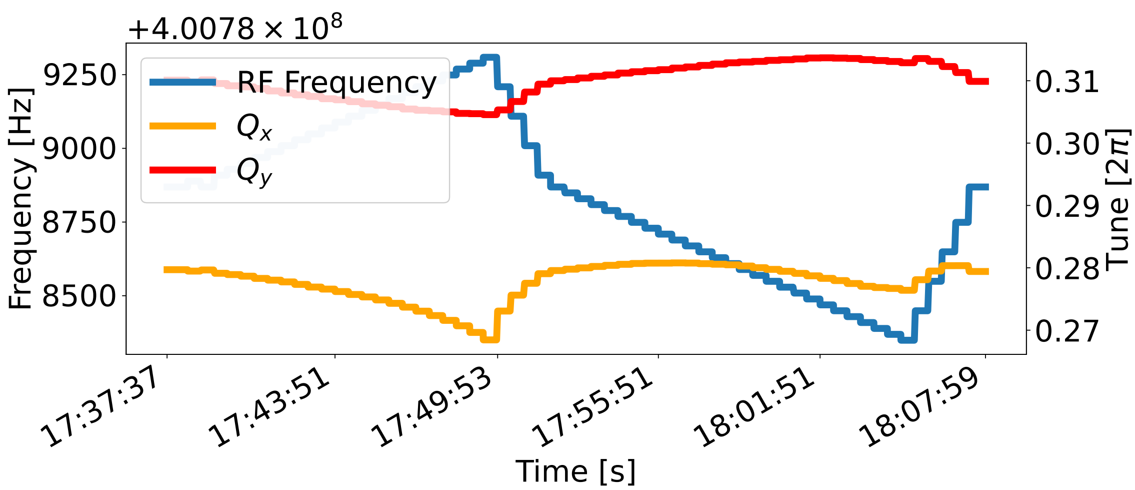

Figure 3.6.: Observation of the tune dependence on momentum offset, created by a shift of RF frequency.

Once the tunes have been acquired and the momentum offset computed via Eq. (3.10), the chromaticity function (see Eq. (2.65)) can be used to fit the measured data and retrieve each order.

As part of the work for this thesis, a new tool, was developed. in order to ease and improve the analysis of chromaticity measurements. The Non-Linear Chromaticity GUI [46] showcases new analysis techniques using the raw signal from the BBQ system along with custom signal cleaning that are detailed later on in Chapter 6. Fits to very high chromaticity orders are also now possible along with their computed corrections and that of resonance driving terms via a combined response matrix approach. Automatic data extraction from the CERN data servers (Timber, NXCALS) is also included.

3.3. Correction Principles

Several ways exist to correct the previous observables. Two common ways to do so are here detailed.

3.3.1. Response Matrix

A response matrix is a linear equation system that describes the change of an observable for a set of individual multipole strengths. By taking the pseudo-inverse of this matrix and multiplying it to the measured observables, a set of corrector strengths if obtained that can replicate the measured value. Taking the opposite sign then gives a correction. This technique is used to correct, amongst others, β-beating, chromaticity as well as Resonance Driving Terms for the first time in the LHC with this thesis. In situations where measurements are taken at each BPM for a particular observable, the corresponding response matrix ends up containing over 500 values per corrector, for a single beam.

Individual MAD-X simulations are run with a single specific circuit powered at a time. The resulting parameter values (e.g. β-beating) are then compared to those obtained from a simulation without any powering, allowing to determine the impact of each circuit on that observable.

A response matrix is thus created following Eq. (3.11), for a matrix of observables O, a reference matrix of observables without any corrector O_R and a fixed multipole strength k. Given measured data M, the set of correctors needed to compensate the values can be obtained by taking the pseudo-inverse of the matrix in Eq. (3.12).

$$R = (O - O_R) \cdot \frac{1}{k} \tag{3.11}$$

$$\begin{bmatrix} k_1 \\ \vdots \\ k_n \end{bmatrix} = -(R^+ \cdot M) \tag{3.12}$$

Response matrices are very versatile and can combine several observables to be corrected by the same multipoles. One example, detailed later in this thesis, is the third order chromaticity and the resonance driving term f_{1004}, both contributed to by decapoles.

Example

In this example, simulations are run with MAD-X PTC to correct the third chromaticity in the LHC. Q''' is taken from `ptc_normal` for each beam and axis, with `MCDs`, decapole correctors, powered with a fixed strength one at a time. A scaling factor is applied to get the change of chromaticity for one unit of K_5. 8 correctors are used, which strengths are denoted k_1 through k_8. Transposes are only used to make the equations easier to display.
The values in Table 3.1 are corrected via Eq. (3.14) after having built the response matrix in Eq. (3.13).

Observable	Value
Q_x'''	-666111
Q_y'''	121557

Table 3.1.: Example chromaticity values to correct via a response matrix

$$R = \left(\begin{matrix}\text{Individual}\\ \text{simulations}\end{matrix} \left\{ \begin{array}{c} \begin{array}{cc} \overbrace{}^{Q_x'''} & \overbrace{}^{Q_y'''} \end{array} \\ \begin{bmatrix} -155899 & 122004 \\ -254584 & 138368 \\ -122715 & 106709 \\ -218597 & 110686 \\ -134140 & 106463 \\ -245791 & 118951 \\ -147035 & 116544 \\ -219537 & 112317 \end{bmatrix}^T \end{array} \right. - \overbrace{\begin{bmatrix} 5135 \\ 8470 \end{bmatrix}}^{\text{Reference}} \left. \begin{matrix} Q_x''' \\ Q_y''' \end{matrix} \right\} \right) \cdot \underbrace{\frac{1}{-1000}}_{\text{Corrector strength}} \tag{3.13}$$

$$
\left.\begin{matrix} k_1 \\ k_2 \\ k_3 \\ k_4 \\ k_5 \\ k_6 \\ k_7 \\ k_8 \end{matrix}\right\}
\begin{pmatrix} -1235 \\ 1032 \\ -1394 \\ 1449 \\ -1043 \\ 1864 \\ -1187 \\ 1369 \end{pmatrix}
= -R^{+} \cdot \left.\begin{pmatrix} -666111 \\ 121557 \end{pmatrix}\right\} \begin{matrix}\text{Measured} \\ \text{values}\end{matrix}
\tag{3.14}
$$

3.3.2. Global Trims for Chromaticity

As per the placement of the octupolar and decapolar correctors in the LHC layout [59], β-functions at their location are slightly different from arc to arc. This slight imbalance leads theoretically to the possibility of correcting the horizontal and vertical axes of the second and third order chromaticity independently, via a response matrix approach. In practice, the required strength to do so would exceed those of the design of the correctors.

Another way to correct the chromaticity is via a global uniform trim, where every available corrector is powered to the same strength. Simulations are run with `ptc_normal` via MADX-PTC to obtain the response in chromaticity for a given strength. Chromaticity being linear with multipole strength, an affine function can be determined for each axis. Figure 3.7 shows a simulation with several MCD strengths, highlighting this linear relation between Q''' and K_5, while Equation (3.15) shows an example of such functions computed at injection energy for the 2022 optics.

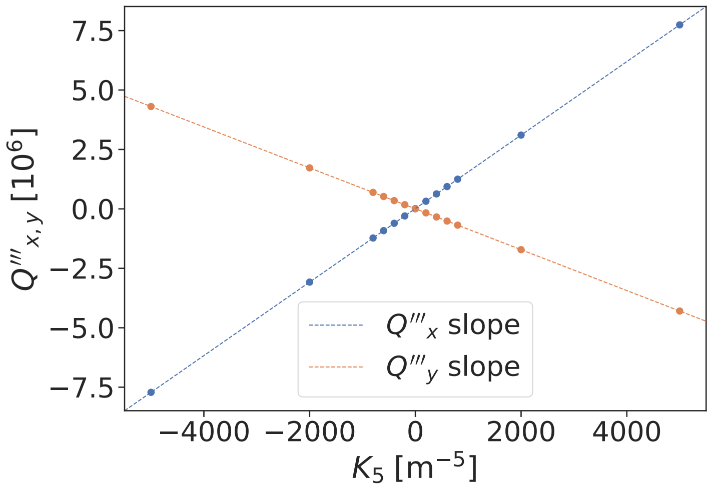

Figure 3.7.: Linear relation between the third order chromaticity and decapole corrector strengths, simulated with MADX-PTC.

$$\begin{aligned} Q_x''' &= 1533 \cdot \Delta K_5 + 6680 \\ Q_y''' &= -860 \cdot \Delta K_5 + 5647 \end{aligned} \tag{3.15}$$

Only the linear part is relevant, as the offset is generated by other multipoles and field errors. It is thus constant for a configuration where only the relevant spool pieces are used.

Corrections involve minimizing both axes, typically where Q_x''' meets Q_y''':

$$\Delta K_5 = -\frac{(Q_x''' - Q_y''')}{\mathrm{slope}_{Q_x'''} - \mathrm{slope}_{Q_y'''}} \tag{3.16}$$

4

Skew Octupolar Fields

4.1. Introduction

The skew octupolar fields in the LHC have previously been identified as significant contributors to limits in forced dynamic aperture, being the dynamic aperture when kicking the beam with the AC-Dipole [58]. Skew octupolar correctors are positioned around the ATLAS and CMS detectors, in Interaction Regions 1 and 5. Those correctors are *common aperture* magnets ; both beams are affected by the created magnetic fields. Unfortunately, one of these four correctors, located to the left of ATLAS, is not functioning. As a result, although corrections can be calculated, they will not effectively minimize the skew octupolar RDTs of interest, $f_{1012,y}$ and $f_{1210,x}$. The associated resonances and frequency lines of these RDTs are shown in Table 4.1.

RDT	Resonance	H-line	V-line
f_{1012}	$1Q_x - 1Q_y$	$1Q_y$	$-1Q_x + 2Q_y$
f_{1210}	$-1Q_x + 1Q_y$	$2Q_x - 1Q_y$	$1Q_x$

Table 4.1.: Skew octupolar RDTs of interest, their associated resonances and the frequency spectrum lines they contribute to.

First corrections of skew octupolar RDTs were performed in 2018 at top energy [58]. A different approach for the same corrections is presented in this chapter. Measurements were also performed at injection energy with the prospect of corrections. However, it was observed that Landau octupoles were strongly contributing to the RDTs of interest.

4.2. Corrections at Top Energy

The very first skew octupolar RDT corrections in the LHC were made in 2018 during Run 2 [58]. These corrections were computed by matching the RDT level of the measurements in simulation and then inverting the strengths. This is possible and remains viable as only three correctors are used and values can be manually adjusted. In this section, a different approach is taken, based on response matrices. This type of correction is explained in details in Section 3.3.1. The real and imaginary responses of the RDTs for each corrector at an arbitrary strength are simulated through tracking. These responses are collected into a matrix, allowing the determination of the required strengths to match the RDT level observed in the measurements. Inverting these values result in a correction.

4.2.1. Correctors

To create a response matrix, simulations were conducted with the tunes and AC-Dipole deltas set to those used for measurements. The natural tunes are $Q_x = 0.285$ and $Q_y = 0.292$ while the driven tunes are $\Delta Q_x = -0.008$ and $\Delta Q_y = 0.01$. Each corrector is then powered individually for each tracking simulation. For this type of simulation, field errors are not necessary, as only the RDT shift caused by the corrector relative to the baseline is needed. Figure 4.1 shows the real part of the resulting RDTs from these simulations for Beam 1. Beam 2 shows a similar level of response for these correctors.

It can already be seen that the L5 and R5 correctors show a similar trend along the ring, with L5 showing a stronger response for the same strength, while the R1 corrector follows the opposite trend. A polar plot at a given BPM can illustrate that trend, and be used to get an intuition of the effect of the correctors to manually compute corrections. Figure 4.2 shows the orthogonality of the correctors for both beams and RDTs. L5 being stronger than R5 while having the same angle indicates that only one of them is needed for corrections.

4.2.2. Measurements and Corrections

Initial measurements of the machine at top energy ($\beta^* = 30$cm) without any skew octupolar correctors were done during an MD slot in 2022 to determine the level of the RDTs before being able to correct them. Those measurements were made at natural tunes of $Q_x = 0.285$ and $Q_y = 0.292$. The driven tunes were set to $\Delta Q_x = -0.008$ and $\Delta Q_y = 0.01$. This selection of tunes has proven to be appropriate for measuring skew octupolar RDTs. The Landau octupoles were powered off during the measurements.

The corrections were computed via the previously detailed response matrix and are shown in Table 4.2. These have then been applied during 2023's commissioning and later on kept for operation. The RDT levels of the bare machine and with these corrections are shown in Fig. 4.3. It can be observed that both RDT amplitudes are reduced, with the exception of $f_{1210,x}$ for Beam 2, which stays constant.

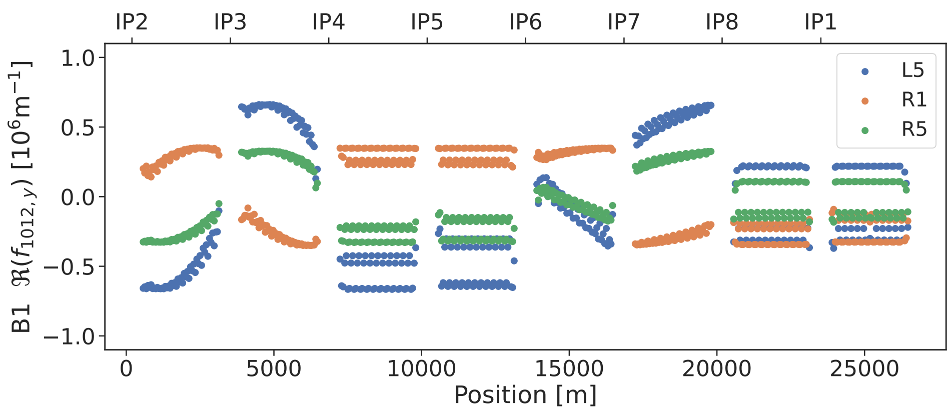

(a) $f_{1012,y}$

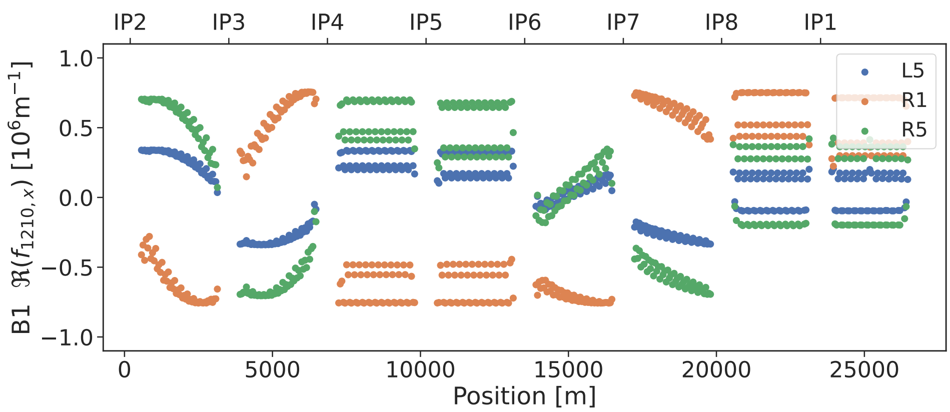

(b) $f_{1210,x}$

Figure 4.1.: Simulation of the RDT response of the skew octupolar correctors at top energy for Beam 1. Each corrector is powered at $J_4 = 1[\mathrm{m}^{-4}]$.

The reduction of RDT amplitude is comparable to those obtained in 2018, where the same RDT for Beam 2 did neither improve or worsen.

Corrector	Strength [m^{-4}]
MCOSX3.L1	—
MCOSX3.R1	−0.50
MCOSX3.L5	0.42
MCOSX3.R5	−0.01

Table 4.2.: Computed corrections for skew octupolar RDTs at top energy. The corrector L1 has been broken for several years and can not be used.

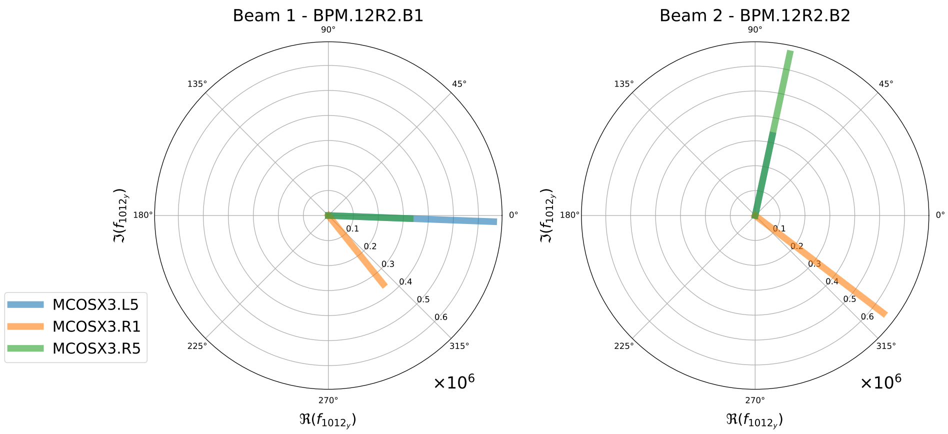

(a) $f_{1012,y}$

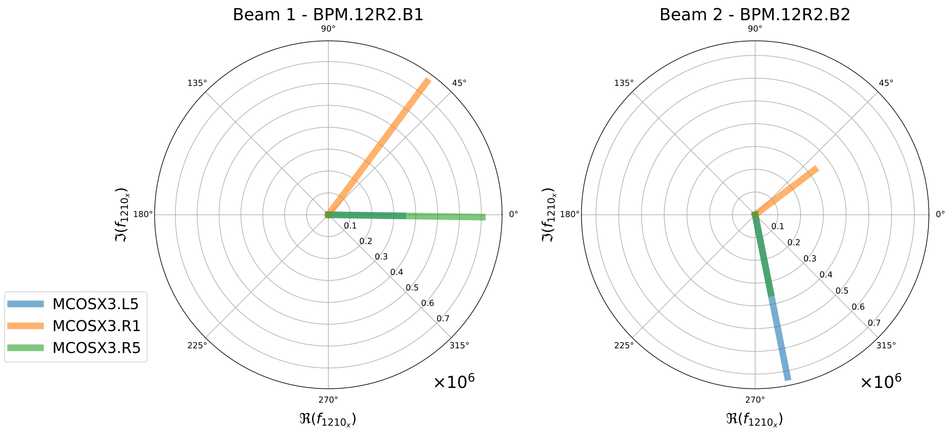

(b) $f_{1210,x}$

Figure 4.2.: Simulated RDTs response of the available skew octupolar correctors at top energy. Each corrector is powered at $J_4 = 1[\mathrm{m}^{-4}]$. The orthogonality of R1 and L5/R5 allows to independently control the real and imaginary parts.

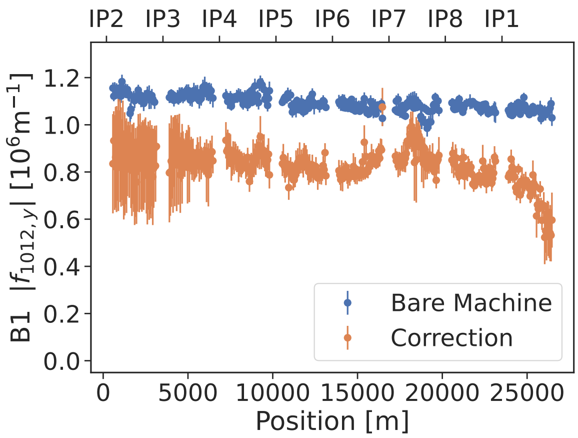

(a) $f_{1012,y}$ Beam 1

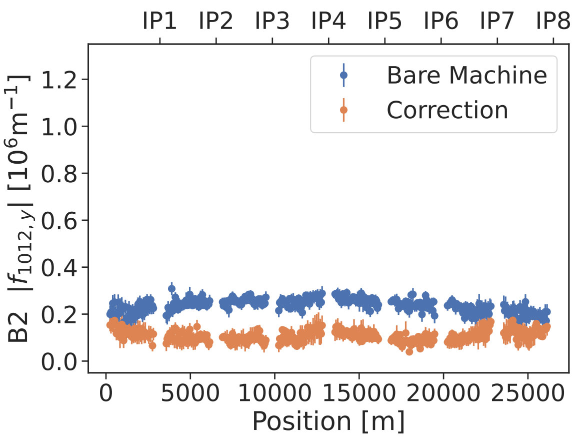

(b) $f_{1012,y}$ Beam 2

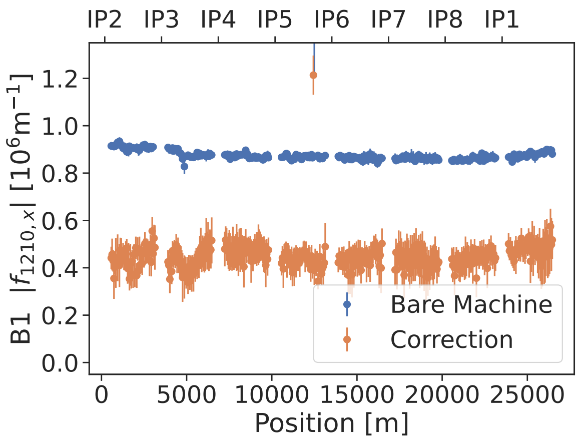

(c) $f_{1210,x}$ Beam 1

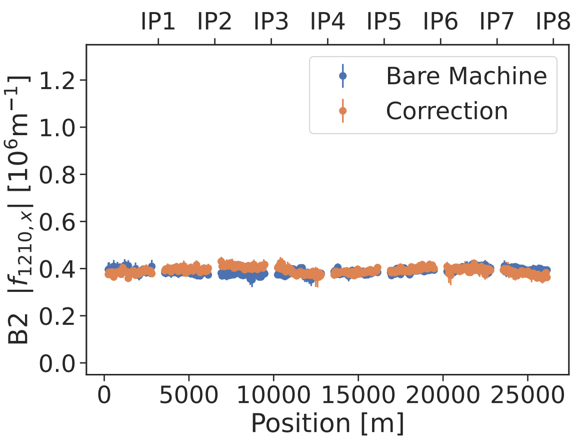

(d) $f_{1210,x}$ Beam 2

Figure 4.3.: Measured skew octupolar RDTs at top energy and $\beta^* = 30$cm before and after correction. A reduction if observed for all but one RDT in Beam 2.

4.3. Landau Octupoles Contribution

4.3.1. Introduction

During the 2023 commissioning, measurements were taken at injection energy with different strengths of Landau octupoles, where an unexpected shift in the skew octupolar RDTs was observed. Subsequent measurements were conducted to better understand and characterize this contribution of normal octupoles to skew octupolar fields. These new measurements were taken during an MD slot in September 2023 and focused on varying the strengths of the Landau octupoles to $-1K_4$, $\pm 2K_4$, $5K_4$. All measurements were taken at injection energy at tunes of $Q_x = 0.275$, $Q_y = 0.293$ and AC-Dipole deltas of $\Delta Q_x = -0.01$ and $\Delta Q_y = -0.011$. Although both beams were measured, this section focuses on Beam 1 to preliminarily investigate the matter. The following Fig. 4.4 illustrates the difference in amplitude of the RDT f_{1012} with these varying strengths. Figure 4.5 on the other hand shows the measured and simulated shift of the same RDT from $0K_4$ to $+2K_4$. It is evident that simulations including normal and skew octupolar field errors are not enough to explain the behaviour observed in the measurements.

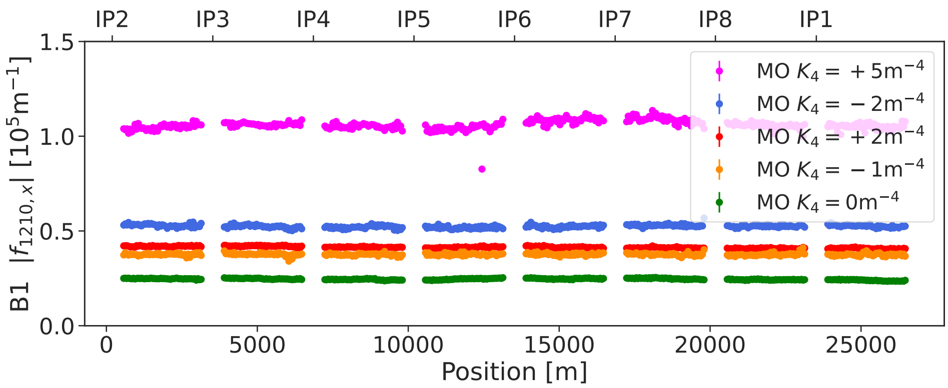

Figure 4.4.: Unexpected difference of skew octupolar RDT amplitudes with varying Landau octupoles strengths.

4.3.2. Misalignments

Magnet misalignments, more specifically roll errors, can generate skew magnetic fields instead of the expected normal ones. To determine if this could explain the behaviour observed in measurements, a tracking simulation was conducted with and without roll errors applied to the Landau octupoles. The resulting RDTs reveal an imperceptible difference, unable to account for the previously seen shifts. The real part of the RDT f_{1012} is shown in Fig. 4.6, with similar results seen in the other component and in f_{1210}.

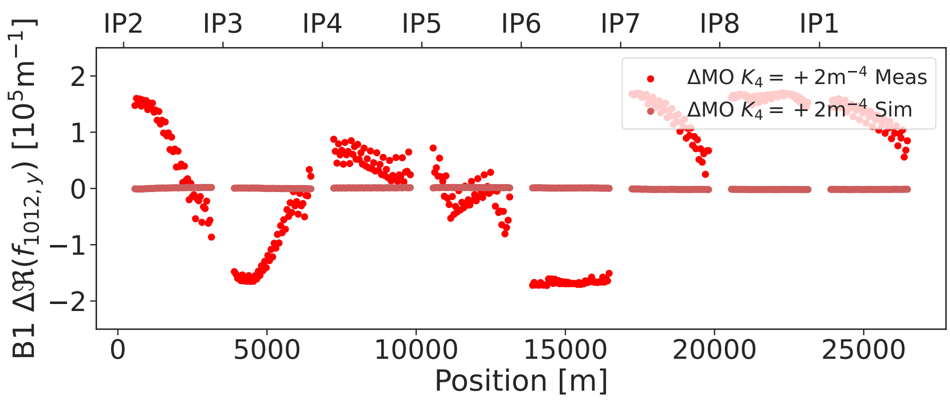

Figure 4.5.: Measured and simulated shift of skew octupolar RDT after increase of Landau octupoles strength from zero. It is apparent that the shift in measurement is not replicated by the simulation.

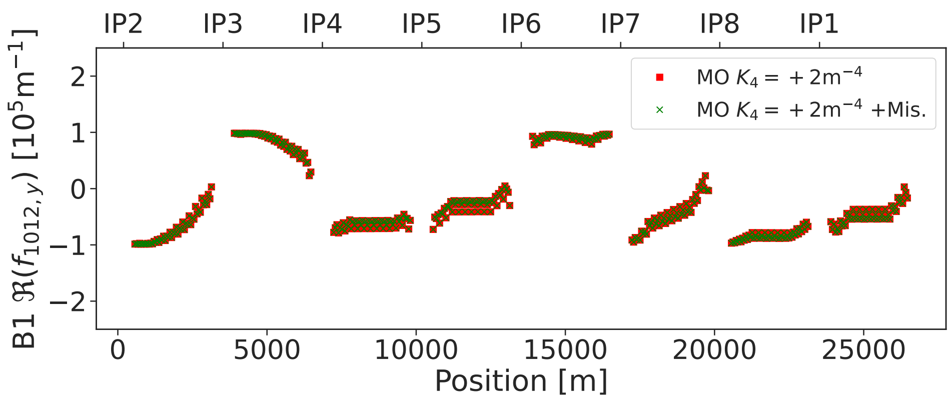

Figure 4.6.: Simulated skew octupolar RDT with normal and skew octupolar errors and Landau octupoles powered. One simulation includes further alignment errors on the Landau octupoles. No significant difference is observed between the two.

4.3.3. Coupling

As misalignments could not explain the discrepancy, simulations were first run with varying values of coupling at a fixed octupolar strength, allowing to gage the impact of coupling only. Appendix A.2.4 details how coupling, in the form of a skew quadrupole, combined with a normal octupole can generate skew quadrupolar-like fields. The resulting RDT f_{1012} is shown in Fig. 4.7, a similar trend is observed for f_{1210}. The presented C^- values are commonly seen in operation and well below that of the tolerances of the design of the LHC [10]. As coupling increases, the skew octupolar RDTs are expected to be significantly altered.

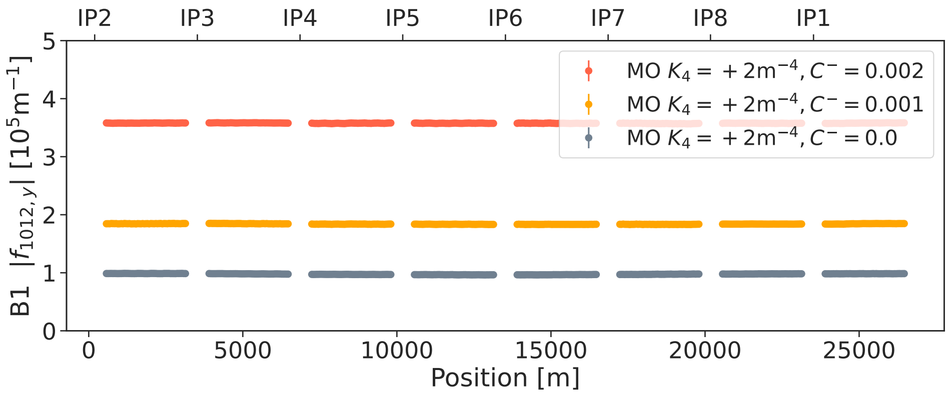

Figure 4.7.: Simulated skew octupolar RDT with fixed Landau octupole strength but varying coupling. Selected coupling values are often seen in operation.

Responses with Coupling

		Rel. Diff. [%]	
K_4 [m^{-4}]	RDT	Real	Imag.
+5	f_{1210}	6	6
	f_{1012}	12	11
+2	f_{1210}	32	34
	f_{1012}	36	36
-1	f_{1210}	26	25
	f_{1012}	21	20
-2	f_{1210}	19	17
	f_{1012}	21	20

Table 4.3.: Relative difference between measured and simulated RDT shift induced by the Landau octupoles in presence of coupling. Real parts are illustrated in Fig. 4.8.

After having demonstrated that coupling could significantly contribute to the creation of skew octupolar fields with normal octupoles, additional simulations were performed matching the measured coupling for each set of measurements. The shift in real part of the RDTs f_{1012} and f_{1210} is shown in Fig. 4.8, with a similar pattern observed for the imaginary part. The relative RMS deviation between simulations and measurements is given for each set of strengths and RDTs in Table 4.3.

It can be observed that simulations and measurements for positive strengths ($K_4 = 2$ and $K_4 = 5$) are now in good agreement. This suggests that the primary contribution to the skew octupolar RDTs can be attributed to the Landau octupoles and coupling. The relative deviation between measurement and simulation can be explained by the sensitivity to the coupling. A difference of 10^{-4} units is enough to be noticeable, making accurate reproduction of skew octupolar RDTs not trivial. It is important to note that measurements of f_{1012} with *negative* strength show a response opposite to what is predicted by simulations while f_{1210} agrees well. This behaviour is not yet understood and requires further investigation.

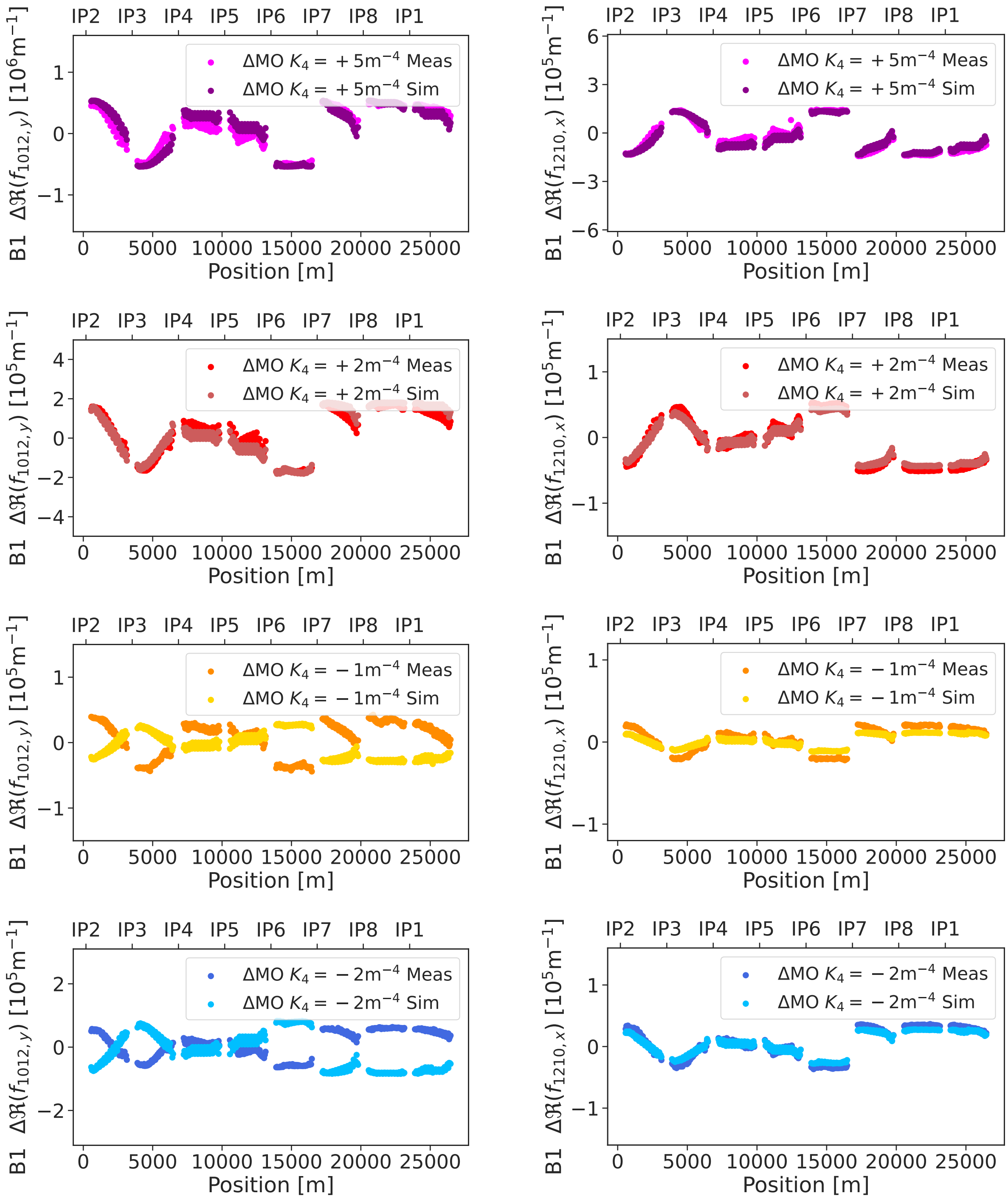

Figure 4.8.: Measured and simulated real part shift of skew octupolar RDTs induced by Landau octupoles in presence of coupling at injection energy. Left column shows f_{1012} while right shows f_{1210}. The vertical scale is adjusted for each plot to highlight the agreement of the simulations.

4.4. Summary

This chapter investigates the origins of skew octupolar fields in the LHC and explores methods to mitigate their effects. Previous studies have shown that these fields significantly contribute to limitations in dynamic aperture, particularly when the beam is kicked with the AC-Dipole. The skew octupolar correctors, located around the ATLAS and CMS detectors, are crucial for managing these fields.

A response matrix method was developed to correct skew octupolar RDTs at top energy using the available corrector magnets. While effective, the absence of one corrector limits the achievable correction strength. As a result, the RDTs f_{1012} and f_{1210} are either successfully corrected or maintained at a constant level.

Additionally, this chapter addresses the unexpected influence of Landau octupoles on skew octupolar RDTs at injection energy. Simulations reveal that misalignments of the Landau octupoles, specifically roll errors, do not a have a significant impact. Instead, coupling was found to be a crucial factor. While further investigation is required to fully understand the underlying mechanisms, initial findings suggest that accurate modeling of coupling is essential for predicting the behavior of skew octupolar RDTs in the presence of Landau octupoles. During regular operation, where the Landau octupoles are powered at $K_4 = 18$, very large skew octupolar RDTs are expected to be generated.

The results presented provide valuable insights into the complex interplay of magnetic fields in the LHC and highlight the importance of accurate modeling for corrections.

5 Decapolar Fields

5.1. Introduction

5.1.1. Motivation

Beam-based measurements have been carried in the LHC since Run 1 to better understand the decapolar fields. Those have been carried out via chromaticity measurements [60–62]. The third order of the non-linear chromaticity, Q''', generated for the most part by decapoles, has shown a consistent discrepancy at injection energy between its expected value from simulations and that observed. Figure 5.1 highlights this discrepancy.

The FiDeL model, based on magnetic measurements, is used during operation to correct various multipole errors, including octupolar and decapolar. The operational corrections being based on this magnetic model and simulations, the residual Q''' value is expected to be small, which is however not the case. Chromaticity measurements have thus been repeated during LHC's Run 3 and corrections made routine, aimed at correcting the observed discrepancy.

The study of non-linear chromaticity has proven valuable in quantifying decapolar fields, yet it does not permit alone to understand the exact origins of the observed discrepancy. In an effort to gain deeper insights, additional measurements were performed focusing on novel observables that had not been previously explored. *Bare chromaticity* involves measuring chromaticity with the octupolar an decapolar correctors deactivated ; this approach aims to isolate the machine effects from those of the correctors. *Chromatic amplitude detuning*, evaluates how the tune varies with both the beam's action and the momentum offset ; this methods has the benefit of having a different expression that of the chromaticity.

Complementing those measurements, studies of decapolar Resonance Driving Terms have been undertaken for the first time in the LHC. Contributing to resonances close to the working, those RDTs also have benefited from corrections.

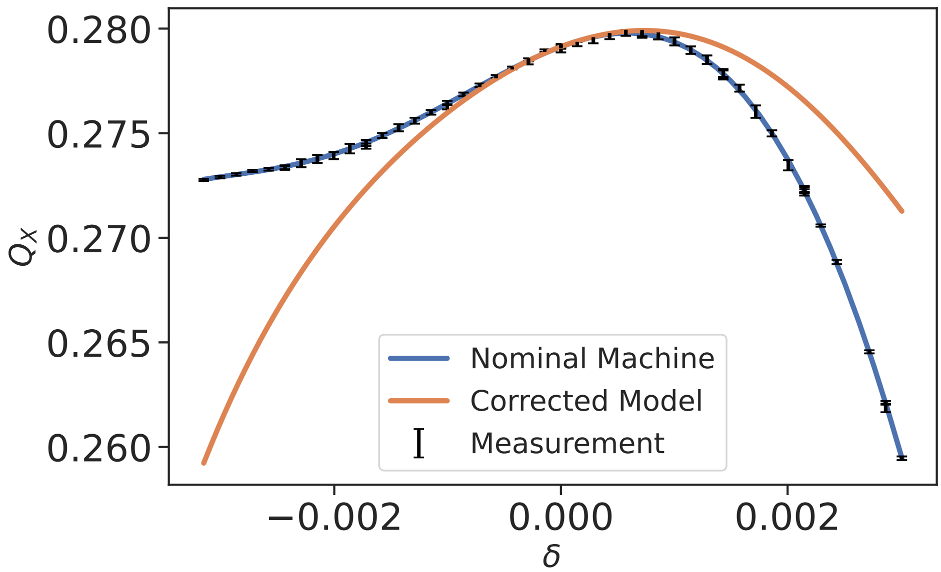

Figure 5.1.: Measured and simulated chromaticity with application of the nominal decapolar corrections from FiDeL. It can be seen that although the corrections should diminish Q''', it is not well corrected in practice.

5.1.2. Decapolar Correctors

As seen in Fig. 2.4, the LHC is equipped with decapoles. Those magnets are part of the LHC's design report, aiming at correcting the field errors of the main dipoles. Those correctors, denominated *MCD*, are specific to each beam and are placed after every second dipole, totaling 1232 in number [63]. MCDs are nested with octupolar correctors, *MCO*. The pair of those correctors of often referred to as *MCDO*. It is not possible to individually power each corrector. Rather, a circuit consists of a whole arc. There are in total 16 circuits to control the correctors of both beams and 8 arcs. Figure 5.2 shows a picture taken of decapoles on a test bench.

The important characteristics of the magnetic fields of correctors are their main field transfer function (or *response*), the field quality and possible crosstalk, as MCOs and MCDs are nested [63]. In order to determine the aforementioned discrepancy, the decapole correctors themselves need to be studied, to rule any possible unwanted effects.

Strengths at Injection At injection energy, the decapoles are powered to a static strength. New optics introduced throughout the years often have for effect to vary slightly the β-function along the ring, having thus an impact on the chromaticity, as seen in Eq. (2.73). New corrections are then computed via FiDeL to account for it. Although those corrections vary throughout the years, the

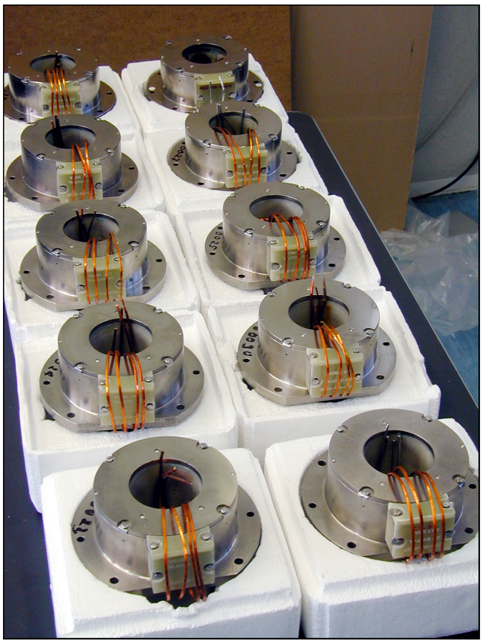

Figure 5.2.: Decapoles on a test bench, being inspected after manufacturing [64].

Circuit	$K_5\,[\mathrm{m}^{-5}]$
Beam 1	
RCD.A12B1	−4582
RCD.A23B1	−5106
RCD.A34B1	−4855
RCD.A45B1	−4577
RCD.A56B1	−4125
RCD.A67B1	−5166
RCD.A78B1	−6827
RCD.A81B1	−5500
Beam 2	
RCD.A12B2	−4490
RCD.A23B2	−5155
RCD.A34B2	−4825
RCD.A45B2	−4619
RCD.A56B2	−4064
RCD.A67B2	−5066
RCD.A78B2	−6866
RCD.A81B2	−5446

Table 5.1.: Strength of decapolar correctors at injection energy for FiDeL corrections.

5

shift is in practice fairly negligible. Table 5.10, a bit further in this chapter, shows the strength of the correctors and the related circuits at injection energy for the optics deployed in 2024.

5.2. Response of correctors

The full third term of the chromaticity function is highlighted in Eq. (5.1). Details on chromaticity are given in Section 2.6.1.

$$Q(\delta) = Q_0 + Q'\delta + \frac{1}{2!}Q''\delta^2 + \boxed{\frac{1}{3!}Q'''\delta^3} + O(\delta^4). \tag{5.1}$$

This third order, mainly contributed to by decapoles, is related to the β-function, the dispersion and the strength of the multipole:

$$\begin{aligned} \Delta Q_x''' &= \frac{1}{4\pi}K_5 L\beta_x D_x^3 \\ \Delta Q_y''' &= -\frac{1}{4\pi}K_5 L\beta_x D_x^3. \end{aligned} \tag{5.2}$$

In order to assess the accuracy of corrections, measurements have to be done to gauge the response of the decapolar correctors, *MCDs*. During Run 3's commissioning, measurements and corrections of Q'' and Q''' have been made routine. Those corrections give the opportunity to study the response of the correctors. Figure 5.3 shows the chromaticity function measured during Run 3's commissioning in 2022 with the nominal corrections via FiDeL and beam-based corrections computed analytically based on top of FiDeL.

The nominal and corrected Q''' values are shown in Table 5.2. The shift in Q''' is shown in Table 5.3 for each beam and axis, and is showing a good agreement between the measurements and simulations. The slight imbalance can be attributed to higher order effects of the octupole correctors, whose correction was implemented after that of Q'''.

This agreement between the simulations and the measurements indicates that our decapole correctors function as intended.

5.3. Bare Chromaticity

Previous studies [62] have demonstrated that octupole and decapole correctors were contributing to an observed octupolar discrepancy in the machine via hysteresis and feed-down. To evaluate the possible effect of decapole correctors on the third order chromaticity Q''', a measurement was taken with these elements turned off.

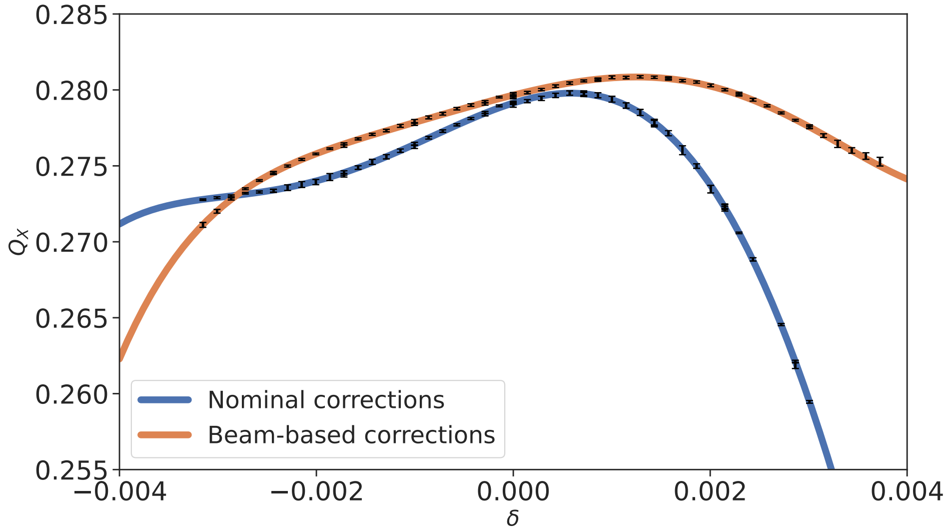

Figure 5.3.: Chromaticity of the horizontal plane of Beam 1 during Run 3's commissioning, with nominal corrections based on the magnetic model and beam-based corrections aimed at correcting Q'' and Q'''.

	Q''' [10^6]	
Plane	Nominal	Beam-Based
Beam 1		
X	-3.36 ± 0.04	-1.02 ± 0.03
Y	1.62 ± 0.05	0.12 ± 0.02
Beam 2		
X	-2.72 ± 0.08	-0.64 ± 0.03
Y	1.54 ± 0.06	0.14 ± 0.03

Table 5.2.: Third order chromaticity obtained during Run 3 commissioning, with nominal and beam-based corrections aimed at correcting Q'' and Q'''.

Simulations have been run with MAD-X and PTC including fields errors from normal sextupole to decahexapole. The expected Q''' values are presented in Table 5.4 and compared to the measured ones along with the ratio between the two.

A consistent ratio is observed for every beam and plane between the measurement and the model. This result, supplemented by the correct response of the correctors, indicates that the decapolar correctors do no generate unwanted fields. Those correctors can thus be discarded as the potential source of discrepancy.

Plane	$\Delta Q'''$ [10^6] Measurement	Simulation
Beam 1		
X	2.3 ± 0.1	2.5
Y	-1.5 ± 0.1	-1.4
Beam 2		
X	2.1 ± 0.1	2.5
Y	-1.4 ± 0.1	-1.4

Table 5.3.: Response of the third order chromaticity upon application of corrections on top of the nominal ones used in operation for both measurements and simulations.

Quantity	Measured [10^6]	Simulated [10^6]	Ratio
Beam 1			
Q_x'''	2.95 ± 0.04	6.94 ± 0.02	0.43 ± 0.01
Q_y'''	−1.82 ± 0.04	−4.29 ± 0.01	0.42 ± 0.01
Beam 2			
Q_x'''	3.06 ± 0.07	7.03 ± 0.02	0.44 ± 0.01
Q_y'''	−1.72 ± 0.02	−4.27 ± 0.01	0.42 ± 0.01

Table 5.4.: Measured and simulated third order chromaticity with octupole and decapole correctors turned off. The simulations include field errors from sextupoles to decahexapole (normal sextupole to decahexapole).

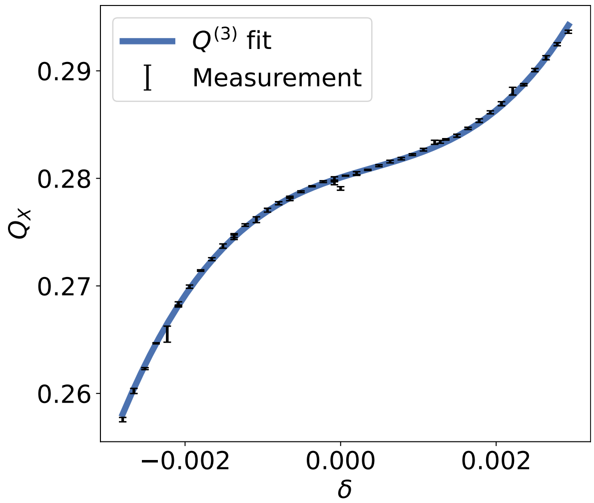

(a) Q_x Beam 1

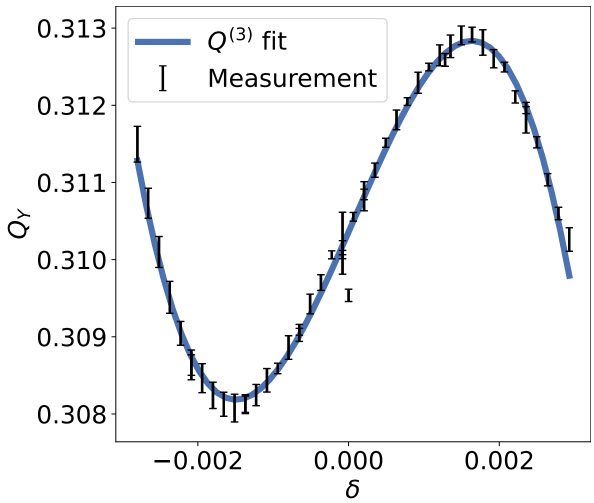

(b) Q_y Beam 1

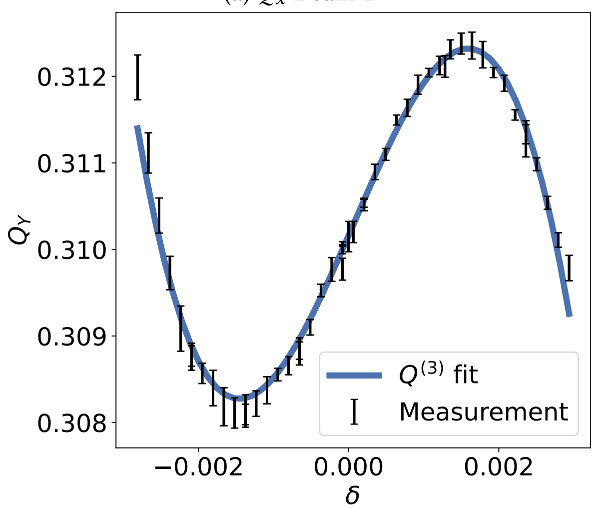

(c) Q_x Beam 2

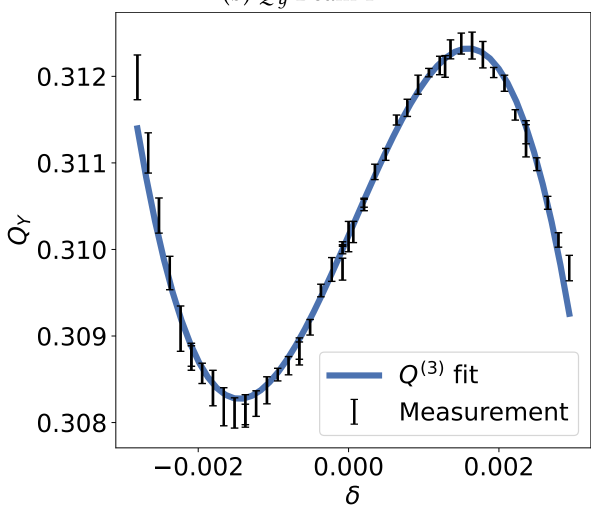

(d) Q_y Beam 2

Figure 5.4.: Fit of the chromaticity function for the chromaticity measurement performed with octupole and decapole correctors powered off. The fit includes all orders up to third.

5

5.4. Chromatic Amplitude Detuning

The Chromatic Amplitude Detuning is the tune shift dependant on both the actions and the momentum offset, whose decapole contributed terms are described via a Taylor expansion in Eq. (5.3). More information and derivations can be found in Section 2.6.3 and Appendix B.

$$\Delta Q(J_x, J_y, \delta) = \frac{\partial^2 Q}{\partial J_x \partial \delta} \cdot J_x \delta + \frac{\partial^2 Q}{\partial J_y \partial \delta} \cdot J_y \delta + \frac{1}{3!} \frac{\partial^3 Q}{\partial \delta^3} \cdot \delta^3. \tag{5.3}$$

The last term is more commonly referred to as the third order chromaticity, Q'''. Each of those terms depend on the β-functions, the horizontal dispersion D and the normalized decapole field gradient K_5 for a single source of length L,

$$\begin{aligned}
\frac{\partial^2 Q_x}{\partial J_x \partial \delta} &= \frac{1}{16\pi} K_5 L \beta_x^2 D, & \frac{\partial^2 Q_x}{\partial J_y \partial \delta} &= -\frac{1}{8\pi} K_5 L \beta_x \beta_y D, \\
\frac{\partial^3 Q_x}{\partial \delta^3} &= \frac{1}{4\pi} K_5 L \beta_x D^3, & \frac{\partial^2 Q_y}{\partial J_x \partial \delta} &= -\frac{1}{8\pi} K_5 L \beta_x \beta_y D, \\
\frac{\partial^2 Q_y}{\partial J_y \partial \delta} &= \frac{1}{16\pi} K_5 L \beta_y^2 D, & \frac{\partial^3 Q_y}{\partial \delta^3} &= -\frac{1}{4\pi} K_5 L \beta_y D^3.
\end{aligned} \tag{5.4}$$

The action dependant terms can be measured by exciting the beam with an AC-dipole with increasing strengths at different momentum-offsets.

Such a measurement was taken with octupole and decapole correctors turned off to measure the bare machine. Some data could not be collected due to machine availability issues, restricting the measurement to low intensity kicks. Nevertheless, the terms $\frac{\partial^2 Q_x}{\partial J_y \partial \delta}$ and $\frac{\partial^2 Q_y}{\partial J_y \partial \delta}$ for beam 2 were measured for the first time in the LHC. The momentum-offsets measured at were -0.001 and 0.001, respectively roughly equal to a trim of +140Hz and −140Hz of the RF.

Figure 5.5a and Fig. 5.5b show a fit of those terms to measured $Q_{x,y}$ vs J_y at two different momentum offsets. Expected shifts from MADX-PTC simulations, that include field errors ranging from sextupoles to decahexapoles (b_3 to b_8 and a_4 to a_8) are shown as a comparison.

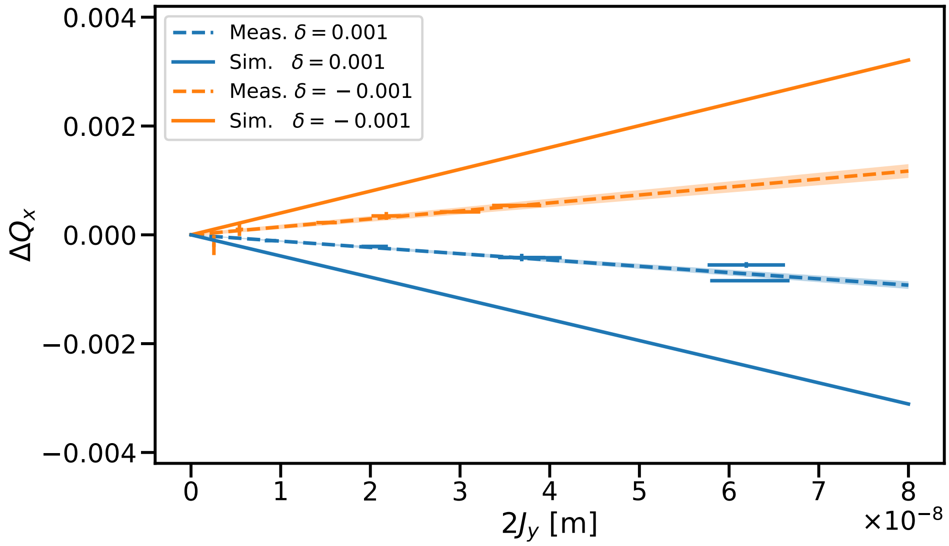

(a) Horizontal tune shift depending on the vertical action: $\frac{\partial^2 Q_x}{\partial J_y \partial \delta}$.

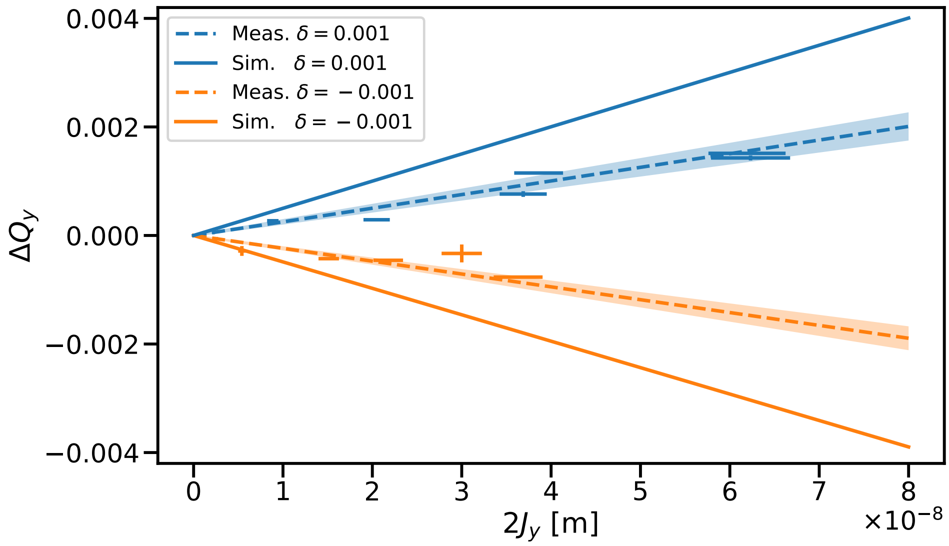

(b) Vertical tune shift depending on the vertical action: $\frac{\partial^2 Q_y}{\partial J_y \partial \delta}$.

Figure 5.5.: Measured and simulated tune shift due to a change of action via an AC-Dipole at two different momentum offsets. Each fit corresponds to a chromatic amplitude detuning term evaluated at a certain δ.

5

Type	$\frac{\partial^2 Q_x}{\partial J_y \partial \delta}$ [10^4m^{-1}]	$\frac{\partial^2 Q_y}{\partial J_y \partial \delta}$ [10^4m^{-1}]
$\delta = +0.001$		
Meas.	-1.16 ± 0.08	1.26 ± 0.15
Sim.	-3.82 ± 0.01	2.47 ± 0.01
Ratio	0.30 ± 0.02	0.51 ± 0.06
$\delta = -0.001$		
Meas.	1.47 ± 0.12	-1.18 ± 0.13
Sim.	3.92 ± 0.01	-2.41 ± 0.01
Ratio	0.38 ± 0.03	0.49 ± 0.05

Table 5.5.: Comparison of the measured and simulated terms $\frac{\partial^2 Q_x}{\partial J_y \delta}$ and $\frac{\partial^2 Q_y}{\partial J_y \partial \delta}$ via PTC, at two discrete momentum offsets. Simulations include errors from normal sextupole to decahexapole and from skew octupole to decahexapole.

A consistent difference between simulation and measurement is observed, which values and ratios of measurement to model can be found in Table 5.5. The observed ratios of measurement to model for the chromatic amplitude detuning show slight discrepancies compared to the bare chromaticity ones. These discrepancies could be due to the low intensity kicks, which don't allow for a better fit. However, the similarity of the ratios suggests an issue with the decapolar error model of the main dipoles, with measurements showing values about half of those predicted by the magnetic model.

5.5. Accounting for Decay

FiDeL, the field model used in operation, aims at correcting the field errors at various energies. Measured field errors but also decay estimates with respect to time are used when computing corrections.

Decay happens after cycles in the magnets powering. This happens for example when ramping down from an energy of 6.8TeV to 0 and then going back to injection energy at 450GeV. Some components of the magnetic field will persist and gradually change over time until they reach their final value.

Time [m]	Δb_5
17	-0.38
33	-0.44
50	-0.46
67	-0.47
83	-0.47
167	-0.47

Table 5.6.: Decay of the b_5 component after injection for long time periods [19].

Such corrections thus vary with time as decay changes the field errors of the magnets. For the main dipoles, the sextupolar component b_3 increased relative to time while the b_5 component decreases [19]. While sextupolar decay is used by FiDeL, it has been observed that this was not the case for the decapolar component b_5. The average b_5 field in the main dipoles, taken from the WISE tables and used by FiDeL, is about 1.145 ± 0.5. Decay measurements for various elements relative to time can be seen in Fig. 5.6. Table 5.6 shows the decay expected at injection energy after a typical cycle of machine operation. From this table, it is clear that decay accounts for a large part of the b_5 at injection. $\approx 40\%$ of the compensated b_5 at injection in the main dipoles can indeed attributed to the decay.

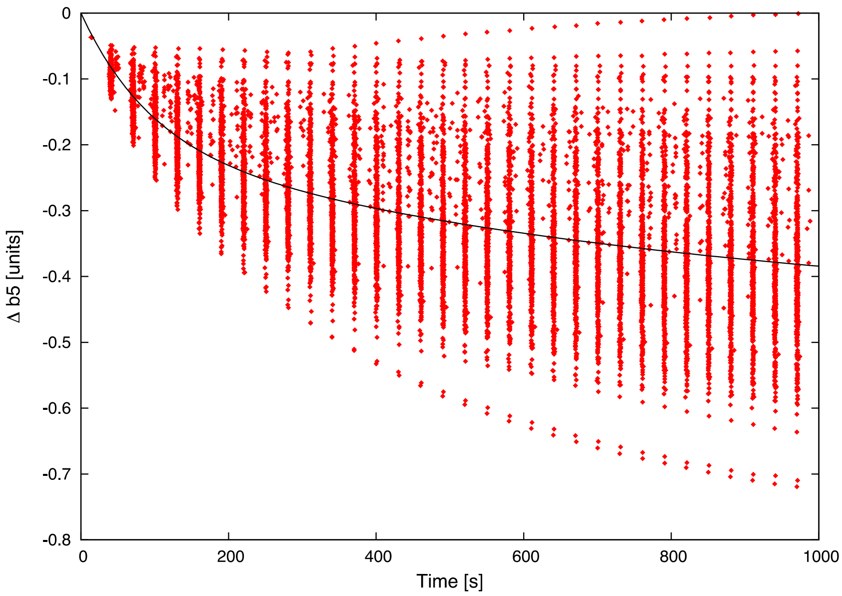

Figure 5.6.: Measured decay of the integrated decapolar field in LHC's main dipoles at injection energy. The fit is shown in black [19].

Chromaticity It has been shown in the previous sections, and particularly in Table 5.4 that measurements and simulations were off regarding the third order chromaticity Q'''. New simulations have hence been conducted to evaluate the effect of this decay on chromaticity. Table 5.7 compares simulations with and without the decay of the b_5 component. The simulations use the 100 available error seeds to calculate error bars.

Condition	Q_x''' [10^6]	Q_y''' [10^6]
No Decay	6.93 ± 0.04	-4.32 ± 0.02
$\Delta b_5 = -0.47$	4.05 ± 0.04	-2.54 ± 0.02

Table 5.7.: Comparison of Q_x''' and Q_y''' for Beam 1 with and without decay of the b_5 component of the main dipoles at injection energy. Fields errors range from normal and skew sextupoles ($n = 3$) to icosapole ($n = 10$).

Integrating the decay of the b_5 component of the main dipoles in the simulations shows a large reduction of the third order chromaticity Q'''. Using the values from the bare chromaticity measurement and updating Table 5.4 with the newly obtain data provides a more accurate comparison of the model to the measurement, as shown in Table 5.8.

Quantity	Measured [10^6]	Simulated [10^6]	Ratio
Beam 1			
Q_x'''	2.95 ± 0.04	4.05 ± 0.04	0.73 ± 0.01
Q_y'''	-1.82 ± 0.04	-2.54 ± 0.02	0.72 ± 0.02
Beam 2			
Q_x'''	3.06 ± 0.07	4.27 ± 0.03	0.72 ± 0.02
Q_y'''	-1.72 ± 0.02	-2.55 ± 0.01	0.67 ± 0.01

Table 5.8.: Measured and simulated third order chromaticity with octupole and decapole correctors turned off. The simulations include field errors from normal and skew sextupoles to icosapole ($n = 3$ to $n = 10$). The b_5 component of the main dipoles has been updated to include decay.

Chromatic Amplitude Detuning Similar to chromaticity, new simulations have been conducted for chromatic amplitude detuning. Table 5.9 gives an overview of the newly computed values and the related ratios relative to the measurements, while Fig. 5.7 gives a visual clue. Following the same trend as for chromaticity, the measured values are now closer to the model.

Type	$\frac{\partial^2 Q_x}{\partial J_y \partial \delta}$ [$10^4\mathrm{m}^{-1}$]	$\frac{\partial^2 Q_y}{\partial J_y \partial \delta}$ [$10^4\mathrm{m}^{-1}$]
$\delta = +0.001$		
Meas.	-1.16 ± 0.08	1.26 ± 0.15
Sim.	-2.35 ± 0.01	1.50 ± 0.01
Ratio	0.49 ± 0.03	0.84 ± 0.10
$\delta = -0.001$		
Meas.	1.47 ± 0.12	-1.18 ± 0.13
Sim.	2.46 ± 0.01	-1.45 ± 0.01
Ratio	0.60 ± 0.05	0.82 ± 0.09

Table 5.9.: Comparison of the measured and simulated terms $\frac{\partial^2 Q_x}{\partial J_y \partial \delta}$ and $\frac{\partial^2 Q_y}{\partial J_y \partial \delta}$ via PTC, at two discrete momentum offsets. Simulations include errors from normal and skew sextupoles to icosapole ($n = 3$ to $n = 10$), as well as the decay of the b_5 component of the main dipoles.

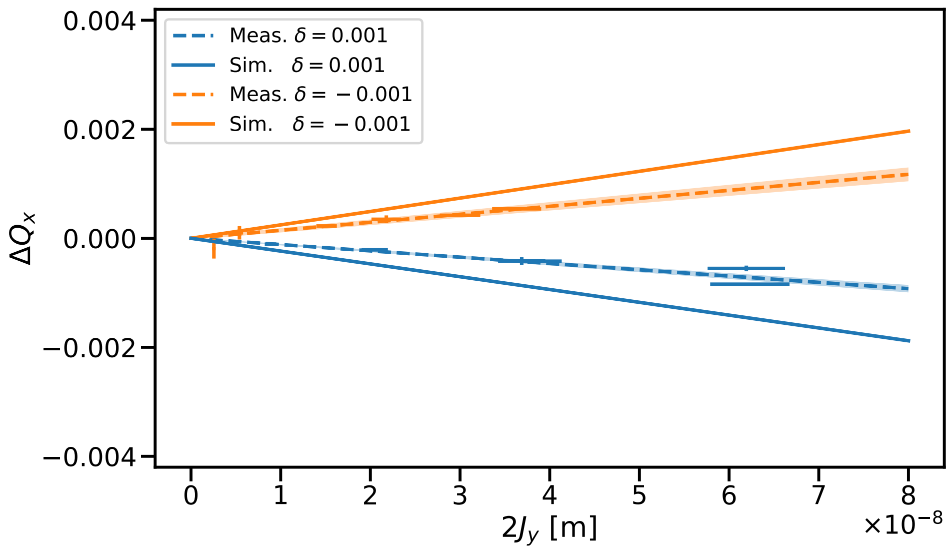

(a) Horizontal tune shift depending on the vertical action: $\frac{\partial^2 Q_x}{\partial J_y \partial \delta}$.

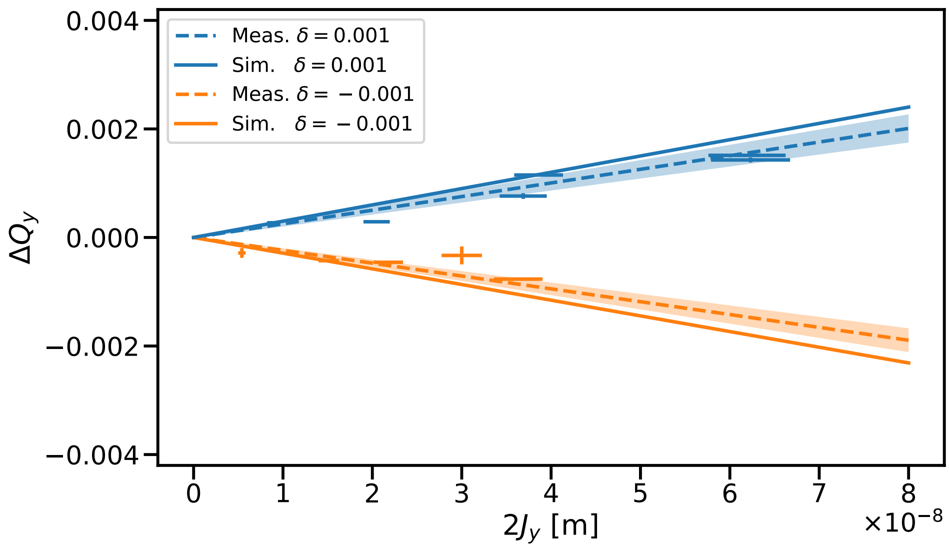

(b) Vertical tune shift depending on the vertical action: $\frac{\partial^2 Q_y}{\partial J_y \partial \delta}$.

Figure 5.7.: Measured and simulated tune shift depending on the action at two different momentum offsets. Each fit corresponds to a chromatic amplitude detuning term evaluated at a certain δ. Estimates from simulations are lowered due to the b_5 decay of the main dipoles.

5

5.6. Resonance Driving Terms

Decapoles, due to their order, contribute to many RDTs. Indeed, 50 of them can be theoretically observed in simulations and measurements. In practice, the contributions of individual multipoles become indistinguishable as many resonances or lines overlap, making it impossible to isolate certain terms. Some resonances, described in Appendix C, are unique to certain multipoles when considering no too high orders. Those resonances, provided that they are sufficiently strong and the beam close to them, can be measured via their RDTs.

Of interest to the LHC Operation, is the RDT f_{1004}, driving the resonance $1Q_x - 4Q_y$. It can be seen in the horizontal frequency spectrum at $-4Q_y$ with an amplitude dependence on J_y^2. Figure Fig. 5.8 shows a frequency map [65] of a simulation including decapolar field errors, where their impact on the beam is easily noticeable. The red particles evolving close to the resonance are affected by it and are subject to large tune shifts. Eventually, those particles are lost when their amplitude becomes too large.

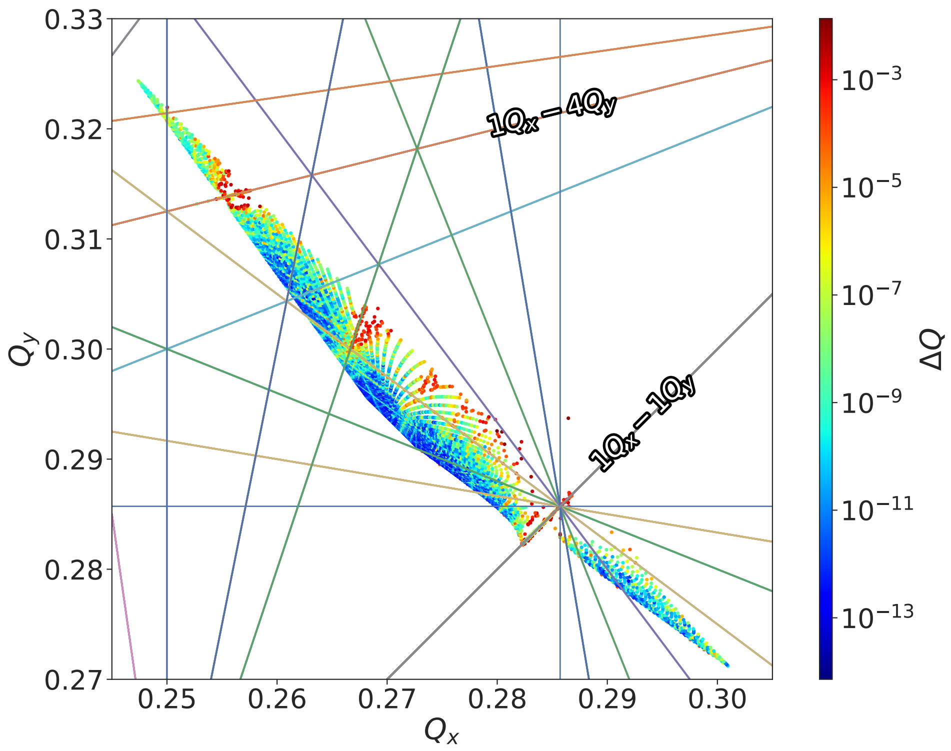

Figure 5.8.: Frequency map at injection energy, with decapolar field errors and nominal settings for landau octupoles. The highlighted resonance (1,-4), excited by decapoles, shows a degradation over 20,000 turns. The tune shift between the start and the end of the simulation is indicated in color.

Measuring turn-by-turn data without using any excitation is not a viable option as amplitudes are not large enough. Spectral lines are indeed usually impossible to discern from the noise floor, making RDTs not measurable. Measurements are hence taken with an AC-Dipole, introducing quadrupolar-like field errors in the linear regime [58] and more complex effects in the non linear regime. In practice, those effects are neglected. *Forced* RDTs are measured with an AC-Dipole and treated as *free* as no compensation is applied.

Such forced measurements were taken for the first time in the LHC to observe the f_{1004} RDT at injection energy. The frequency line of the resonance $1Q_x - 4Q_y$ is seen at $4Q_y$ in the horizontal spectrum, as shows Fig. 5.9.

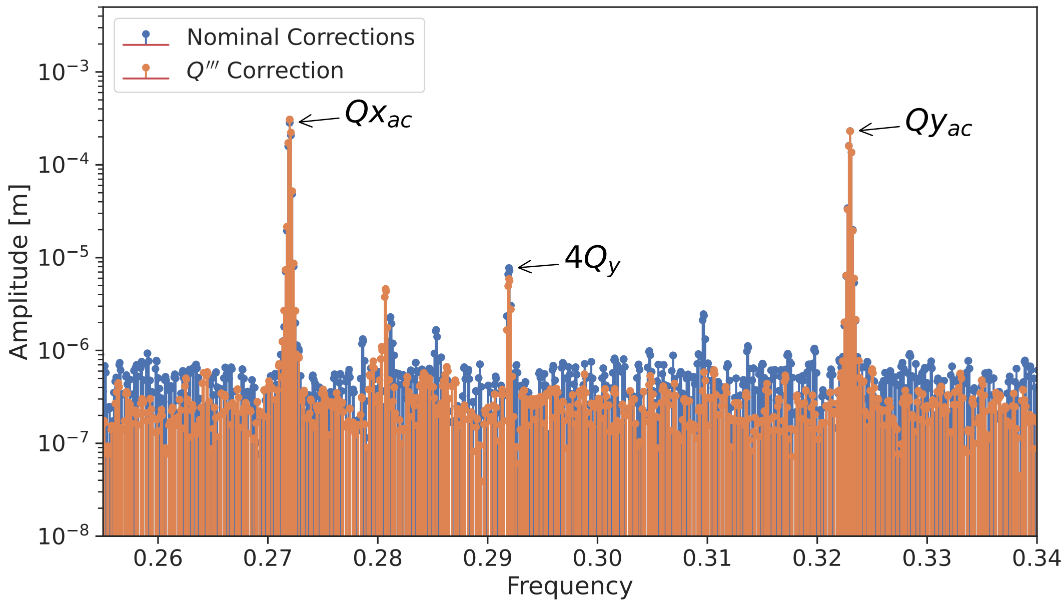

Figure 5.9.: Horizontal frequency spectrum of turn-by-turn data, with nominal and beam-based corrections for the third order chromaticity Q'''. The $1Q_x - 4Q_y$ resonance can be seen at $-4Q_y$ with different amplitudes for each correction scheme.

5

5.6.1. Decapolar Contribution

Decapolar fields are the main contributors to the RDT f_{1004}. As such, powering the decapolar correctors is a good way to correct the related resonances. Being linear with the strength of the correctors, the RDT can be corrected via a response matrix.

Measurements were taken in order to attempt such a correction and get a baseline for the amplitude of the RDT without decapolar correctors and with the nominal FiDeL corrections applied. Corrections were made on the base of those nominal settings and applied on top. The strength of the decapolar correctors is shown in Table 5.10 for the FiDeL settings, the delta applied on top and the final correction values.

Circuit	FiDeL $K_5\,[\mathrm{m}^{-5}]$	$\Delta K_5\,[\mathrm{m}^{-5}]$	$K_5\,[\mathrm{m}^{-5}]$
Beam 1			
RCD.A12B1	−4582	6055	1473
RCD.A23B1	−5106	7	−5099
RCD.A34B1	−4855	3827	−1028
RCD.A45B1	−4577	−4746	−9323
RCD.A56B1	−4125	−4903	−9028
RCD.A67B1	−5166	2961	−2205
RCD.A78B1	−6827	3593	−3234
RCD.A81B1	−5500	2380	−3120
Total	−40738	9174	−31564
Beam 2			
RCD.A12B2	−4490	3639	−851
RCD.A23B2	−5155	−1147	−6302
RCD.A34B2	−4825	−1038	−5863
RCD.A45B2	−4619	3986	−633
RCD.A56B2	−4064	2944	−1120
RCD.A67B2	−5066	2357	−2709
RCD.A78B2	−6866	−2952	−9818
RCD.A81B2	−5446	1825	−3621
Total	−40531	9614	−30917

Table 5.10.: Strength of decapolar correctors with nominal FiDeL settings and after application of corrections aiming at reducing both the RDT f_{1004} and Q'''. The total value as a direct incidence on the chromaticity

5

This RDT correction also serves as a partial Q''' correction. To fully correct Q''' indeed approximately requires a strength of $+13,000K_5$ distributed amongst the correctors. Therefore, this new approach reduces Q''' by about 70% compared to the previous method. The chromatic amplitude detuning terms are also expected to be decreased. Result of those measurements, as well as the inverse of the correction, are shown in Fig. 5.10

Although the FiDeL scheme was not intended to correct the RDT but rather only Q''', it would be expected for it to lower the amplitude of the RDT. It can though be seen that it degrades the resonance compared to the machine with no decapolar correctors. On the other hand, the newly computed RDT correction does lower the amplitude of f_{1004} as expected. Its inverse has the opposite effect.

Simulations were run with decapolar correctors turned of and with the absolute value of the RDT correction. The response of the RDT between those two schemes is shown in Fig. 5.11. The difference

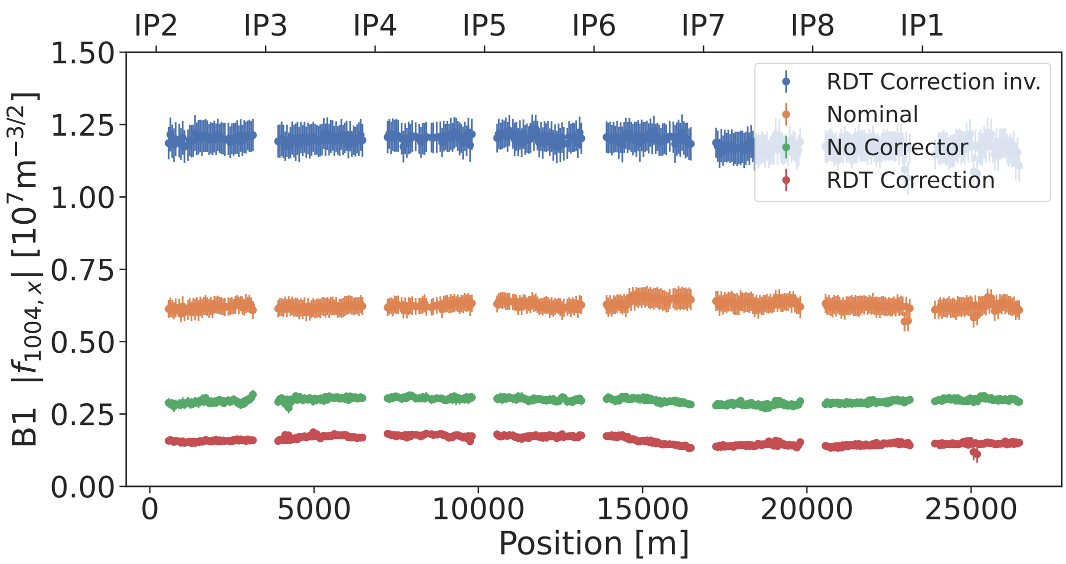

(a) $|f_{1004}|$ for Beam 1

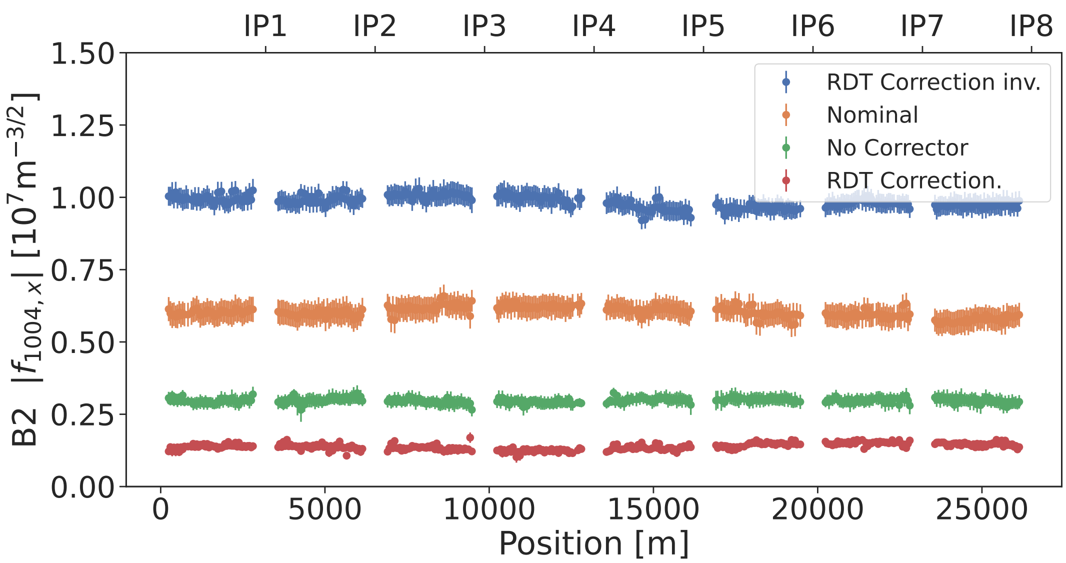

(b) $|f_{1004}|$ for Beam 2

Figure 5.10.: Measured f_{1004} with decapolar correctors powered off, nominal settings, and combined RDT & Q''' correction with normal and opposite signs.

between their RMS value ratio is $\approx 6\%$, indicating that simulations correctly model the decapolar correctors.

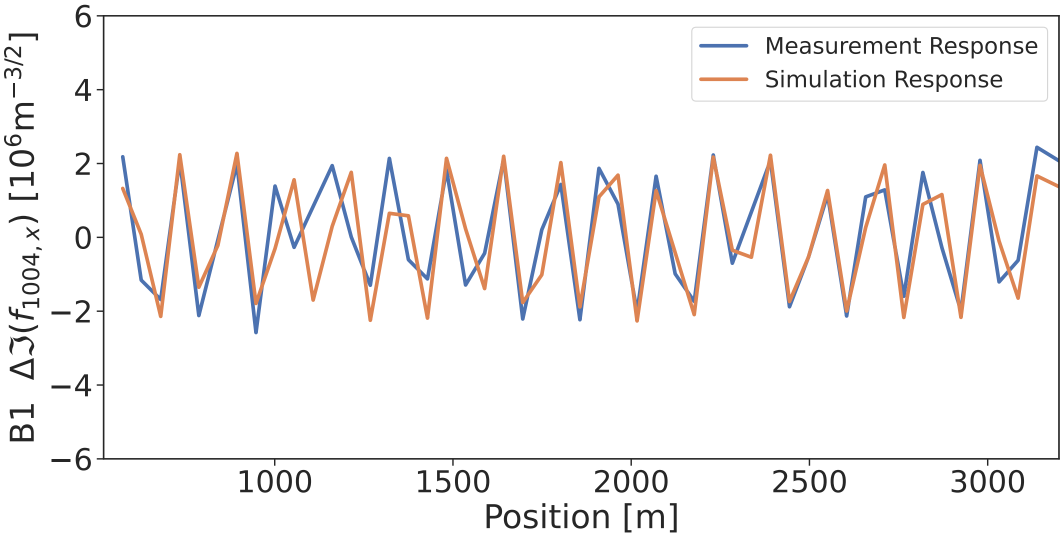

Figure 5.11.: Comparison for measurement and simulation of the response of the imaginary part of f_{1004} upon application on unpowered correctors of the RDT corrections.

5.6.2. Feed-Up Contributions

First Observation

As described in Appendix A, multipoles can combine to create fields that are seen as higher orders when considering higher orders of the BCH expansion. For decapoles, combinations of several sextupoles and sextupoles with octupoles give rise to decapolar-like fields, as described in Table A.3. The following parts of this section will describe those combinations.

This effect was observed in 2022 during Run 3's commissioning. New corrections of the non-linear chromaticity Q'' and Q''' were performed, and RDT measurements taken before and after their correction. As Q''' was corrected, the expectation was that the RDT f_{1004} would also lower with the reduction of the decapolar strengths K_5. However, an increase of the RDT was observed, as shows Fig. 5.12.

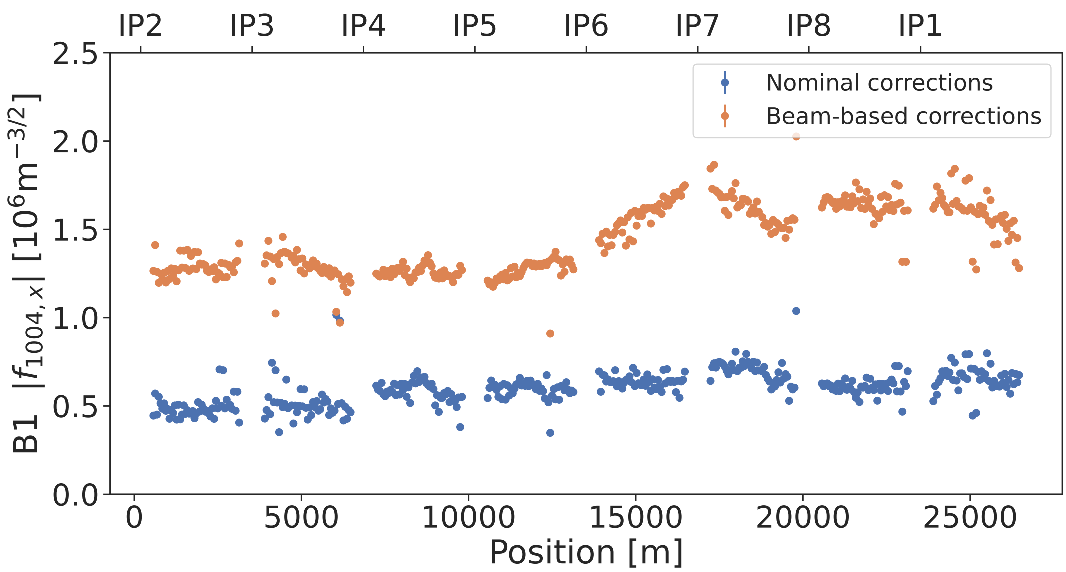

Figure 5.12.: Non intuitive increase of the RDT f_{1004} after application of both the Q'' and Q''' corrections.

Action Dependance and Analysis

Resonance lines in the frequency spectrum are often contributed to by several multipoles. Some lines start getting a contribution with rather high multipole orders, like the RDT f_{1004} considered here. The line $4Q_y$ in the horizontal spectrum is indeed contributed to by decapoles and then only by decatetrapoles. When the main contributing field alone is varied, it is easy to reconstruct the RDT, as its fit is only dependant its action dependance ($\propto J_x^* J_y^*$). Several turn-by-turn measurements at the same configuration can be taken wit varying kick amplitudes, refining the RDT value with more data points for the fit.

Considering the contribution of lower order multipoles is a bit trickier, as the second order RDTs change the dependance of the frequency line [66]. In order to be able to compare the RDT from several turn by turn measurements, the same kick amplitude must then be used. Failing to do so would lead to a poor fit of the line amplitude relative to the action, resulting in an RDT with incorrect amplitude and significant noise.

Sextupoles

At the third order of the BCH expansion, the combination of two sextupoles yields a decapolar-like expression. This means that, during normal operation of the machine, decapolar observables will be altered when adjusting parameters such as the linear chromaticity Q'. Derivation of such a combination

5

can be found in Appendix A.2.2. The resulting Hamiltonian indeed is similar to the terms of a decapole, dropping the $p_{x,y}$ terms for readability:

$$\begin{aligned}(H_3)^3 &\propto \frac{1}{48}\left(x^5 - 2x^3y^2 - 3xy^4\right)\\ &\sim x^5 - 10x^3y^2 + 5xy^4.\end{aligned} \tag{5.5}$$

To quantify the actual impact of such an equation on the LHC, a simulation was run with injection optics while varying this same linear chromaticity Q'. No higher fields than sextupoles are have been included, including field errors. The resulting effect on the RDT f_{1004} can be seen in Fig. 5.13.

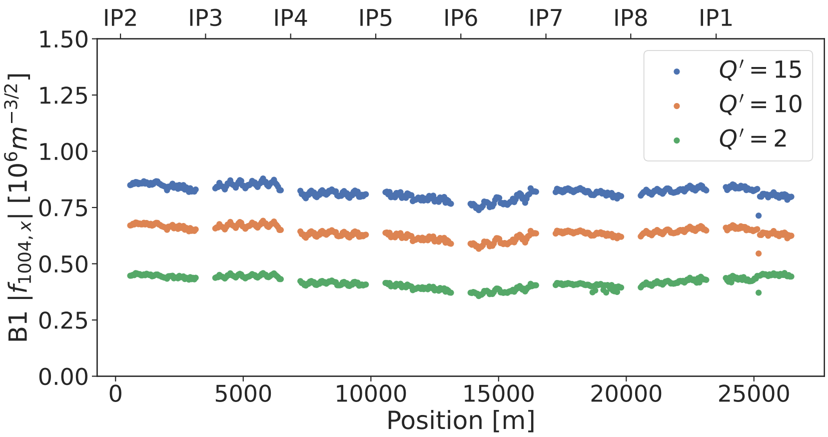

Figure 5.13.: Simulated change of the decapolar RDT f_{1004} with varying linear chromaticity Q' generated by sextupoles. The combination of sextupolar fields clearly shows a increase in decapolar RDT.

5

As the linear chromaticity increases, the overall K_3 strength of sextupoles actually becomes more negative. Considering the previous Eq. (5.5), a higher chromaticity is expected to increase the amplitude of the RDT f_{1004}, related to the last term xy^4. Figure 5.14 shows how the RDT is expected to vary, depending on the overall sextupoles strength and the linear chromaticity. It can be noted that although the relation between K_3 and Q' is linear, that of K_3 and the RDT varies with the cubed strength. Using the sum of the cubed strength is possible due to the chromaticity knob being a factor applied on all sextupoles at the same time.

To confirm what is observed in simulations, measurements were performed by varying Q' and kicking the beam with the AC-Dipole. Limited by losses, up to three measurements with distinct Q' were taken, as shows Fig. 5.15.

Like in simulations, it is observed that an increase in Q' translates to an increase in $|f_{1004}|$. The scale of the amplitude is though one order of magnitude higher than that of simulations. An offset for all

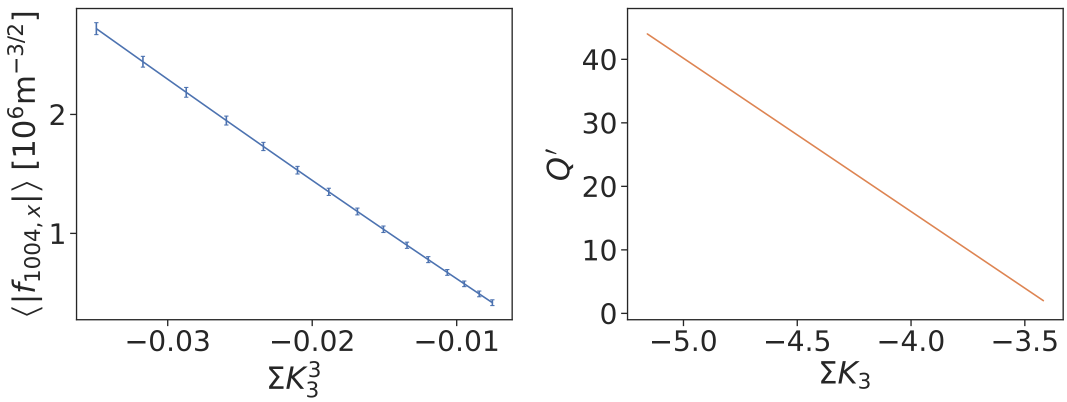

Figure 5.14.: Average amplitude of the decapolar RDT f_{1004} depending on the overall strength of the sextupoles used to control the linear chromaticity Q'. The right plot can be used to relate the RDT amplitude to a specific Q' value.

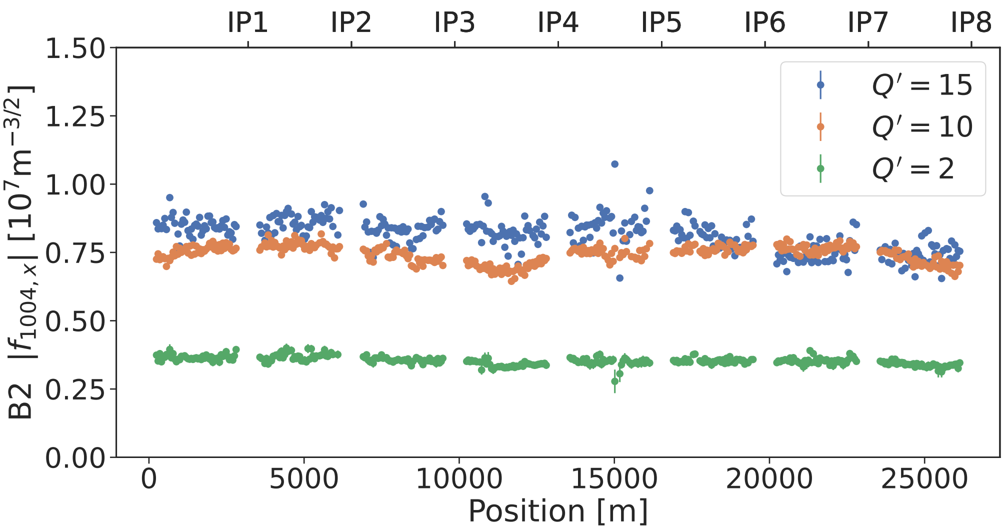

Figure 5.15.: Measured change of the decapolar RDT f_{1004} depending of the desired linear chromaticity Q' generated by sextupoles. It is to be noted that the vertical axis is one order of magnitude higher than the previous simulations' plot.

measurements could be explained by non-included field-errors. The shift between them however should be similar between machine and simulations, this could be due by the interaction of the sextupolar fields with octupoles, as detailed in the following section. More data points with varying Q' at similar kick amplitudes would be required to further investigate.

Sextupoles and Octupoles

At the second order of the BCH expansion, the combination of a sextupole and an octupole yields a decapolar-like expression. Like sextupoles, octupoles are used in operation, thus contributing to decapolar fields. This happens amongst other when correcting the second order chromaticity Q'' and most importantly with the Landau Octupoles, which are powered to high strengths at injection energy to introduce Landau damping [9]. Derivation of such a combination can be found in Appendix A.2.3. The resulting Hamiltonian indeed is similar to the terms of a decapole, dropping the $p_{x,y}$ terms for readability:

$$\begin{aligned} H_3H_4 &\propto \frac{1}{24}\left(x^5 + 2x^3y^2 + xy^4\right) \\ &\sim x^5 - 10x^3y^2 + 5xy^4. \end{aligned} \tag{5.6}$$

In order to assess the previous equation, simulations were run with several configurations. As seen previously, a combination of two sextupoles creates a decapolar-like field, varying their field is thus not needed. Rather, a set of two configurations was run to check the impact of octupoles alone. The first configuration is ran with all sextupoles of the machine turned off, while octupoles are powered. The second configuration turns off all sextupoles and octupoles. Figure 5.16 shows the resulting RDT f_{1004} from these simulations. It is there apparent that varying octupoles without sextupoles does not have any effect on this RDT.

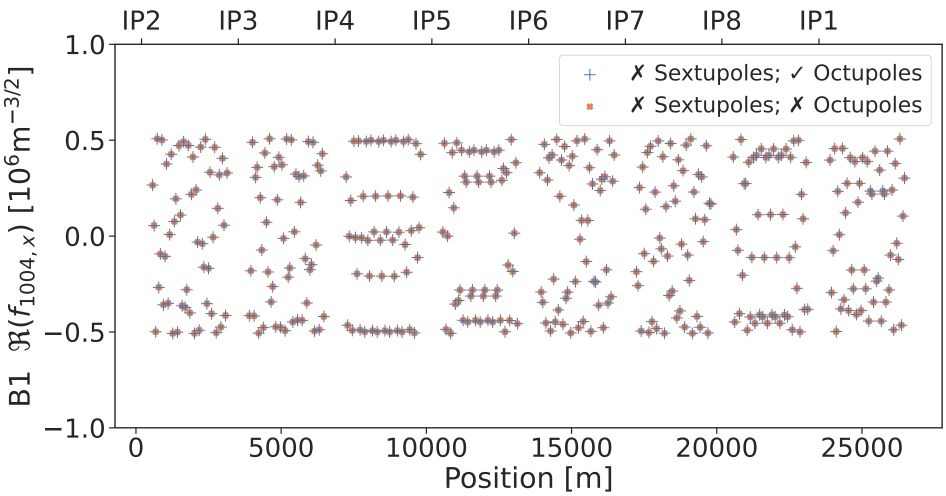

Figure 5.16.: Simulated decapolar RDT f_{1004} with two different schemes. First scheme has lattice sextupoles turned off and octupoles turned on. Second scheme has all sextupoles of the lattice turned off and octupoles turned off as well. No difference is seen, as expected from the equations.

The most powerful octupoles used in operation are the lattice octupoles, used for Landau damping. Figure 5.17 shows a simulation ran with varying strengths of those magnets. It can be noted here that the shift of the RDT is almost of an order of magnitude, making octupoles a large contributor to the decapolar fields.

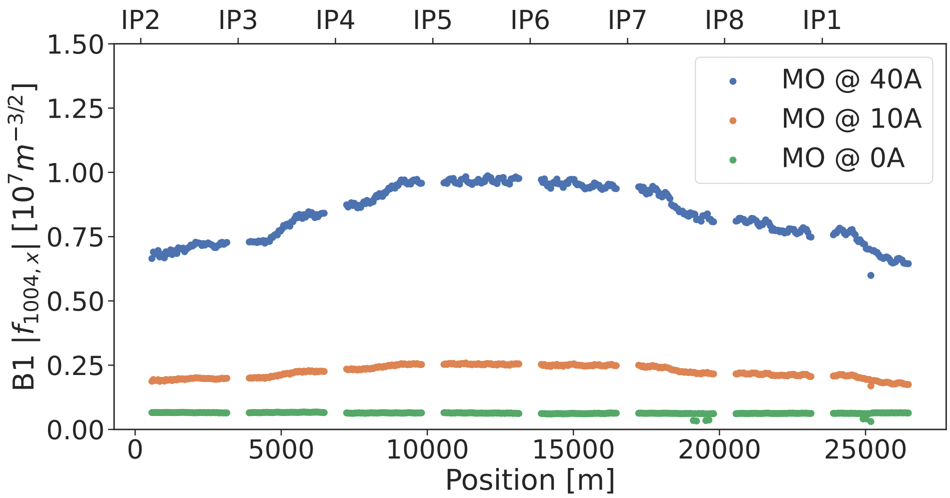

Figure 5.17.: Simulated change of the decapolar RDT f_{1004} depending of the strength of the lattice octupoles used for Landau damping.

While decapoles are expected to be the main contributors to decapolar fields, other strong sources can indeed be identified. Figure 5.18 shows the average amplitude of the RDT f_{1004} depending on the error sources introduced in the simulations. A large contribution comes from the octupolar errors in the main dipoles, being actually larger than the decapolar errors in those magnets.

Measurements were performed to confirm and quantify the effect of octupoles coupled with sextupoles on the decapolar fields. Previous corrections, aimed at correcting the second order chromaticity Q'', via octupolar correctors *MCO*, were applied with varying factors. Such corrections apply use a uniform trim on all correctors of $\approx +2.5K_4$. Figure 5.19 shows a comparison of the resulting RDT with those corrections at factors -10, -4, -1 and 0.

Factor	RMS $\lvert f_{1004}\rvert$
-10	37, 308, 159
-4	6, 721, 270
0	3, 533, 796
-1	2, 333, 384

Table 5.11.: RMS of $|f_{1004}|$ depending on the factor of the Q'' corrections.

Table 5.11 shows the RMS of the amplitude of this RDT for the various configurations. Similar to the shift observed when powering the landau octupoles in simulations, the shift is of one order of magnitude between factors -0 and -10. Measurements with landau octupoles were also attempted but losses made it impossible to obtain high enough amplitudes to correctly measure the RDT.

5

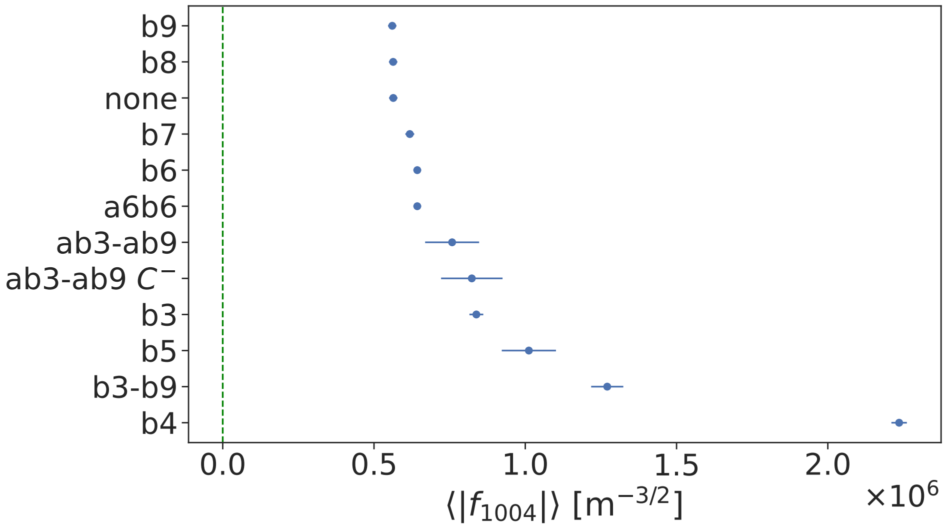

Figure 5.18.: Simulation of the amplitude of the decapolar RDT f_{1004} depending on the field errors applied on main dipoles as well as coupling (C^-). While it is apparent that some multipolar errors drive the resonance higher, some combinations actually seem to cancel each other.

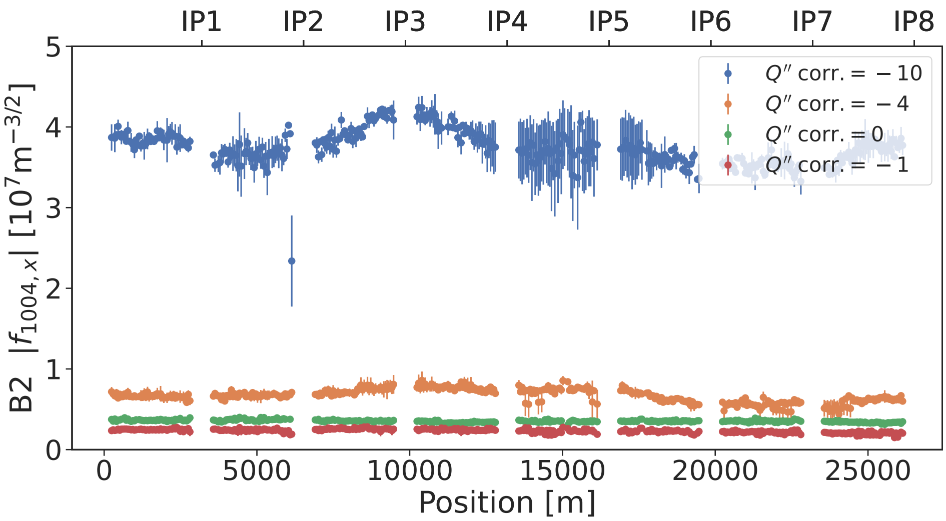

Figure 5.19.: Shift of the decapolar RDT f_{1004} depending on the factor applied on octupolar corrections for Q''.

Simulated and observed large shifts due tu octupoles are relevant to the operation of the LHC, as resonances can be greatly deteriorated, especially when powering landau octupoles. A better understanding of the interaction between Landau octupoles and octupolar correctors could lead to improved corrections in not only octupolar but also decapolar fields in the future.

5.6.3. Feed-Down Contributions

To produce collisions at top energy, *crossing angles* are introduced via the orbit correctors located in the triplets, before the separation dipoles and the matching section of the interaction regions (MCBX, MCBY and MCBC) [67]. Those collisions happen with a small $\beta*$, currently 30cm, requiring strong quadrupolar fields from the triplets.

At such β, those triplets also generate strong dodecapolar field errors. Because of the crossing-angles, feed-down appears and lower-order fields can be observed. Such feed-down to decapolar fields was observed during the first commissioning of Run 3, in 2022 [68]. Figure 5.20 shows how the RDT f_{1004}, normally affected by decapoles, varies with the application of crossing angles.

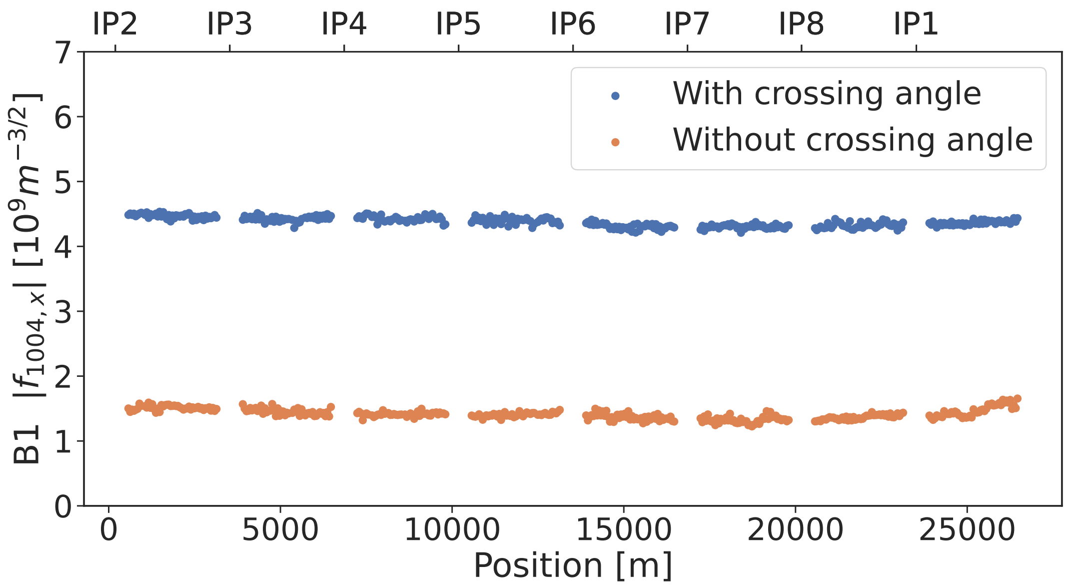

Figure 5.20.: Varying amplitude of the decapolar RDT f_{1004} at top energy depending on the activation or not of the crossing angle at the IP. Offsets in orbit create feed-down from higher orders.

Such a contribution is though not expected at injection energy, as the triplets aren't powered a much as at top energy, $\beta*$ being set at around 10m.

5.7. Impact of Decapolar Fields

Decapolar fields can influence the beam lifetime in several ways. Chromatic amplitude detuning and chromaticity will induce a tune shift, relative to either or both the action and the momentum offset. After such detuning, particles may move closer to certain resonances in tune space, causing their oscillations to grow, eventually leading to their loss.

5.7.1. Large RDT

As seen previously in Fig. 5.8, the resonance $1Q_x - 4Q_y$ passes through the beam in tune space, deteriorating the lifetime of the nearby particles. In order to measure the impact of this resonance on the beam, a knob was created, alternating the current of all decapole correctors in the machine arc by arc. Such a powering scheme has no impact on chromaticity as the sum of the strengths K_5 is zero. Rather, the RDT f_{1004} is impacted. Is it to be noted that this is not a correction, but purely a way to artificially increase the RDT in order to quantify the effect of the resonance.

ΔK_5	RMS $\lvert f_{1004}\rvert$
0	618, 947
±10500	17, 566, 377
∓10500	17, 623, 867

Table 5.12.: RMS of $|f_{1004}|$ relative to the powering scheme of decapolar correctors.

Starting with nominals corrections for Q''' corrections, a delta of $\pm 10500 K_5$ is applied on each decapolar correctors. Figure 5.21 shows the response of the real part of the RDT for this scheme and its inverse. The amplitude of the RDT is on a similar level as the shift is significantly larger than the original level of the RDT. Table 5.12 indicates the amplitude of the RDT created with each knob value.

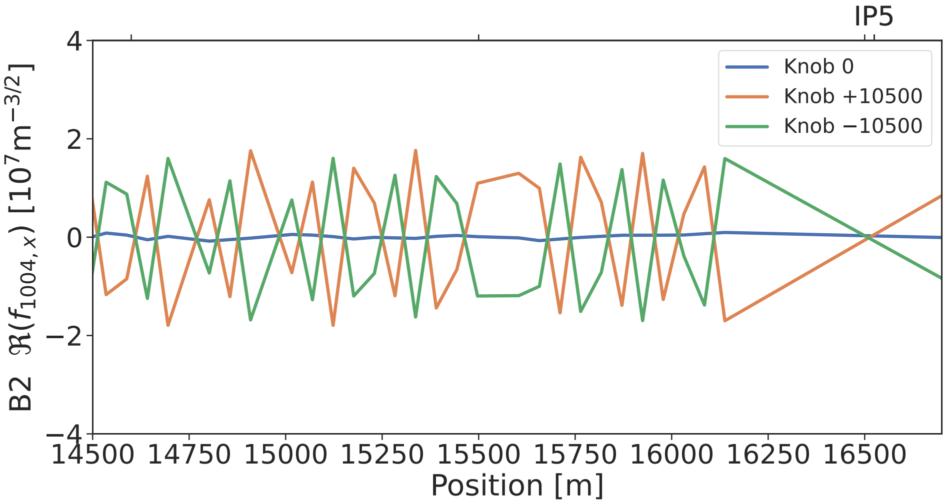

Figure 5.21.: Measured real part of the RDT f_{1004} depending on the powering scheme of the decapolar correctors.

In order to measure the lifetime, a long period must be allocated as the signal returned from monitors can be jittery. Figure 5.22 shows this lifetime depending on the decapolar strength scheme applied. The current of only one circuit is shown for readability. A current of ≈ 230 corresponds to a knob value of +10500 while a current of −45 corresponds to 0.

It is clear from this measurement that a large RDT decreases the lifetime of the beam. The first pair

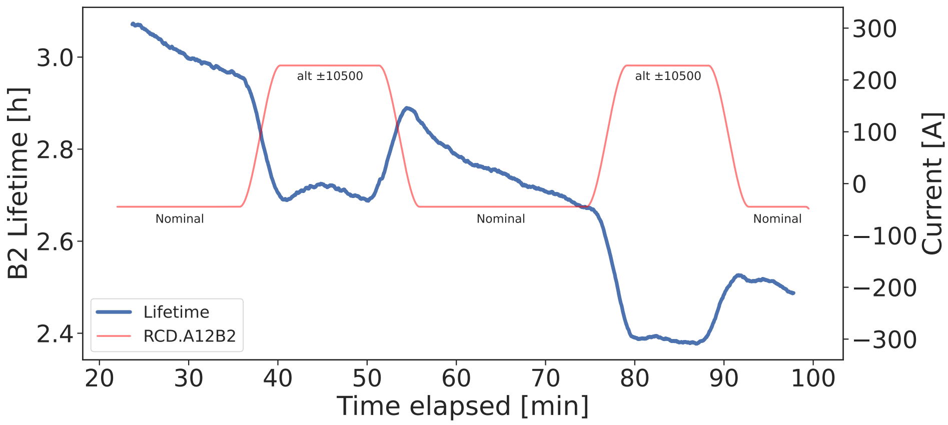

Figure 5.22.: Measured lifetime of Beam 2 upon application of two different powering schemes for decapolar correctors. One trim keeps the RDT at a low amplitude while the other greatly amplifies it.

of trim sees the average lifetime decreasing of 0.31 ± 0.03 hours, while the second one sees a decrease of 0.36 ± 0.03 hours. This observed decrease of 20 minutes accounts for 10% of the beam lifetime at injection energy.

5.7.2. Corrections

In order to understand what can be gained from correcting decapolar fields, a lifetime measurement was taken with the corrections described in Section 5.6.1. This scheme corrects the three decapolar observables, being the RDT f_{1004} linked to the resonance $1Q_x - 4Q_y$, the third order chromaticity Q''' and the chromatic amplitude detuning terms. Figure 5.23 shows the evolution of the lifetime, starting with corrections applied, removed and then trimmed to their opposite. A net change in lifetime for Beam 1 can be measured after each application. Acquired signal for Beam 2 has been deemed too noisy to be relevant, due to the shortness of the measurement.

It is apparent here that the corrections have a beneficial effect on the beam. The lifetime improvement is of $\approx 3\%$, while the degradation after applying the opposite is of $\approx 5\%$. Further developments in the correction scheme and lengthier measurements could easily improve this lifetime gain.

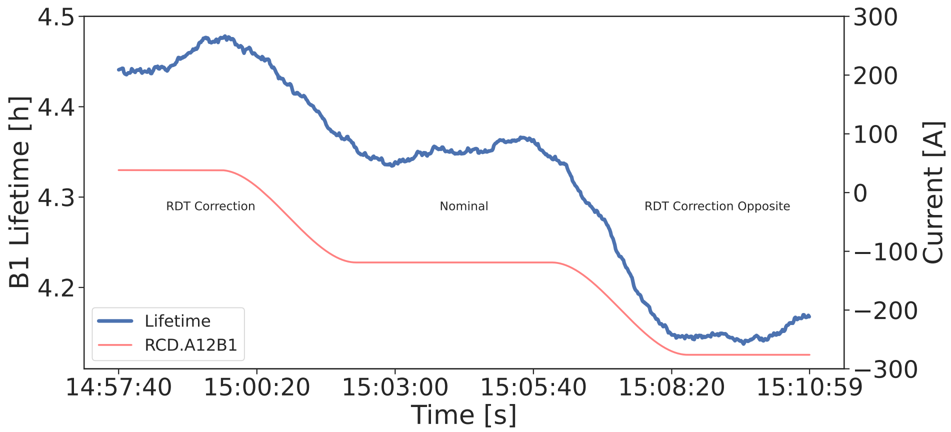

Figure 5.23.: Measured lifetime of Beam 1 with the nominal corrections for Q''', combined correction of f_{1004} and Q''', and its inverse.

5.8. Summary

This chapter examines the role of decapolar fields in the Large Hadron Collider (LHC) at injection energy. First is addressed the previously observed discrepancy between measurements and model regarding the third-order chromaticity. To investigate these issues, various measurements and simulations were conducted. By introducing novel observables, such as the bare chromaticity and, for the first time, chromatic amplitude detuning, a clearer understanding of these discrepancies was achieved. Simulations indicate that the decay of the decapolar component in the main dipoles is a major factor contributing to the discrepancies.

For the first time at injection energy, measurements and corrections of the decapolar Resonance Driving Term (RDT) f_{1004} were carried out. Further simulations and measurements explored how sextupoles and octupoles interact to create decapolar-like fields. The findings revealed that sextupoles, both alone and in combination with Landau octupoles, generate substantial decapolar RDTs during machine operation that could benefit from corrections.

Applying combined corrections for third-order chromaticity, chromatic amplitude detuning, and the RDT f_{1004} led to a 3% improvement in beam lifetime. Additionally, a broader impact of decapolar RDTs on beam stability was investigated. Specifically, intentionally degrading the RDT f_{1004} resulted in a decrease in beam lifetime of about 10%. This underscores the importance of these corrections for stable beam operation and suggests that further advancements in correction methods could lead to even greater improvements.

6 Higher Order Fields

6.1. Introduction

Beam-based high order field measurements have been carried out in the LHC since its first Run [59, 60], via chromaticity studies. Those measurements, made by varying the RF frequency while observing the resulting tune change, have been performed with a momentum offset of up to $\delta = \pm 2.2 \times 10^{-3}$, which led to the observation of the third order term of the non-linear chromaticity.

During the commissioning of Run 3 in 2022, a new collimator sequence has been introduced, allowing wider momentum offset measurements, within $\delta \in [-3.2 \times 10^{-3}, 3.7 \times 10^{-3}]$. This improved setup led to the observation of the fourth and fifth order terms at injection energy. Those terms, denoted $Q^{(4)}$ and $Q^{(5)}$ respectively in Eq. (6.1), are produced to first order by dodecapoles and decatetrapoles. Dodecapoles being powered off at injection and decatetrapoles being absent from the lattice, those fields originate from the field errors of the various magnets installed in the LHC.

$$Q(\delta) = Q_0 + Q'\delta + \frac{1}{2!}Q''\delta^2 + \frac{1}{3!}Q'''\delta^3 + \frac{1}{4!}Q^{(4)}\delta^4 + \frac{1}{5!}Q^{(5)}\delta^5 + \mathcal{O}(\delta^6). \tag{6.1}$$

In addition to completing the measurements of high-order fields through chromaticity scans, turn-by-turn measurements were also conducted. High amplitude kicks indeed made it possible to observe dodecapolar RDTs in the LHC for the first time. Such fields were never before observed directly, but rather only via feed-down to amplitude detuning [14].

6.2. Chromaticity

6.2.1. Procedure

As described in Section 3.2.3, the momentum offset δ is related to the RF frequency and the momentum compaction factor. This relation is given as a simplified form in Eq. (6.2). The model α_c for the LHC injection optics is 3.48×10^{-4} for beam 1 and 3.47×10^{-4} for beam 2. Via this relation, a change of 140Hz of the RF frequency corresponds to a momentum offset of about -0.001.

$$\delta = -\frac{1}{\alpha_c} \cdot \frac{\Delta f_{RF}}{f_{RF,nominal}}. \tag{6.2}$$

To properly characterize higher orders of the chromaticity function and ensure quality measurements, several steps are required. The tune measured during chromaticity scans can exhibit jitter and resonance lines may appear, requiring thorough data cleaning to either reject problematic data points or reduce error bars. The simplified Eq. (6.2), describing δ, has been sufficient for reliably measuring up to the third order chromaticity. However, this relation also needs verification.

Noise and Spectral Lines

Noise lines, due to electronics, can be seen in the raw data obtained from the BBQ tune system. Occasionally, when those resonances are strong, their frequency peak can be mistaken as the tune and logged as such by the system. This yield large uncertainties in the measurement when data points can't properly be classified as outliers. A tune measurement presenting this issue is showed in Fig. 6.1.

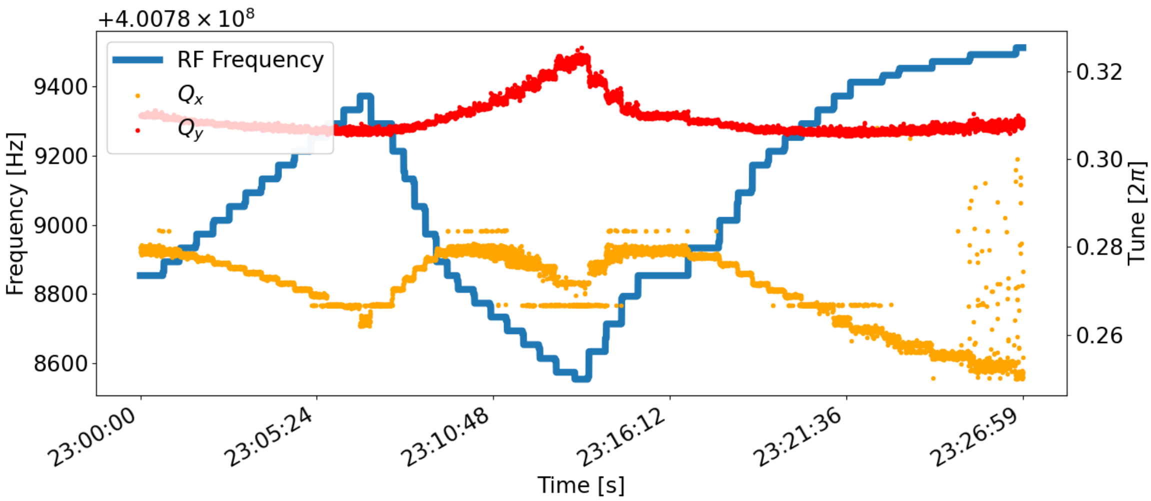

Figure 6.1.: Shift of the tune by variation of the RF. Noise lines can appear in some cases, making the tune error bar large or downright unusable.

A solution to this issue is to use the raw data extracted from the BBQ system. From there, a spectrogram clearly shows the noise lines, as seen in Fig. 6.2. Those lines have been repeatedly identified over several measurements and confirmed to be fixed. The highest peak of the spectrogram can thus be safely identified by removing those resonances, yielding a cleaner measurement. It is also to be added that the BBQ requires to set a tune window, which can be forgotten. By analyzing the raw data, it is ensured that the measurement has usable data and does not try to measure noise.

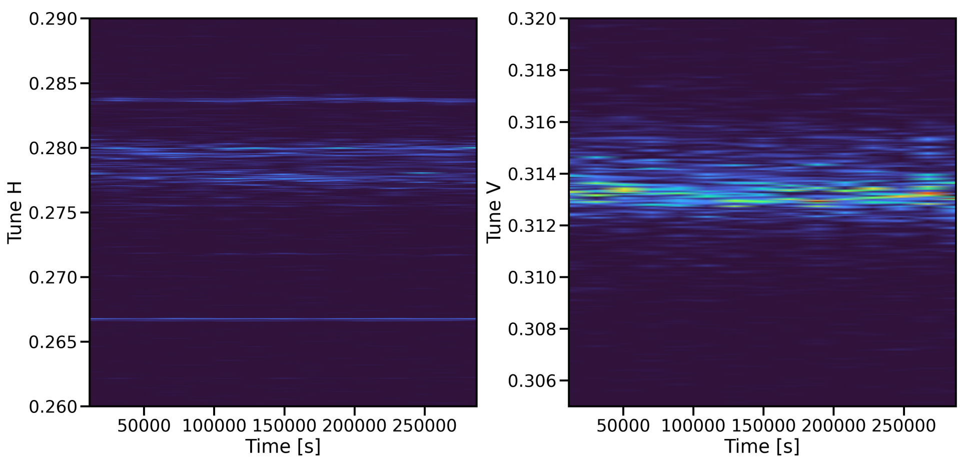

Figure 6.2.: Tune spectrogram obtained via BBQ system. Strong resonance lines can be seen above and below where the tune really is, causing the wrong frequency peak to be identified as the tune.

6

Momentum Compaction Factor

Rather than a constant, the momentum compaction factor can be expressed as an expansion, as detailed in Section 2.5.1. The first terms are given by the following,

$$\alpha_c = \underbrace{\alpha_{c,0}}_{1^{\text{st}}\text{ order}} + \underbrace{\alpha_{c,1}\delta}_{2^{\text{nd}}\text{ order}} + \underbrace{\alpha_{c,2}\delta^2}_{3^{\text{rd}}\text{ order}} . \tag{6.3}$$

The expression for δ at first and second order then reads,

$$\begin{aligned} \delta &= -\frac{\Delta f_{RF}}{\alpha_0 f_{RF}} && \Rightarrow \text{Order 1} \\ \delta &= \frac{-\alpha_0 f_{RF} + \sqrt{f_{RF}\left(-4\Delta f_{RF}\alpha_1 + \alpha_0^2 f_{RF}\right)}}{2\alpha_1 f_{RF}} && \Rightarrow \text{Order 2} \end{aligned} \tag{6.4}$$

It is assumed that only the first term is relevant as the induced difference in chromaticity is negligible as will be demonstrated later on. Figure 6.3 shows the non linearity of the momentum compaction factor and its effect on the calculated δ via the previous formulas.

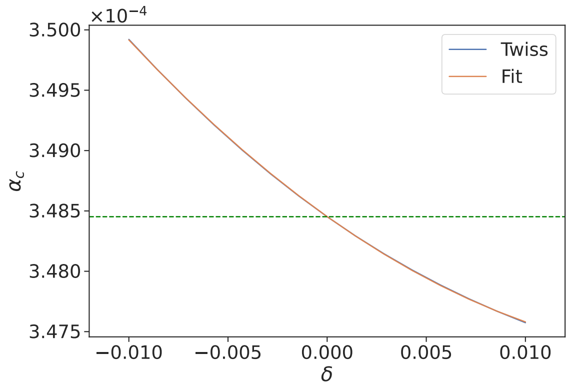

(a) Non-linear fit of α_c obtained via an evaluation at discrete δ in MAD-X. The green line represents a constant $\alpha_c = \alpha_{c,0}$.

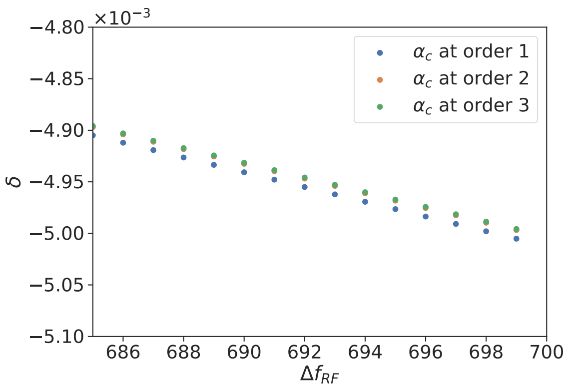

(b) Divergence of the momentum offset when considering higher α_c orders with large RF trims.

Figure 6.3.: Non linearity of α_c and its effect on the computed δ via RF trims. The simulations are done at injection energy of 450GeV.

It is observed that while clearly depending on higher orders, the momentum compaction factor only has a small impact on the calculated δ. Figure 6.4 shows a real-life measurement, comparing the fit of the chromaticity function with various δ, computed up to the third order of α_c.

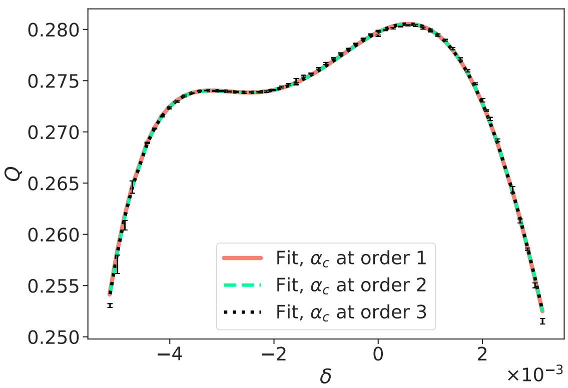

(a) Fit of the chromaticity function at the 5th order, considering the α_c expansion up to the third order.

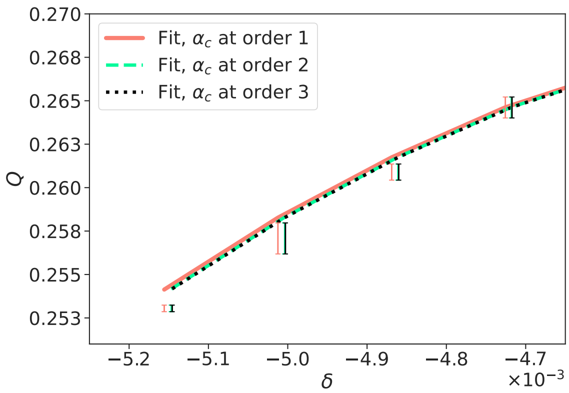

(b) Zoom on one side of the fit. The difference between the second and third order is barely noticeable.

Figure 6.4.: Fit of the chromaticity function considering several α_c orders.

The fit of the chromaticity function is barely impacted when considering the higher orders of the momentum compaction factor. The different orders of the chromaticity are collected in Table 6.1. The higher order terms of α_c can thus be neglected and are not a source of higher chromaticity orders.

	α_c order		
Chromaticity	1	2	3
$Q^{(1)}$	2.52 ± 0.03	2.53 ± 0.03	2.53 ± 0.03
$Q^{(2)}$	-3.04 ± 0.05	-3.05 ± 0.05	-3.05 ± 0.05
$Q^{(3)}$	-4.75 ± 0.03	-4.75 ± 0.03	-4.75 ± 0.03
$Q^{(4)}$	-0.33 ± 0.07	-0.32 ± 0.07	-0.32 ± 0.07
$Q^{(5)}$	2.33 ± 0.06	2.36 ± 0.06	2.36 ± 0.06

Table 6.1.: Chromaticity values obtained for the same measurement, depending on the order of the momentum compaction factor taken into account.

Momentum Offset from Orbit

During machine operation, the momentum offset, derived from the orbit, used to be logged on the servers. It was then possible to directly compute the chromaticity that way without having to use the RF and the momentum compaction factor. In 2016, measurements of the non-linear chromaticity were performed using the former method. Figure 6.5 shows a comparison of the obtained non-linear chromaticity from both methods, while Table 6.2 shows a numerical comparison. Results being similar, is it deemed that both methods are reliable to measure the non-linear chromaticity in the LHC.

	δ via RF		δ via orbit	
Plane	$Q''\,[10^3]$	$Q'''\,[10^6]$	$Q''\,[10^3]$	$Q'''\,[10^6]$
Beam 1				
X	-0.64 ± 0.01	3.00 ± 0.04	-0.62 ± 0.01	2.91 ± 0.04
Y	-0.17 ± 0.01	-2.12 ± 0.04	-0.14 ± 0.01	-2.09 ± 0.04
Beam 2				
X	-1.18 ± 0.02	2.89 ± 0.06	-1.23 ± 0.03	3.13 ± 0.11
Y	0.18 ± 0.02	-1.95 ± 0.05	0.20 ± 0.02	-2.02 ± 0.06

Table 6.2.: Comparison of the chromaticity values obtained for the same measurement via two different methods to acquire δ.

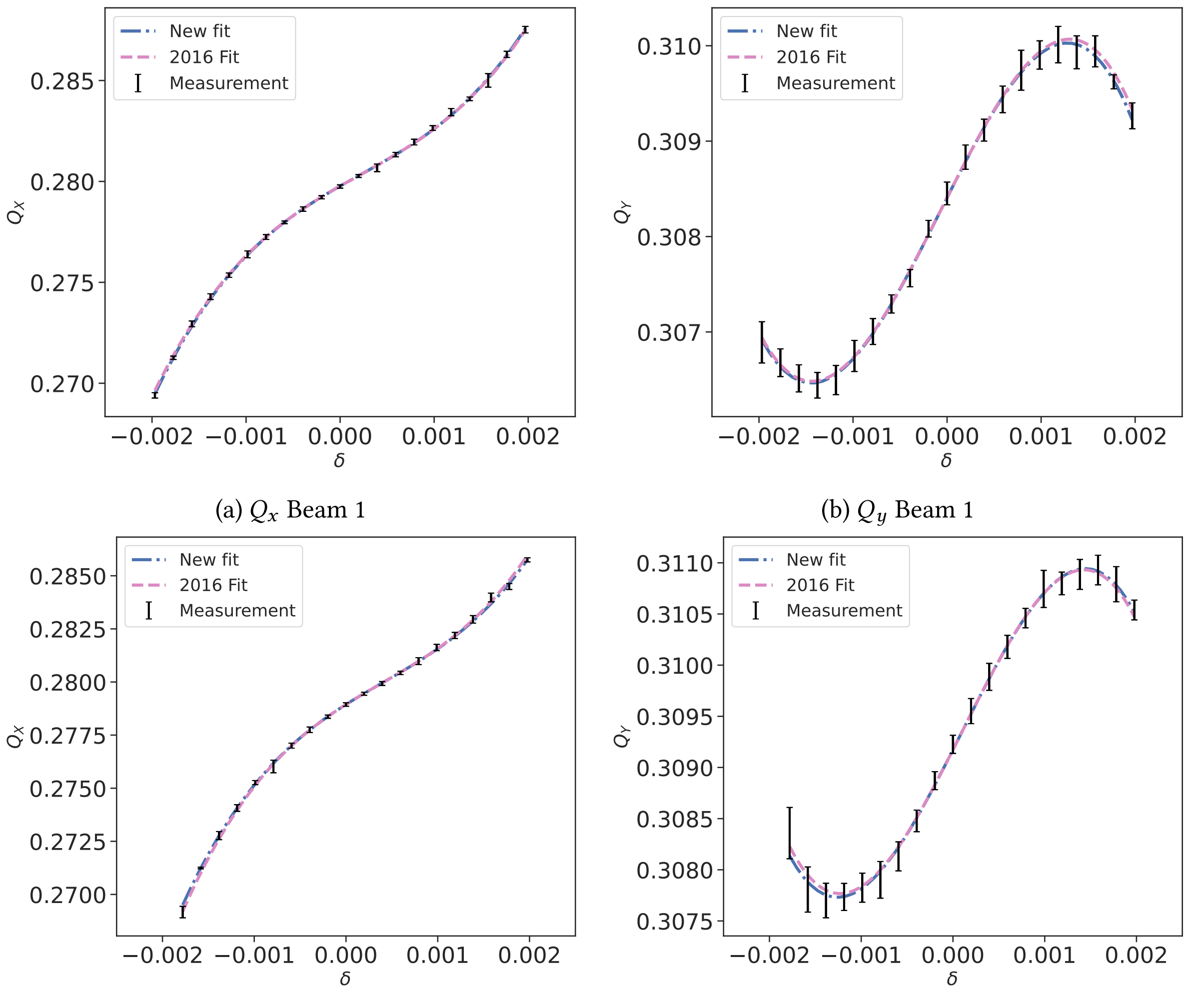

(a) Q_x Beam 1 (b) Q_y Beam 1

(c) Q_x Beam 2 (d) Q_y Beam 2

Figure 6.5.: Comparison of the non-linear chromaticity fit obtained from the computed momentum offset via the RF in 2022 and from the logged values in 2016.

6.2.2. Measurements

In order to assess the correctness of the observation of higher chromaticity orders, measurement repeatability is needed. Two measurements were thus take in 2022, with different configurations pertaining to the correction of the second and third order chromaticities Q'' and Q'''. The first one used the nominal correction strengths for octupole and decapole corrector magnets, derived from magnetic measurements, where the second one used beam-based corrections for the same elements, computed from the previous measurement. More measurements were taken during 2024's commissioning with new optics for the same reasons, to minimize the second and third order chromaticities. Three measurements were taken: with nominal corrections, after having corrected Q''' and then Q''. The introduced new optics mainly changed the powering of the triplets at the IPs and are not expected to have a considerable impact on the chromaticity.

Table 6.3 shows a summary of those measurements with their respective achieved momentum offset ranges. While the 2024 measurements achieved greater ranges than the previous ones, those were restricted during analysis to allow suitable comparisons.

Number	Year	Corrections	δ min. [$\times 10^{-3}$]	δ max. [$\times 10^{-3}$]
1	2022	Nominal	−3.15	3.01
2	2022	Q'' & Q'''	−3.15	3.72
3	2024	Nominal	−5.15	3.15
4	2024	Q'''	−3.44	4.87
5	2024	Q'' & Q'''	−3.86	4.44

Table 6.3.: Performed chromaticity measurements with their respective momentum offset ranges.

In order to stay consistent, the horizontal and vertical tunes were respectively set to $Q_x = 0.28$ and $Q_y = 0.31$ for both measurements. The linear chromaticity Q' is set to a small value, around 2, to avoid large tune shifts throughout the scan. All measurements were performed during LHC's beam commissioning, as part of the measurements and corrections performed after technical or long shutdowns.

First Observation

The first observation of higher order chromaticity was done with the octupolar and decapolar correctors *MCO* and *MCD* set to their nominal settings. Those are aimed at correcting Q'' and Q''', as previously described in Chapter 5. Results of this initial measurement are shown in Table 6.4. Lower order chromaticities such as Q' and Q'' are consistent with measurements done during the previous Run [61].

Due to the RF-scan method, the momentum offset crosses zero several times during the measurement. Negligible change in tune at this point makes it possible to determine that the tune drift through the

Plane	$Q^{(2)}\,[10^3]$	$Q^{(3)}\,[10^6]$	$Q^{(4)}\,[10^9]$	$Q^{(5)}\,[10^{12}]$
Beam 1				
X	-2.44 ± 0.02	-3.36 ± 0.04	-0.56 ± 0.02	1.20 ± 0.07
Y	0.97 ± 0.02	1.62 ± 0.05	0.15 ± 0.03	-0.88 ± 0.09
Beam 2				
X	-2.45 ± 0.03	-2.72 ± 0.08	-1.00 ± 0.05	0.15 ± 0.14
Y	0.79 ± 0.03	1.54 ± 0.06	0.24 ± 0.04	-0.74 ± 0.13

Table 6.4.: Terms of the high order chromaticity obtained during Run 3's commissioning in 2022, with nominal corrections.

measurement is of no consequence. This measurement was performed after an extended period at injection energy, where the decay of the sextupolar fields is small and not causing any change in the first order chromaticity. The fitted curve for the chromaticity function is shown in Fig. 6.6. It is clear that a higher order polynomial is beneficial to the fit, as discussed further in Section 6.2.2.

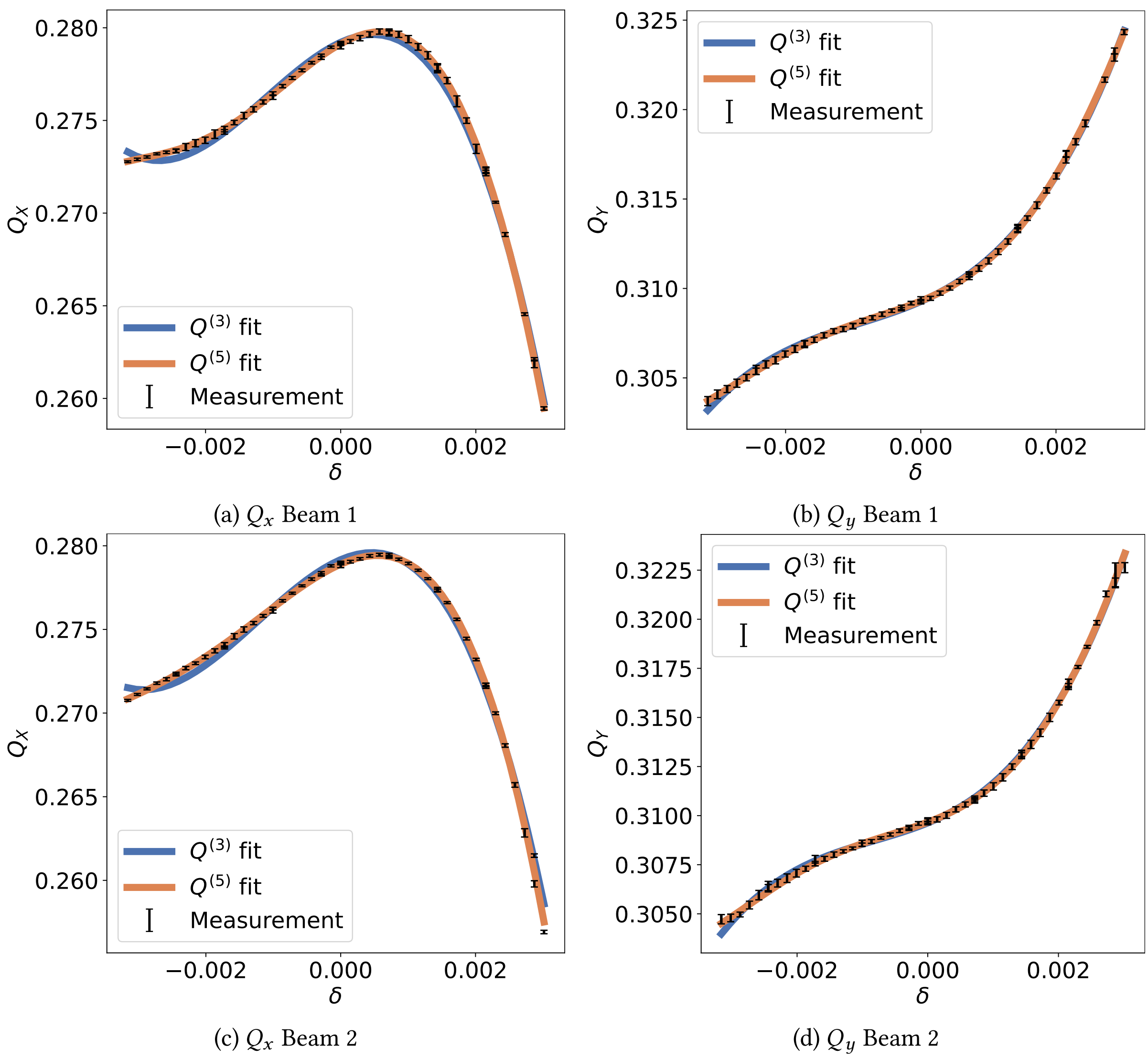

Figure 6.6.: Measurement of higher order chromaticity terms with nominal corrections used during operation. Fits are up to the third and fifth order.

Previous studies of chromaticity in the LHC only considered fits up to the third order. Expanding the fits to the fifth order increases the Q''' estimate and improves the fit quality. Accurately measuring the third order chromaticity is essential for its correction, making it important to consider the higher orders.

6

Varying Configurations

The five previously introduced measurements were performed with very different configurations for the octupolar and decapolar correctors. Table 6.5 shows the strengths applied on every circuit for each correction scheme, in 2022. The correction is called *global* as all correctors are trimmed uniformly. The 2024 corrections are similar in order of magnitude. Figure 6.7 shows the measurements and fit of some of these measurements, to highlight their differences.

Beam	$K_4\,[\mathrm{m}^{-4}]$	$K_5\,[\mathrm{m}^{-5}]$
1	+3.2973	+1610
2	+2.1716	+1618

Table 6.5.: Corrections applied on top of the nominal octupolar and decapolar correctors strengths in 2022 for the Q'' and Q''' corrections.

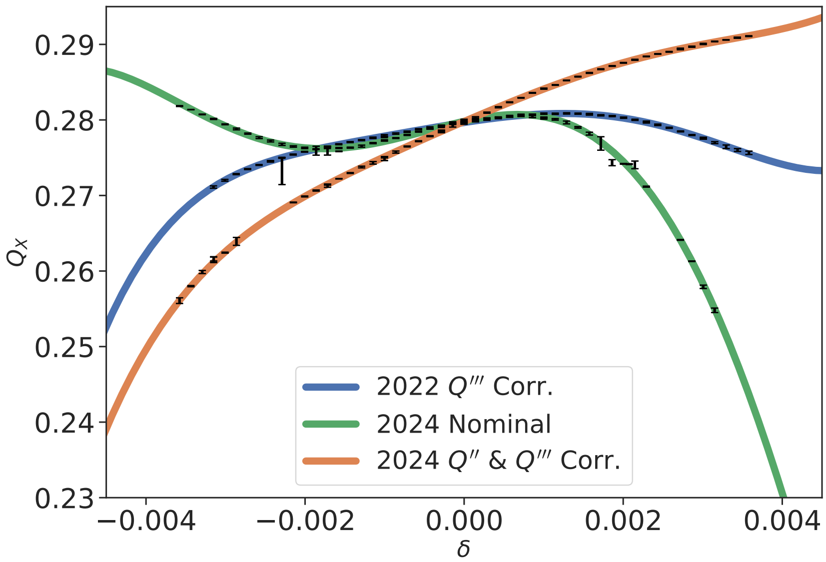

Figure 6.7.: Selection of horizontal chromaticity measurements performed with varying configurations of the octupolar and decapolar correctors for Beam 1 during the commissionings of 2022 and 2024.

A summary of the measured chromaticity orders is given in Table 6.6. The first measurement in the horizontal plane of Beam 2 showed a high correlation between $Q^{(4)}$ and $Q^{(5)}$, making the fit less reliable and is not included. The last measurement for the vertical plane experienced some tune drift, making the fit impossible and is therefore not included for both beams.

Axis	Meas.	Q''	Q'''	$Q^{(4)}$	$Q^{(5)}$
Horizontal					
Beam 1	1	-2.44 ± 0.02	-3.37 ± 0.04	-0.56 ± 0.02	1.21 ± 0.07
	2	-0.61 ± 0.01	-1.00 ± 0.03	-0.62 ± 0.02	1.19 ± 0.05
	3	-2.01 ± 0.05	-4.49 ± 0.10	-0.58 ± 0.07	1.34 ± 0.18
	4	-1.46 ± 0.03	-0.29 ± 0.06	-0.43 ± 0.04	1.09 ± 0.10
	5	-0.33 ± 0.01	-0.31 ± 0.03	-0.59 ± 0.01	0.75 ± 0.04
	Avg.			-0.56 ± 0.07	1.12 ± 0.20
Beam 2	2	-0.85 ± 0.01	-0.66 ± 0.03	-0.57 ± 0.02	1.09 ± 0.06
	3	-2.93 ± 0.05	-4.40 ± 0.08	-0.53 ± 0.08	1.66 ± 0.16
	4	-2.21 ± 0.02	-0.00 ± 0.03	-0.46 ± 0.02	1.18 ± 0.05
	5	-0.53 ± 0.02	-0.09 ± 0.03	-0.57 ± 0.02	0.98 ± 0.05
	Avg.			-0.53 ± 0.04	1.23 ± 0.26
Vertical					
Beam 1	1	0.97 ± 0.02	1.62 ± 0.05	0.15 ± 0.03	-0.88 ± 0.09
	2	-0.23 ± 0.01	0.13 ± 0.02	0.09 ± 0.02	-0.60 ± 0.03
	3	0.83 ± 0.02	1.97 ± 0.03	0.29 ± 0.02	-0.68 ± 0.05
	4	0.62 ± 0.01	-0.18 ± 0.03	0.00 ± 0.02	-0.56 ± 0.05
	Avg.			0.13 ± 0.11	-0.68 ± 0.12
Beam 2	1	0.79 ± 0.03	1.54 ± 0.06	0.24 ± 0.04	-0.74 ± 0.13
	2	-0.29 ± 0.01	0.10 ± 0.02	0.13 ± 0.02	-0.58 ± 0.04
	3	0.89 ± 0.02	2.05 ± 0.03	0.32 ± 0.03	-0.73 ± 0.06
	4	0.60 ± 0.02	-0.14 ± 0.03	0.04 ± 0.02	-0.66 ± 0.05
	Avg.			0.18 ± 0.11	-0.68 ± 0.06

Table 6.6.: Summary of the chromaticity values obtained from the measurements presented in Table 6.3.

Fit Quality

The values measured for $Q^{(4)}$ and $Q^{(5)}$ are similar across the measurements, with nominal and beam-based corrections performed with very different lower order chromaticity, and well separated in time. This reproducibility with varying configurations gives confidence that the measured values are robust. It is to be noted that one exception exists for the first measurement, the horizontal plane of beam 2 showed a high correlation between the fourth and fifth order terms, making the fit less reliable.

The reduced chi-square for the last measurement of 2022 for each fit order is detailed in Table 6.7. While adding terms to the chromaticity function is beneficial to the fit, it can be seen that the reduced chi-square does not substantially improve above the fifth order, indicating that such further orders are not warranted.

	χ^2_ν			
Plane	$Q^{(3)}$	$Q^{(4)}$	$Q^{(5)}$	$Q^{(6)}$
Beam 1				
X	17.9	12.1	1.8	1.5
Y	3.0	2.2	0.7	0.7
Beam 2				
X	17.3	7.1	1.8	1.8
Y	2.9	2.8	1.0	1.0

Table 6.7.: Reduced χ^2 values for each order of fit, taken from the second measurement of 2022, with Q'' and Q''' beam-based corrections.

6.3. Model Estimates

The model of the LHC is based on MAD-X and WISE field errors [20], containing a hundred seeds for the random errors. To compute the chromaticity, simulations are run via PTC, with various field errors.

6.3.1. Decatetrapolar Decay

6

It has been noted in the previous chapter about decapoles (see Section 5.5) that the b_5 component in the main dipoles was large at injection energy, and could explain most of the discrepancy between the measurements and simulations. Such a decay in the main dipoles also exists for the b_7 component [69], and is shown in Fig. 6.8.

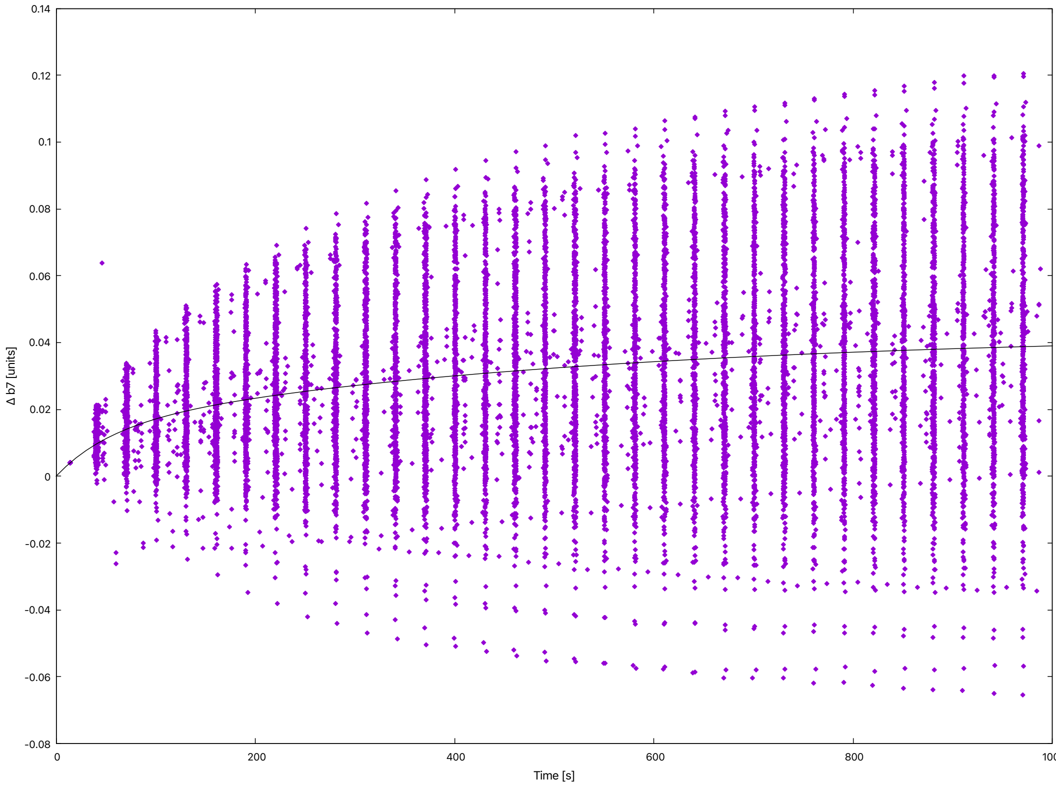

Figure 6.8.: Measured decay of the integrated decatetrapolar field in LHC's main dipoles at injection energy. The fit is shown in black [69] and settles around +0.035.

Its value is though small and settles around +0.0351 ± 0.0007. The average b_7 of the main dipoles is of 0.32 ± 0.16. The decay thus increase that value of only about 11%. Simulations done with that decay taken into account are detailed next.

6.3.2. Major contributions

Simulations with various field errors have been run to assess the contribution of individual magnet order and combinations for the fourth and firth order chromaticity. Normal and skew fields errors ranging from sextupolar (b_3) to decahexapolar (b_8) are added alone or in combination to observe which is the strongest. Quadrupolar field errors (b_2) introduce beta-beating. Coupling is introduced via skew quadrupolar correctors.

Fourth Order Chromaticity

The results from simulations strongly imply that the dodecapolar errors are the main contributors to $Q^{(4)}$, as can be seen in Fig. 6.9. Fringe fields have a negligible impact, as do skew multipoles. The most notable effect on this chromaticity order is the beta-beating, introducing a very large spread via the various error seeds. Comparing the simulation at the top with most errors added, the b_6 component alone accounts for $\approx$ 70% of it for both axes on each beam.

Fifth Order Chromaticity

It is seen that the the decatetrapolar errors are the main contributors to $Q^{(5)}$, as can be seen in Fig. 6.10. Fringe fields and skew multipoles have been found to have a negligible impact. Beta-beating and coupling are seen to increase by a small amount the chromaticity, while sextupolar errors induce a spread with the different seeds. As for the fourth order, comparing the simulation at the top with most errors added, the b_7 component alone accounts for $\approx$ 70% of it for both axes on each beam of the fifth order chromaticity.

6.3.3. Ratios

Previous simulation results are shown in Table 6.8, taking the values from the simulation including the most effects at the top of the plots. For the fourth order, the beating is not included as the large beating is not yet explained. Table 6.9 shows the ratio between the measured average and simulated chromaticities.

Plane	$Q^{(4)}$ [10^9]	$Q^{(5)}$ [10^{12}]
Beam 1		
X	-0.29 ± 0.02	0.90 ± 0.05
Y	0.04 ± 0.01	-0.46 ± 0.03
Beam 2		
X	-0.31 ± 0.02	0.92 ± 0.03
Y	0.05 ± 0.00	-0.45 ± 0.01

Table 6.8.: Simulated high order chromaticity terms via PTC at injection energy, including normal and skew sextupolar to decahexapolar field errors. Are also included beta-beating, coupling and decatetrapolar decay. For the fourth order, the values do not include beta-beating as the observed spread is not yet fully understood.

The similar ratios between planes and beams for the fifth order could indicate a systematic error not modeled. The large differences observed for the fourth order are not yet explained but the difference

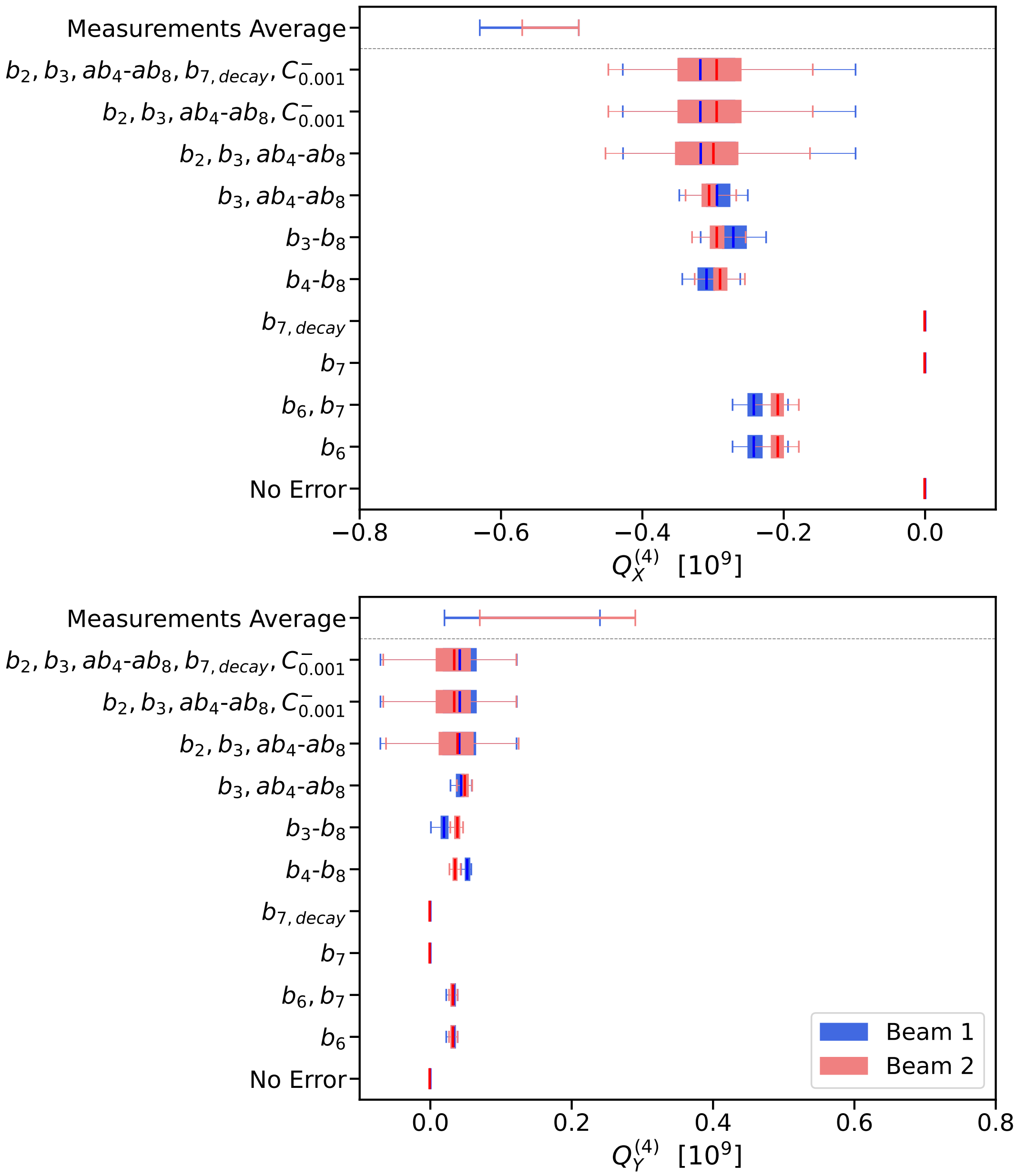

Figure 6.9.: Measured and simulated fourth order chromaticity with different multipole errors. The b_2 errors, applied on dipoles and quadrupoles, generate beta-beating. Coupling is set to a value commonly seen in operation.

between planes could be linked to a shift induced by the decapolar corrections in the vertical plane. It indeed seems that the fourth order follows a trend with the third order.

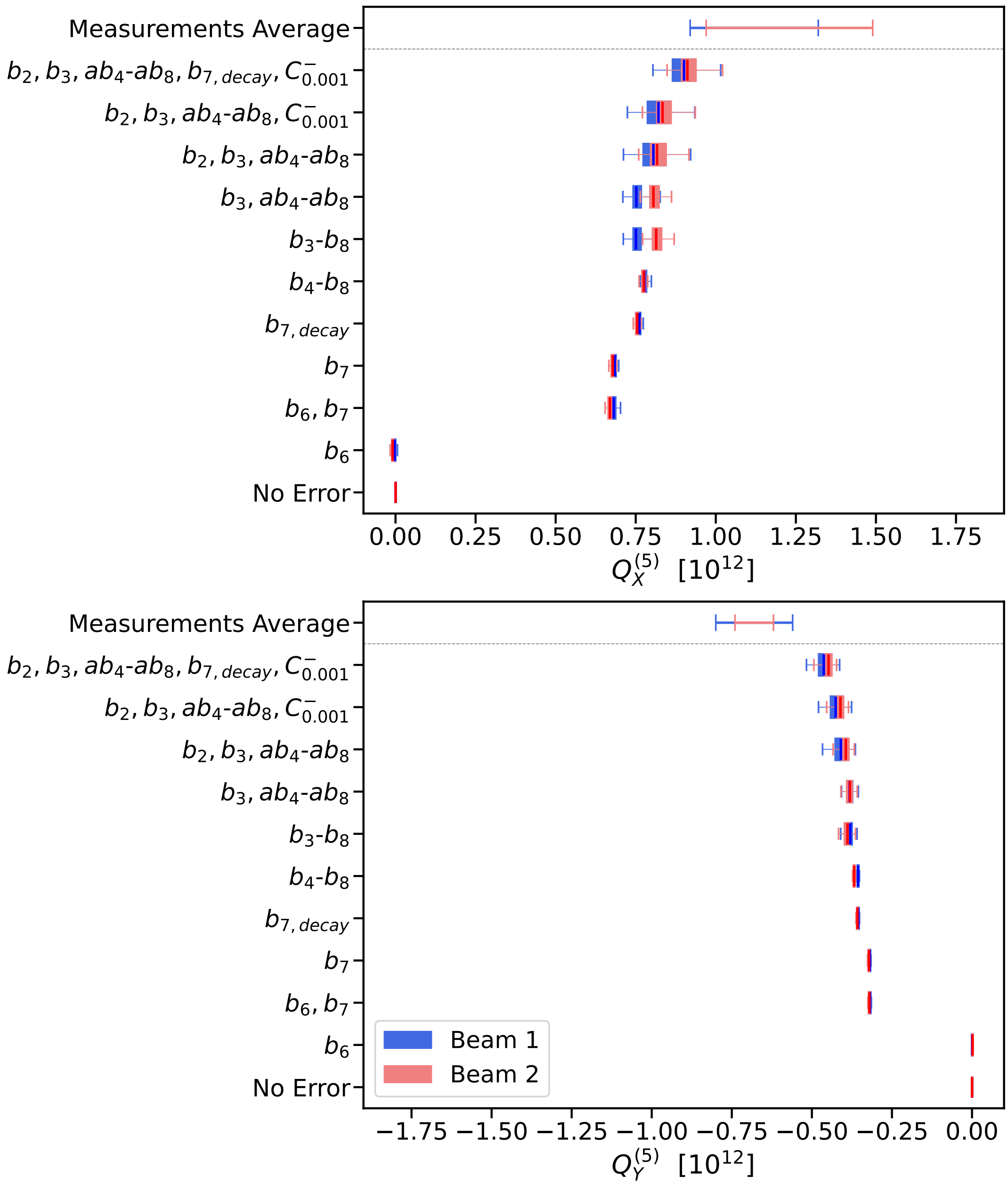

Figure 6.10.: Measured and simulated fifth order chromaticity with different multipole errors. The b_2 errors, applied on dipoles and quadrupoles, generate beta-beating. Coupling is set to a value commonly seen in operation.

Plane	$Q^{(4)}$ Ratio	$Q^{(5)}$ Ratio
Beam 1		
X	1.91 ± 0.28	1.24 ± 0.23
Y	3.00 ± 2.60	1.47 ± 0.27
Beam 2		
X	1.74 ± 0.16	1.34 ± 0.29
Y	3.70 ± 2.30	1.51 ± 0.14

Table 6.9.: Ratios of the simulated and average measured high-order chromaticity terms. The values are taken from Table 6.6 and Table 6.8.

6.4. Dodecapolar RDT

During the commissioning of 2024, resonance driving terms measurements were performed by kicking the beam at various strengths with the AC-Dipole at injection energy. Those measurements were intended to measure several RDTs with a focus on decapoles and their associated corrections. Kicks were performed using the nominal settings for octupolar and decapolar correctors, first with Q'' corrections and then with additional Q'' corrections applied. A distinct line in the vertical spectrum was observed at $5Q_y$, as shows Fig. 6.11. This line is contributed to by dodecapolar fields (see Appendix C) and is proportional to the vertical oscillation amplitude.

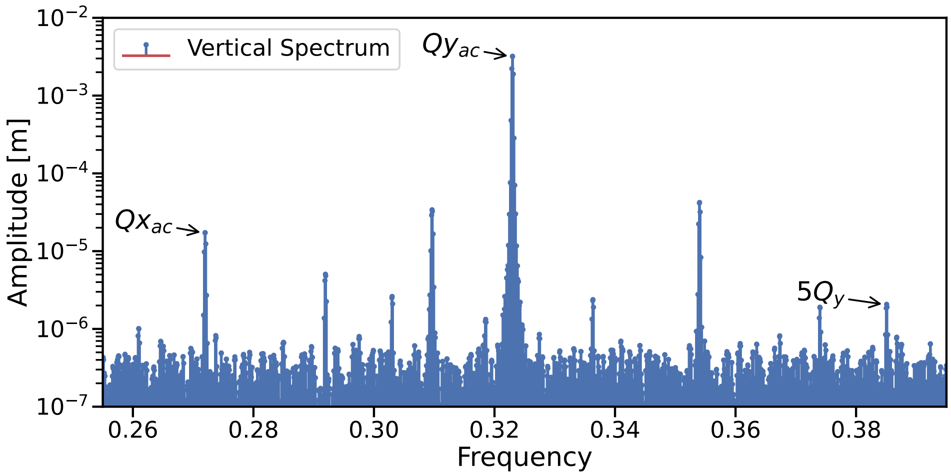

Figure 6.11.: Vertical spectrum of recorded turn-by-turn data for Beam 1 showing the tunes driven by the AC-Dipole along with a line contributed to by dodecapolar fields.

To achieve these measurements, the kick strength of the AC-Dipole was set up to 40% of its maximum, made possible by the newly introduced collimator sequence. The specific excited resonance of the observed line is the $6Q_y$, related to the RDT f_{0060}. Figure 6.12 highlights the real part of this RDT taken with nominal corrections and the repeatability of the measurement at varying kick strengths. The RMS of the amplitude of these kicks is of $3.5 \cdot 10^8$

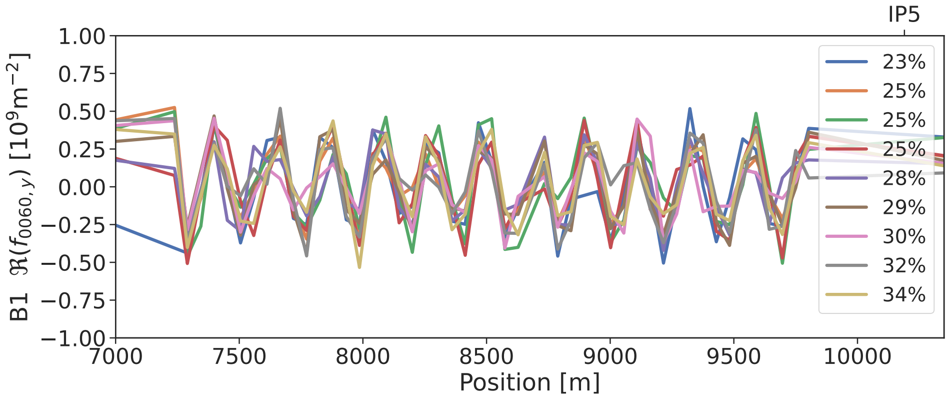

Figure 6.12.: Real part of the dodecapolar RDT f_{0060} measured with several kick strengths. The RMS amplitude is of $3.5 \cdot 10^8$.

Similar to the decapoles discussed in Section 5.6.2, the dodecapolar RDTs can be influenced by lower-order components, as shown in Table A.3. At the second-order BCH, a combination of sextupoles and decapoles, as well as a combination of octupoles, generate a decapolar-like field. At the third and fourth orders, these fields are respectively generated by a combination of sextupoles with octupoles and by sextupoles. Several tracking simulations were performed with various combinations of field errors, ranging from normal and skew sextupoles (a, b_3) to decaoctupoles (a, b_9), including as well coupling. Beta-beating is not included as b_2 errors also have an effect on the phase. Figure 6.13 shows the RMS amplitude of the RDT f_{0060} for each of these simulations. As expected from the analytical equations, the lower-order multipoles do contribute to this RDT and seem to cancel the b_6 component. It is though apparent that Beam 1 and Beam 2 do not have the same contributions from the dodecapolar errors. These seem to be compensated by other field errors for Beam 1.

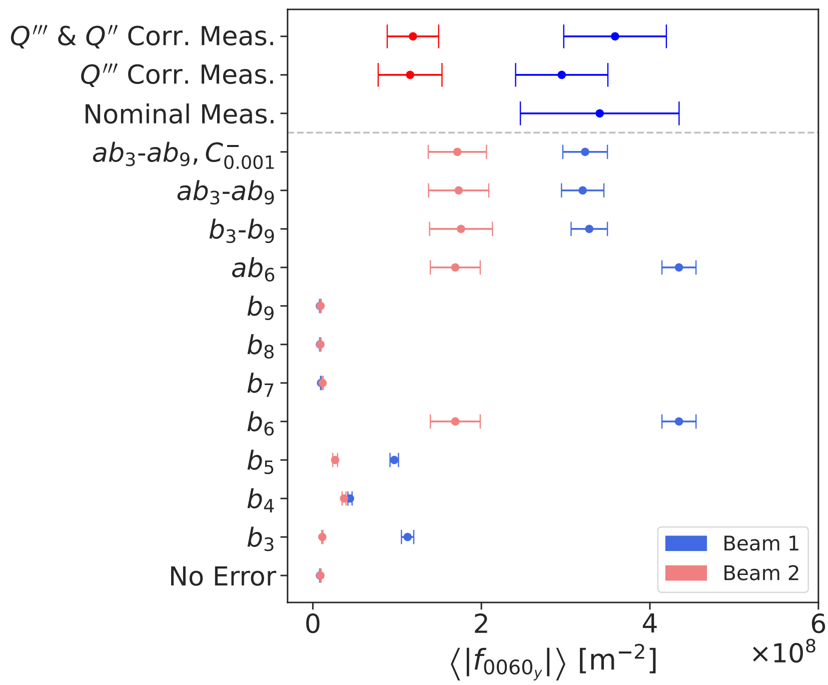

Figure 6.13.: Measured and simulated RDT f_{0060} with various normal and skew field errors. Coupling is set to a common value seen in operation.

The previously referenced measurements are also compared to these simulations. The measurement for Beam 2 with the nominal corrections could not be reliably exploited and is not included. The RDTs from these measurements are similar in amplitude, despite the different configurations for the octupolar and decapolar correctors. This suggests that, at these strength variations, the high-order correctors do not significantly affect the dodecapolar RDT f_{0060}. It is however important to note that predicting the contributions from lower-order multipoles remains difficult.

6.5. Going Further

6.5.1. Chromaticity Measurements

Limitations

So far, the momentum offset ranges of the 2024 measurements have been restricted in order to allow a comparison with the shorter ranges measurements made in 2022. The non-linearity of the chromaticity and its higher orders become very noticeable once these large ranges are reached. Figure 6.14 shows an example of such measurement for Beam 2, made with the nominal corrections, highlighting the difference between two momentum offset ranges.

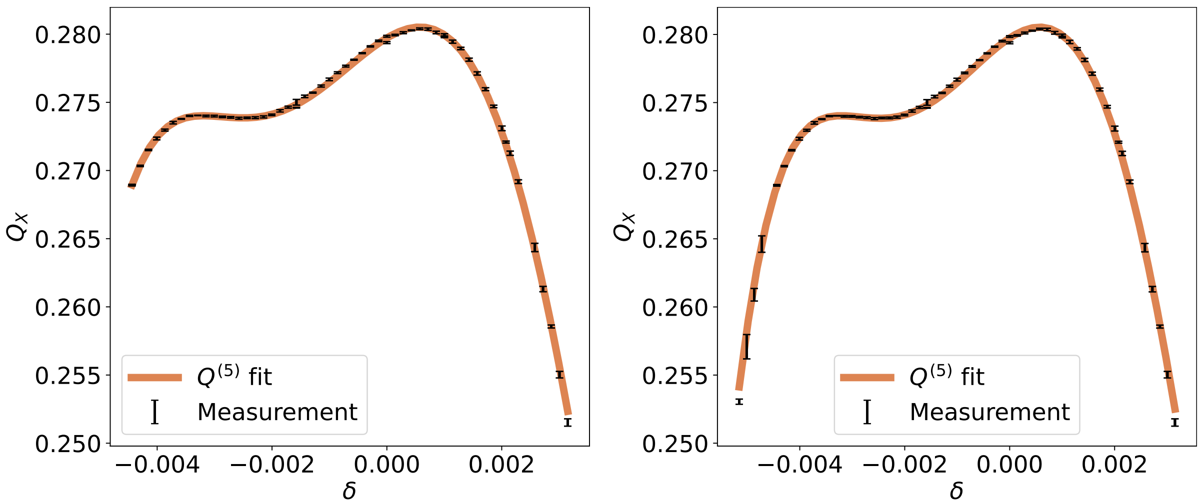

(a) Q_x Beam 2 High Range

(b) Q_y Beam 2 Full Range

Figure 6.14.: Third Beam 2 measurement of Table 6.3 with nominal corrections. A very large momentum offset range clearly highlights the non-linearity of the chromaticity function.

Plane	$Q^{(2)}$ [$\times 10^3$]	$Q^{(3)}$ [$\times 10^6$]	$Q^{(4)}$ [$\times 10^9$]	$Q^{(5)}$ [$\times 10^{12}$]
X				
Rest. Range	-2.93 ± 0.05	-4.40 ± 0.08	-0.53 ± 0.08	1.66 ± 0.16
High Range	-2.99 ± 0.05	-4.71 ± 0.03	-0.42 ± 0.07	2.23 ± 0.07
Full Range	-3.05 ± 0.05	-4.75 ± 0.03	-0.33 ± 0.07	2.34 ± 0.06
Y				
Rest. Range	0.89 ± 0.02	2.05 ± 0.03	0.32 ± 0.03	-0.73 ± 0.06
High Range	0.87 ± 0.02	2.07 ± 0.02	0.36 ± 0.03	-0.77 ± 0.03
Full Range	0.70 ± 0.04	1.83 ± 0.03	0.64 ± 0.06	-0.32 ± 0.05

Table 6.10.: Variance of the chromaticity values depending on the considered momentum offset range. All ranges have an upper bound of 3.2×10^{-3}. The lower bounds are, in order of appearance: -3.5, -4.5, -5.2.

Table 6.10 shows the obtained chromaticity values for varying ranges. From this table, it can be noted that increasing the range mainly changes the estimate for $Q_x^{(5)}$. Measurements over such a wide range are not yet fully understood, as other non-linear effects can induce a detuning. For example, transverse impedances leads to a defocusing effect whose magnitude increases with the orbit offset [70, 71]. Some other performed measurements with wide ranges in 2024 could not be fitted with a chromaticity function, despite including higher orders. It is deemed that restricting the ranges is beneficial to the fit estimates, until further investigation of these effects.

Higher Orders

The fifth measurement in Table 6.3 covered a range of $[-4.0 \cdot 10^{-3}, 4.5 \cdot 10^{-3}]$, which is among the widest ever measured. It is clear from Fig. 6.15 that a chromaticity function including the sixth order provides a better fit to the data. However, no additional observations were made for this order, and considering the previously mentioned limitations, this measurement may not be entirely robust. Further studies could address these limitations to more accurately characterize the decahexapolar fields of the LHC at injection energy.

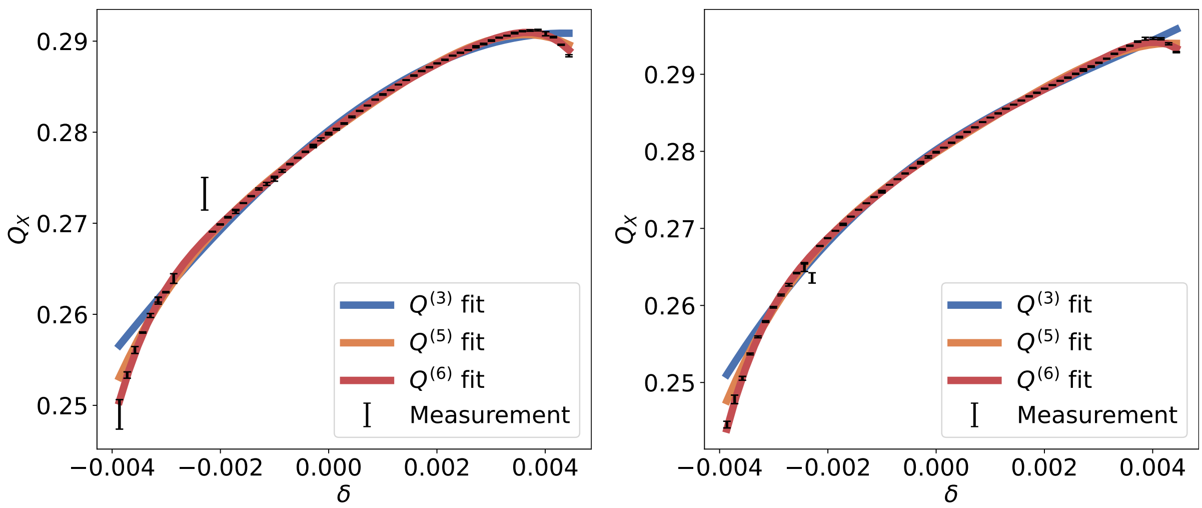

(a) Q_x Beam 1

(b) Q_x Beam 2

Figure 6.15.: Fifth measurement of Table 6.3 with Q'' and Q''' corrections. A possible sixth chromaticity order can be seen.

6.5.2. Dodecapolar RDTs

The measured RDT f_{0060} seems to be on par with the model but it is crucial to note that RDTs of high-order multipoles are contributed to by the lower orders. Notably here, changes of chromaticity (linear and non-linear), landau octupoles and amplitude detuning corrections will affect the RDT f_{0060}. Such effects stack up quickly and make an accurate model of the machine hard to achieve. Regarding the chromaticity, there exists a discrepancy between the measured $Q^{(4)}$ and the model. Further studies could be aimed at trimming lower order circuits such as decapolar correctors and observing the impact on both the chromaticity and the RDT. The decay of the b_6 component of the quadrupoles could also play a role.

Since dodecapolar correctors are only located at the IPs, within a dispersion-suppressed zone, they can only influence the RDTs, not the chromaticity. Without crossing angles, and therefore no feed-down to amplitude detuning, these correctors could be individually trimmed to observe changes in lifetime and RDT, which could potentially lead to corrections is deemed useful.

6.6. Summary

This chapter explores the measurement and analysis of higher-order fields in the LHC at injection energy, with a focus on dodecapolar and decatetrapolar fields. Leveraging a newly implemented collimation setup and a custom post-processing technique, these higher-order fields have been successfully observed.

Chromaticity measurements were conducted with varying momentum offsets, revealing fourth and fifth-order terms $Q^{(4)}$ and $Q^{(5)}$. The repeated measurements consistently identified these higher-order terms, demonstrating their robustness. Measuring across such extended ranges and including higher orders is essential for accurately characterizing the lower orders. The analysis also shows that the primary contributors to these terms are dodecapolar and decatetrapolar fields, which originate from fields errors of the main dipoles.

For the first time, the dodecapolar Resonance Driving Term f_{0060} was measured. This measurement, repeated for both beams at different configurations, shows a good agreement with the model.

It is then concluded that further investigations could be conducted to address limitations in the measurement range of the chromaticity function and to refine estimates of higher-order chromaticity terms. Dodecapolar RDT studies could benefit from lifetime measurements accompanied by trims of the relevant correctors situated in the Interaction Regions (IRs). Additionally, investigating the impact of lower-order multipoles on the RDT would be valuable. Overall, gaining a thorough understanding of the higher-order field errors is essential for optimizing the LHC's performance.

7 Conclusions

This thesis has provided a comprehensive analysis of higher-order magnetic fields in the Large Hadron Collider (LHC) and their significant impact on beam dynamics and stability. The research underscores the critical importance of understanding and correcting skew octupolar, decapolar, dodecapolar, and decatetrapolar fields to ensure optimal performance of the LHC, particularly at injection energy.

The investigation into skew octupolar fields made use a response matrix approach for correcting resonance driving using corrector magnets. The research further identified the interplay between Landau octupoles and skew octupolar RDTs, highlighting the essential role of accurate coupling modeling.

The study of decapolar fields addressed discrepancies between measured and predicted third-order chromaticity, pinpointing the decay of decapolar components in the main dipoles as a key factor. The development of new correction strategies led to tangible improvements in beam lifetime and stability, demonstrating the effectiveness of these approaches.

Finally, the thesis introduced innovative measurement techniques for higher-order chromaticity terms, revealing the contribution of dodecapolar and decatetrapolar fields errors. Furthermore, first measurements of dodecapolar resonance driving terms were made. These findings reinforce the need for further exploration of higher-order fields to enhance the LHC's operational efficiency.

Overall, the research provides valuable insights into the complex interplay of magnetic fields within the LHC and lays the groundwork for future advancements in collider performance and stability.

List of Figures

List of Tables

Appendices

A Hamiltonians and Transfer Maps

This appendix is intended to gather and explicit the Hamiltonians of the elements used in this thesis. Non-linear transfer maps are also described for some of those elements from the first to the second order.

A.1. Hamiltonians of Elements

The Hamiltonian of a *multipole* is the following [29, 31, 72]:

$$H = \Re\left[\sum_{n>1}(K_n + iJ_n)\frac{(x+iy)^n}{n!}\right]. \tag{A.1}$$

From this, normal and skew fields can be separated:

$$\begin{aligned} N_n &= \frac{1}{n!}K_n\Re\left[(x+iy)^n\right] \\ S_n &= -\frac{1}{n!}J_n\Im\left[(x+iy)^n\right], \end{aligned} \tag{A.2}$$

where K and J are the normalized strength of the multipole and x, y the transverse coordinates. Table A.1 explicits the normal and skew Hamiltonians of multipoles up to order 8.

Name	Order	Normal and Skew Hamiltonians
Drift	-	$H = \frac{1}{2}(p_x^2 + p_y^2)$
Quadrupole	2	$N_2 = \frac{1}{2!}K_2\left(x^2 - y^2\right)$ $S_2 = -J_2xy$
Sextupole	3	$N_3 = \frac{1}{3!}K_3\left(x^3 - 3xy^2\right)$ $S_3 = -\frac{1}{3!}J_3 \cdot \left(3x^2y - y^3\right)$
Octupole	4	$N_4 = \frac{1}{4!}K_4\left(x^4 - 6x^2y^2 + y^4\right)$ $S_4 = -\frac{1}{4!}J_4 \cdot \left(4x^3y - 4xy^3\right)$
Decapole	5	$N_5 = \frac{1}{5!}K_5\left(x^5 - 10x^3y^2 + 5xy^4\right)$ $S_5 = -\frac{1}{5!}J_5 \cdot \left(5x^4y - 10x^2y^3 + y^5\right)$
Dodecapole	6	$N_6 = \frac{1}{6!}K_6\left(x^6 - 15x^4y^2 + 15x^2y^4 - y^6\right)$ $S_6 = -\frac{1}{6!}J_6 \cdot \left(6x^5y - 20x^3y^3 + 6xy^5\right)$
Decatetrapole	7	$N_7 = \frac{1}{7!}K_7\left(x^7 - 21x^5y^2 + 35x^3y^4 - 7xy^6\right)$ $S_7 = -\frac{1}{7!}J_7 \cdot \left(7x^6y - 35x^4y^3 + 21x^2y^5 - y^7\right)$
Decahexapole	8	$N_8 = \frac{1}{8!}K_8\left(x^8 - 28x^6y^2 + 70x^4y^4 - 28x^2y^6 + y^8\right)$ $S_8 = -\frac{1}{8!}J_8 \cdot \left(8x^7y - 56x^5y^3 + 56x^3y^5 - 8xy^7\right)$

Table A.1.: Normal and skew Hamiltonians of multipoles up to order 8.

A.2. Transfer Maps

This sections goes more in depth regarding the derivation of the examples of transfer maps introduced in Section 2.4.

As a reminder, the BCH of two elements up to order 3 is given below,

$$Z = \underbrace{H_2 + H_1}_{\text{First order}} + \underbrace{\frac{[H_2, H_1]}{2}}_{\text{Second order}} + \underbrace{\frac{[H_2, [H_2, H_1]]}{12} - \frac{[H_1, [H_2, H_1]]}{12}}_{\text{Third order}}. \tag{A.3}$$

A.2.1. Generic Effective Hamiltonian of Two Elements

In order not to have to derive every combination of multipoles, a generic approach can be taken. Two elements of orders n and m can indeed be combined together via the BCH. Their hamiltonians is thus the one from Eq. (A.1) with orders m and n. A drift is put in between the two multipoles to change the coordinates. This results in non-zero Poisson brackets as the momentum is propagated,

$$[H_2, H_1] \longrightarrow [H_2, D \cdot H_1]. \tag{A.4}$$

Higher orders will arise with derivations when applying the Poisson brackets. Those orders can be found by counting the number of Poisson brackets, and which operators are implicated. A Poisson bracket implicating H_2 will increase the resulting order by m, and likewise for H_1 and n. The resulting order is then decreased by the number of poisson brackets times 2. Equation (A.5) gives how this can be calculated when considering the written form of the Poisson brackets (eg. $[H_2, [H_2, H_1]]$).

$$\text{resulting order} = \text{count}(\text{"}H_2\text{"}) \cdot m + \text{count}(\text{"}H_1\text{"}) \cdot n - 2 \cdot \text{count}(\text{"[")} \tag{A.5}$$

Although this formula is quite helpful, it is not trivial to compute which orders will arise from each BCH order. Indeed, not all combinations of H_1 and H_2 appear, as explained in details in [27]. Table A.2 shows the Poisson brackets corresponding to each order of the BCH, up to order 6, along with the resulting multipole order. To keep the table readable, Poisson Brackets are not shown above that order, as duplicates of resulting orders become quite frequent. Similarly, Table A.3 shows how fields can be generated depending on the orders of multipoles and that of the BCH.

BCH Order	Poisson Brackets	Resulting Order
1	A	m
	B	n
2	$\frac{[A,B]}{2}$	$m+n-2$
3	$-\frac{[B,[A,B]]}{12}$	$m+2n-4$
	$\frac{[A,[A,B]]}{12}$	$2m+n-4$
4	$-\frac{[B,[A,[A,B]]]}{24}$	$2m+2n-6$
5	$-\frac{[A,[B,[A,[A,B]]]]}{120}$	$3m+2n-8$
	$-\frac{[B,[A,[A,[A,B]]]]}{180}$	$3m+2n-8$
	$-\frac{[A,[B,[B,[A,B]]]]}{360}$	$2m+3n-8$
	$-\frac{[A,[A,[A,[A,B]]]]}{720}$	$4m+n-8$
	$\frac{[B,[B,[A,[A,B]]]]}{180}$	$2m+3n-8$
	$\frac{[B,[B,[B,[A,B]]]]}{720}$	$m+4n-8$
6	$-\frac{[A,[A,[B,[B,[A,B]]]]]}{240}$	$3m+3n-10$
	$\frac{[A,[B,[B,[A,[A,B]]]]]}{240}$	$3m+3n-10$
	$\frac{[B,[B,[A,[A,[A,B]]]]]}{360}$	$3m+3n-10$
	$\frac{[A,[B,[B,[B,[A,B]]]]]}{720}$	$2m+4n-10$
	$\frac{[B,[A,[A,[A,[A,B]]]]]}{1440}$	$4m+2n-10$
	$\frac{[B,[B,[B,[A,[A,B]]]]]}{1440}$	$2m+4n-10$
7	$\cdots$	$2m+5n-12$
		$m+6n-12$
		$3m+4n-12$
		$5m+2n-12$
		$6m+n-12$
		$4m+3n-12$

Table A.2.: Resulting multipole orders arising from the Poisson brackets of a given BCH order for two multipoles A and B of order m and n. At order 7, the Poisson brackets are not given as duplicates grow the list significantly.

	BCH Order					
Field	1	2	3	4	5	6
3	H_3					
4	H_4	$(H_3)^2$				
5	H_5	H_3H_4	$(H_3)^3$			
6	H_6	H_3H_5, $(H_4)^2$	$(H_3)^2H_4$	$(H_3)^4$		
7	H_7	H_3H_6, H_4H_5	$(H_3)^2H_5$, $H_3(H_4)^2$		$(H_3)^5$	
8	H_8	$(H_5)^2$, H_3H_7, H_4H_6	$(H_3)^2H_6$, $(H_4)^3$	$(H_3)^2(H_4)^2$	$(H_3)^4H_4$	$(H_3)^6$
9	H_9	H_4H_7, H_3H_8, H_5H_6	$(H_3)^2H_7$, $(H_4)^2H_5$, $H_3(H_5)^2$		$(H_3)^3(H_4)^2$, $(H_3)^4H_5$	
10	H_{10}	H_4H_8, H_5H_7, H_3H_9, $(H_6)^2$	$(H_3)^2H_8$, $H_4(H_5)^2$, $(H_4)^2H_6$	$(H_4)^4$, $(H_3)^2(H_5)^2$	$(H_3)^2(H_4)^3$, $(H_3)^4H_6$	$(H_3)^4(H_4)^2$
11	H_{11}	H_4H_9, H_3H_{10}, H_6H_7, H_5H_8	$(H_4)^2H_7$, $H_3(H_6)^2$, $(H_5)^3$, $(H_3)^2H_9$		$(H_3)^4H_7$, $H_3(H_4)^4$, $(H_3)^3(H_5)^2$	$(H_3)^3(H_4)^3$
12	H_{12}	H_6H_8, $(H_7)^2$, H_5H_9, H_3H_{11}, H_4H_{10}	$H_4(H_6)^2$, $(H_4)^2H_8$, $(H_5)^2H_6$, $(H_3)^2H_{10}$	$(H_3)^2(H_6)^2$, $(H_4)^2(H_5)^2$	$(H_3)^4H_8$, $(H_4)^5$	$(H_3)^4(H_5)^2$, $(H_3)^2(H_4)^4$

Table A.3.: Correspondence of a combination of multipoles from a BCH order to multipole-like fields. The exponents indicate the order of the BCH for individual components.

A.2.2. Transfer Map of Two Sextupoles

The transfer map of two sextupoles H_1 and H_2 of strength K_1 and K_2, separated by a drift to introduce a change of coordinates in H_1 is the following,

$$\mathcal{M} = e^{:Z:} = e^{:H_2:} \cdot e^{D:H_1:}, \tag{A.6}$$

After such application of the drift on H_1, the two hamiltonians read,

$$\begin{aligned} H_1 &= \frac{1}{3!} K_1 L_1 \left((L_D p_x + x)^3 - 3\,(L_D p_x + x)\left(L_D p_y + y\right)^2 \right) \\ H_2 &= \frac{1}{3!} K_2 L_2 \left(x^3 - 3xy^2\right). \end{aligned} \tag{A.7}$$

Below are detailed each term of the BCH. Each term should be added together in order to obtain the whole effective Hamiltonian Z.

First Order

$$\left.\begin{aligned} &K_1 L_1 L_D \begin{pmatrix} \dfrac{L_D^2 p_x^3}{6} - \dfrac{L_D^2 p_x p_y^2}{2} + \dfrac{L_D p_x^2 x}{2} - L_D p_x p_y y \\ - \dfrac{L_D p_y^2 x}{2} + \dfrac{p_x x^2}{2} - \dfrac{p_x y^2}{2} - p_y x y \end{pmatrix} \\ &+ K_1 L_1 \left(\frac{x^3}{6} - \frac{xy^2}{2}\right) + K_2 L_2 \left(\frac{x^3}{6} - \frac{xy^2}{2}\right) \end{aligned}\right\}\text{sextupolar} \tag{A.8}$$

Second Order

$$K_1 K_2 L_1 L_2 L_D \left.\begin{pmatrix} \dfrac{L_D^2 p_x^2 x^2}{8} - \dfrac{L_D^2 p_x^2 y^2}{8} + \dfrac{L_D^2 p_x p_y x y}{2} - \dfrac{L_D^2 p_y^2 x^2}{8} \\ + \dfrac{L_D^2 p_y^2 y^2}{8} + \dfrac{L_D p_x x^3}{4} + \dfrac{L_D p_x x y^2}{4} + \dfrac{L_D p_y x^2 y}{4} \\ + \dfrac{L_D p_y y^3}{4} + \dfrac{x^4}{8} + \dfrac{x^2 y^2}{4} + \dfrac{y^4}{8} \end{pmatrix}\right\}\text{octupolar-like} \tag{A.9}$$

A

Third Order

$$\left.\begin{aligned} &K_1^2K_2L_1^2L_2L_D\left(\begin{aligned}&\frac{L_D^5p_x^4x}{48}+\frac{L_D^5p_x^3p_yy}{12}-\frac{L_D^5p_x^2p_y^2x}{8}-\frac{L_D^5p_xp_y^3y}{12}\\&+\frac{L_D^5p_y^4x}{48}+\frac{L_D^4p_x^3x^2}{12}+\frac{L_D^4p_x^3y^2}{12}-\frac{L_D^4p_xp_y^2x^2}{4}\\&-\frac{L_D^4p_xp_y^2y^2}{4}+\frac{L_D^3p_x^2x^3}{8}+\frac{L_D^3p_x^2xy^2}{8}-\frac{L_D^3p_xp_yx^2y}{4}\\&-\frac{L_D^3p_xp_yy^3}{4}-\frac{L_D^3p_y^2x^3}{8}-\frac{L_D^3p_y^2xy^2}{8}+\frac{L_D^2p_xx^4}{12}\\&-\frac{L_D^2p_xy^4}{12}-\frac{L_D^2p_yx^3y}{6}-\frac{L_D^2p_yxy^3}{6}+\frac{L_Dx^5}{48}\\&-\frac{L_Dx^3y^2}{24}-\frac{L_Dxy^4}{16}\end{aligned}\right)\\ &+K_1K_2^2L_1L_2^2L_D\left(\begin{aligned}&\frac{L_D^2p_xx^4}{48}-\frac{L_D^2p_xx^2y^2}{8}+\frac{L_D^2p_xy^4}{48}+\frac{L_D^2p_yx^3y}{12}\\&-\frac{L_D^2p_yxy^3}{12}+\frac{L_Dx^5}{48}-\frac{L_Dx^3y^2}{24}-\frac{L_Dxy^4}{16}\end{aligned}\right)\end{aligned}\right\}\text{decapolar-like} \tag{A.10}$$

A.2.3. Transfer Map of a Sextupole and Octupole

The transfer map of a sextupole H_1 and octupole H_2 of strength K_1 and K_2, separated by a drift like in the previous example is given by

$$\mathcal{M} = e^{:Z:} = e^{:H_2:}\cdot e^{D:H_1:} \tag{A.11}$$

with H_1 and H_2 having as final expressions,

$$\begin{aligned} H_1 &= \frac{1}{3!}K_{3,h1}L_1\left((L_Dp_x+x)^3-3\,(L_Dp_x+x)\left(L_Dp_y+y\right)^2\right)\\ H_2 &= \frac{1}{4!}K_2L_2\left(x^4-6x^2y^2+y^4\right). \end{aligned} \tag{A.12}$$

The first two orders of the BCH of those two elements is given below.

First Order

$$\begin{aligned} &K_3\left(\begin{aligned}&\frac{L_D^3p_x^3}{6}-\frac{L_D^3p_xp_y^2}{2}+\frac{L_D^2p_x^2x}{2}-L_D^2p_xp_yy-\frac{L_D^2p_y^2x}{2}\\&+\frac{L_Dp_xx^2}{2}-\frac{L_Dp_xy^2}{2}-L_Dp_yxy+\frac{x^3}{6}-\frac{xy^2}{2}\end{aligned}\right)\Bigg\}\text{sextupolar}\\ &+K_4\left(\frac{x^4}{24}-\frac{x^2y^2}{4}+\frac{y^4}{24}\right)\Big\}\text{octupolar} \end{aligned} \tag{A.13}$$

A

Second Order

$$K_3K_4L_D\left.\left(\begin{array}{l}\frac{L_D^2p_x^2x^3}{24}-\frac{L_D^2p_x^2xy^2}{8}+\frac{L_D^2p_xp_yx^2y}{4}-\frac{L_D^2p_xp_yy^3}{12}\\-\frac{L_D^2p_y^2x^3}{24}+\frac{L_D^2p_y^2xy^2}{8}+\frac{L_Dp_xx^4}{12}-\frac{L_Dp_xy^4}{12}\\+\frac{L_Dp_yx^3y}{6}+\frac{L_Dp_yxy^3}{6}+\frac{x^5}{24}+\frac{x^3y^2}{12}+\frac{xy^4}{24}\end{array}\right)\right\}\text{ decapolar-like} \tag{A.14}$$

A.2.4. Transfer Map of a Skew Quadrupole and Octupole

The transfer map of a skew quadrupole H_1 and octupole H_2 of strength K_1 and K_2, separated by a drift like in the previous examples is given by

$$\mathcal{M} = e^{:Z:} = e^{:H_2:}\cdot e^{D:H_1:} \tag{A.15}$$

with H_1 and H_2 having as final expressions,

$$\begin{aligned}H_1 &= -J_1L_1\left(L_Dp_x+x\right)\left(L_Dp_y+y\right)\\H_2 &= \frac{1}{4!}K_2L_2\left(x^4-6x^2y^2+y^4\right).\end{aligned} \tag{A.16}$$

The first two orders of the BCH of those two elements is given below.

First Order

$$\begin{aligned}&J_1L_1\left(-L_D^2p_xp_y-L_Dp_xy-L_Dp_yx-xy\right)\Big\}\text{ skew quadrupolar}\\&+K_2L_2\left.\left(\frac{x^4}{24}-\frac{x^2y^2}{4}+\frac{y^4}{24}\right)\right\}\text{ octupolar}\end{aligned} \tag{A.17}$$

Second Order

$$J_1K_2L_1L_2L_D\left.\left(\begin{array}{l}\frac{L_Dp_xx^2y}{4}-\frac{L_Dp_xy^3}{12}-\frac{L_Dp_yx^3}{12}\\+\frac{L_Dp_yxy^2}{4}+\frac{x^3y}{6}+\frac{xy^3}{6}\end{array}\right)\right\}\text{ skew octupolar-like} \tag{A.18}$$

B

Chromatic Amplitude Detuning

B

This appendix details the derivations of chromatic amplitude detuning from sextupoles up to dodecapoles. *Chromatic Amplitude Detuning*, being detuning coming from both the action and the momentum offset, only starts appearing with decapoles. Below that order, only amplitude detuning and chromaticity can be observed. As those are part of the derivations, they will also be detailed here.

B.1. Derivations

In this section, the terms of the chromatic amplitude detuning are given up to dodecapoles. Derivations are given only for sextupoles and octupoles, as the process remains fairly similar for higher orders. Vertical offsets will be neglected, as horizontal dispersion is dominant. The reasoning remains the same.

Up to the third order, the expression of the Taylor expansion of the Chromatic Amplitude Detuning around ϵ_x, ϵ_y and δ, for a tune Q_z, $z \in \{x, y\}$ reads:

B

$$
\begin{aligned}
Q_z(\epsilon_x, \epsilon_y, \delta) = Q_{z0} &+ \left[\frac{\partial Q_z}{\partial \epsilon_x}\epsilon_x + \frac{\partial Q_z}{\partial \epsilon_y}\epsilon_y + \frac{\partial Q_z}{\partial \delta}\,\delta \right] \\
&+ \frac{1}{2!}\left[\frac{\partial^2 Q_z}{\partial \epsilon_x^2}\epsilon_x^2 + \frac{\partial^2 Q_z}{\partial \epsilon_y^2}\epsilon_y^2 + \frac{\partial^2 Q_z}{\partial \delta^2}\,\delta^2 \right. \\
&\qquad \left. + 2\frac{\partial^2 Q_z}{\partial \epsilon_x \partial \epsilon_y}\epsilon_x\epsilon_y + 2\frac{\partial^2 Q_z}{\partial \epsilon_x \partial \delta}\epsilon_x\delta + 2\frac{\partial^2 Q_z}{\partial \delta \partial \epsilon_y}\delta\epsilon_y \right] \\
&+ \frac{1}{3!}\left[\frac{\partial^3 Q_z}{\partial \delta^3}\,\delta^3 + \frac{\partial^3 Q_z}{\partial \epsilon_x^3}\epsilon_x^3 + \frac{\partial^3 Q_z}{\partial \epsilon_y^3}\epsilon_y^3 \right. \\
&\qquad + 3\frac{\partial^3 Q_z}{\partial \epsilon_x \partial \delta^2}\delta^2\epsilon_x + 3\frac{\partial^3 Q_z}{\partial \epsilon_y \partial \delta^2}\delta^2\epsilon_y + 3\frac{\partial^3 Q_z}{\partial \epsilon_x^2 \partial \delta}\delta\epsilon_x^2 \\
&\qquad + 3\frac{\partial^3 Q_z}{\partial \epsilon_y^2 \partial \delta}\delta\epsilon_y^2 + 3\frac{\partial^3 Q_z}{\partial \epsilon_y \partial \epsilon_x^2}\epsilon_x^2\epsilon_y + 3\frac{\partial^3 Q_z}{\partial \epsilon_y^2 \partial \epsilon_x}\epsilon_x\epsilon_y^2 \\
&\qquad \left. + 6\frac{\partial^3 Q_z}{\partial \epsilon_y \partial \epsilon_x \partial \delta}\delta\epsilon_x\epsilon_y \right] + \cdots
\end{aligned}
\tag{B.1}
$$

B.1.1. Principle

From [32], the detuning caused by a magnet of length L can be described by its hamiltonian with

$$
\Delta Q_z = \frac{1}{2\pi}\int_L \frac{\partial \langle H \rangle}{\partial J_z}\,\mathrm{d}s. \tag{B.2}
$$

The usual variables x and y of Eq. (2.12) can be replaced by *action-angle* variables to introduce the action:

$$
\begin{aligned}
x &\longrightarrow \sqrt{2J_x\beta_x}\cos\phi_x \\
y &\longrightarrow \sqrt{2J_y\beta_y}\cos\phi_x
\end{aligned}
\tag{B.3}
$$

A momentum dependence can be introduced for a particle with a different orbit (Δz) [73] via dispersion. Combined with Eq. (B.3), a dependence on all required components is achieved:

$$
\begin{aligned}
x + \Delta x &\longrightarrow \sqrt{2J_x\beta_x}\cos\phi_x + D_x\delta \\
y + \Delta y &\longrightarrow \sqrt{2J_y\beta_y}\cos\phi_y + D_y\delta
\end{aligned}
\tag{B.4}
$$

After averaging over the phase variable, all that is left is to compute the partial derivatives.

B.1.2. Sextupole

Taken from Table A.1, the normal field of a sextupole is $N_3 = \frac{1}{3!}K_3(x^3 - 3xy^2)$. Introducing δ via an orbit offset and changing the variables to action-angle, as given in Eq. (B.4), leads to the following expression:

$$\begin{aligned} N_3 = \frac{1}{6}K_3\Big[&- 3\left(\delta D_x + \sqrt{2J_x\beta_x}\cos\phi_x\right)\left(\sqrt{2J_y\beta_y}\cos\phi_y\right)^2 \\ &+ \left(\delta D_x + \sqrt{2J_x\beta_x}\cos\phi_x\right)^3\Big] \end{aligned} \tag{B.5}$$

Averaging over the cosines means integrating over $[0, \pi]$ and dividing by π:

$$\begin{aligned} \langle N_3 \rangle &= \frac{1}{\pi}\int_0^\pi N_3 \\ &= \frac{1}{6\pi^2}K_3 \cdot \left(3\pi^2 J_x\beta_x\delta D_x - 3\pi^2 J_y\beta_y\delta D_x + \pi^2\delta^3 D_x^3\right) \end{aligned} \tag{B.6}$$

Differentiating by either J_x or J_y gives the tune shift induced by a single sextupole:

$$\begin{aligned} \Delta Q_x &= \frac{1}{4\pi}K_3\beta_x D_x\delta L \\ \Delta Q_y &= -\frac{1}{4\pi}K_3\beta_y D_x\delta L \end{aligned} \tag{B.7}$$

From now on, differentiating by the action would give amplitude detuning, and by δ the chromaticity. Cross-terms exist but evidently depend on the expression of the multipole. For a sextupole, differentiating by the action does not have an effect, as no action is present in the tune shift equation. Rather, sextupoles are known to contribute to the first order chromaticity Q'. The following gives a recap of those operations:

$$\begin{aligned} \frac{\partial Q_x}{\partial J_x} &= 0 \quad ; \quad \frac{\partial Q_x}{\partial J_y} = 0 \quad ; \quad \frac{\partial Q_x}{\partial \delta} = \frac{1}{4\pi}K_3\beta_x D_x L \\ \frac{\partial Q_y}{\partial J_x} &= 0 \quad ; \quad \frac{\partial Q_y}{\partial J_y} = 0 \quad ; \quad \frac{\partial Q_y}{\partial \delta} = -\frac{1}{4\pi}K_3\beta_y D_x L \end{aligned} \tag{B.8}$$

The overall contribution of sextupoles to the Chromatic Amplitude Detuning is then highlighted in the following:

$$Q_z(\epsilon_x, \epsilon_y, \delta) = Q_{z0} + \left[\frac{\partial Q_z}{\partial \epsilon_x}\epsilon_x + \frac{\partial Q_z}{\partial \epsilon_y}\epsilon_y + \frac{\partial Q_z}{\partial \delta}\delta\right] \tag{B.9}$$

B.1.3. Octupole

With the normal hamiltonian of octupoles being $N_4 = \frac{1}{4!}K_4\left(x^4 - 6x^2y^2 + y^4\right)$, applying an orbit offset and changing for action-angle variables gives the following:

$$\begin{aligned}
N_4 = \frac{1}{24}K_4\Big[& \left(\sqrt{2J_x\beta_x} cos\phi_x\right)^4 \\
& + 4\left(\sqrt{2J_x\beta_x}\cos\phi_x\right)^3 D_x\delta \\
& + 6\left(\sqrt{2J_x\beta_x}\cos\phi_x\right)^2 D_x^2\delta^2 \\
& + 4\left(\sqrt{2J_x\beta_x}\cos\phi_x\right) D_x^2\delta \\
& + D_x^4\delta^4 \\
& - 6\left(\sqrt{2J_x\beta_x}\cos\phi_x\right)^2\left(\sqrt{2J_y\beta_y}\cos\phi_y\right)^2 \\
& - 6\left(\sqrt{2J_y\beta_y}\cos\phi_y\right)^2 \cdot 2\left(\sqrt{2J_x\beta_x}\cos\phi_x\right) D_x\delta \\
& - 6\left(\sqrt{2J_y\beta_y}\cos\phi_y\right)^2 D_x^2\delta^2 \\
& + \left(\sqrt{2J_y\beta_y}\cos\phi_y\right)^4\Big]
\end{aligned} \tag{B.10}$$

Average over the phase variables gives the following:

$$\begin{aligned}
\langle N_4\rangle &= \frac{1}{\pi}\int_0^\pi N_4 \\
&= \frac{1}{48}K_4\Big[\; 3J_x^2\beta_x^2 + 12J_x\beta_x D_x^2\delta^2 + 2D_x^4\delta^4 \\
&\qquad - 12J_y\beta_y(J_x\beta_x + D_x^2\delta^2) + 3J_y^2\beta_y^2\Big]
\end{aligned} \tag{B.11}$$

Differentiating by either J_x or J_y gives the tune shift induced by a single octupole. Contrary to sextupoles, it can be noted that some action terms $J_{x,y}$ remain in the expression.

$$\begin{aligned}
\Delta Q_x &= \frac{1}{48\pi}K_4L\left[3J_x\beta_x^2 + 6\beta_x D_x^2\delta^2 - 6\beta_x J_y\beta_y\right] \\
\Delta Q_y &= \frac{1}{48\pi}K_4L\left[-6J_x\beta_x\beta_y - 6\beta_y D_x^2\delta^2 + 3J_y\beta_y^2\right]
\end{aligned} \tag{B.12}$$

Differentiating by the action $J_{x,y}$ yields amplitude detuning, while differentiating by the momentum offset yields the second order chromaticity Q'':

$$\begin{aligned}
\frac{\partial Q_x}{\partial J_x} &= \frac{1}{16\pi}K_4\beta_x^2 L \quad ; \quad \frac{\partial Q_x}{\partial J_y} = -\frac{1}{8\pi}K_4\beta_x\beta_y L \quad ; \quad \frac{\partial^2 Q_x}{\partial \delta^2} = \frac{1}{4\pi}K_4\beta_x D_x^2 L \\
\frac{\partial Q_y}{\partial J_x} &= -\frac{1}{8\pi}K_4\beta_x\beta_y L \quad ; \quad \frac{\partial Q_y}{\partial J_y} = \frac{1}{16\pi}K_4\beta_y^2 L \quad ; \quad \frac{\partial^2 Q_y}{\partial \delta^2} = -\frac{1}{4\pi}K_4\beta_y D_x^2 L
\end{aligned} \tag{B.13}$$

The overall contribution of octupoles to the Chromatic Amplitude Detuning is then highlighted in the following:

$$\begin{aligned}
Q_z(\epsilon_x, \epsilon_y, \delta) = Q_{z0} &+ \left[\frac{\partial Q_z}{\partial \epsilon_x}\epsilon_x + \frac{\partial Q_z}{\partial \epsilon_y}\epsilon_y + \frac{\partial Q_z}{\partial \delta}\delta\right] \\
&+ \frac{1}{2!}\left[\frac{\partial^2 Q_z}{\partial \epsilon_x^2}\epsilon_x^2 + \frac{\partial^2 Q_z}{\partial \epsilon_y^2}\epsilon_y^2 + \frac{\partial^2 Q_z}{\partial \delta^2}\delta^2\right. \\
&\left. + 2\frac{\partial^2 Q_z}{\partial \epsilon_x \partial \epsilon_y}\epsilon_x\epsilon_y + 2\frac{\partial^2 Q_z}{\partial \epsilon_x \partial \delta}\epsilon_x\delta + 2\frac{\partial^2 Q_z}{\partial \delta \partial \epsilon_y}\delta\epsilon_y\right]
\end{aligned} \tag{B.14}$$

B.1.4. Decapole

Skipping the first steps detailed previously, the tune shift induced by a normal decapole is given by the following:

$$\begin{aligned}
\Delta Q_x &= \frac{1}{240\pi}K_5 L\left[10D_x^3\delta^3\beta_x + 15D_x\delta J_x\beta_x^2 - 30J_y\beta_y\beta_x D_x\delta\right] \\
\Delta Q_y &= \frac{1}{240\pi}K_5 L\left[-10D_x^3\delta^3\beta_y + 15D_x\delta J_y\beta_y^2 - 30J_x\beta_y\beta_x D_x\delta\right]
\end{aligned} \tag{B.15}$$

The terms of the chromatic amplitude detuning can now be computed. Unlike sextupoles and octupoles, cross-terms between δ and the action now appear, giving rise to *chromatic amplitude detuning* and the third order chromaticity Q''':

$$\begin{aligned}
\frac{\partial^2 Q_x}{\partial J_x \partial \delta} &= \frac{1}{16\pi}K_5\beta_x^2 D_x L \quad ; \quad \frac{\partial^2 Q_x}{\partial J_y \partial \delta} = \frac{1}{8\pi}K_5\beta_x\beta_y D_x L \quad ; \quad \frac{\partial^3 Q_x}{\partial \delta^3} = \frac{1}{4\pi}K_5\beta_x D_x^3 L \\
\frac{\partial^2 Q_y}{\partial J_x \partial \delta} &= -\frac{1}{8\pi}K_5\beta_x\beta_y D_x L \quad ; \quad \frac{\partial^2 Q_y}{\partial J_y \partial \delta} = \frac{1}{16\pi}K_5\beta_y^2 D_x L \quad ; \quad \frac{\partial^3 Q_y}{\partial \delta^3} = -\frac{1}{4\pi}K_5\beta_y D_x^3 L
\end{aligned} \tag{B.16}$$

The contribution of decapoles to Chromatic Amplitude Detuning is then the following:

$$
\begin{aligned}
Q_z(\epsilon_x, \epsilon_y, \delta) = Q_{z0} &+ \left[\frac{\partial Q_z}{\partial \epsilon_x}\epsilon_x + \frac{\partial Q_z}{\partial \epsilon_y}\epsilon_y + \frac{\partial Q_z}{\partial \delta}\delta\right] \\
&+ \frac{1}{2!}\left[\frac{\partial^2 Q_z}{\partial \epsilon_x^2}\epsilon_x^2 + \frac{\partial^2 Q_z}{\partial \epsilon_y^2}\epsilon_y^2 + \frac{\partial^2 Q_z}{\partial \delta^2}\delta^2\right. \\
&\qquad \left. + 2\frac{\partial^2 Q_z}{\partial \epsilon_x \partial \epsilon_y}\epsilon_x\epsilon_y + 2\frac{\partial^2 Q_z}{\partial \epsilon_x \partial \delta}\epsilon_x\delta + 2\frac{\partial^2 Q_z}{\partial \delta \partial \epsilon_y}\delta\epsilon_y\right] \\
&+ \frac{1}{3!}\left[\frac{\partial^3 Q_z}{\partial \delta^3}\delta^3 + \cdots\right]
\end{aligned}
\tag{B.17}
$$

B.1.5. Dodecapole

The tune shift induced by a normal dodecapole is given by the following:

$$
\begin{aligned}
Q_x &= \frac{1}{720\pi}K_6L\Big[15J_x^2\beta_x^3 + 30\beta_x D_x^4\delta^4 + 90J_x\beta_x^2D_x^2\delta^2 \\
&\qquad - 180J_y\beta_y\beta_xD_x^2\delta^2 - 90J_y\beta_yJ_x\beta_x^2 + 90J_y^2\beta_y^2\beta_x\Big] \\
Q_y &= \frac{1}{720\pi}K_6L\Big[-30\beta_yD_x^4\delta^4 - 180\beta_yJ_x\beta_xD_x^2\delta^2 - 90\beta_yJ_x^2\beta_x^2 \\
&\qquad + 90J_y\beta_y^2J_x\beta_x + 45J_y\beta_y^2D_x^2\delta^2 - 15J_y^2\beta_y^3\Big]
\end{aligned}
\tag{B.18}
$$

The terms of the chromatic amplitude detuning can now be computed. Like for decapoles, chromatic amplitude detuning terms appear, as well as the third order chromaticity $Q^{(4)}$:

$$
\begin{aligned}
\frac{\partial^2 Q_x}{\partial J_x^2} &= \frac{1}{96\pi}K_6\beta_x^3L \quad ; \quad & \frac{\partial^2 Q_y}{\partial J_y^2} &= -\frac{1}{96\pi}K_6\beta_y^3L \\
\frac{\partial^3 Q_x}{\partial J_x\partial\delta^2} &= \frac{1}{16\pi}K_6\beta_x^2D_x^2L \quad ; \quad & \frac{\partial^3 Q_y}{\partial J_y\partial\delta^2} &= \frac{1}{16\pi}K_6\beta_y^2D_x^2L \\
\frac{\partial^2 Q_x}{\partial J_y^2} &= \frac{1}{32\pi}K_6\beta_y^2\beta_xL \quad ; \quad & \frac{\partial^2 Q_y}{\partial J_x^2} &= -\frac{1}{32\pi}K_6\beta_y\beta_x^2L \\
\frac{\partial^3 Q_x}{\partial J_y\partial\delta^2} &= -\frac{1}{8\pi}K_6\beta_y\beta_xD_x^2L \quad ; \quad & \frac{\partial^3 Q_y}{\partial J_x\partial\delta^2} &= -\frac{1}{8\pi}K_6\beta_y\beta_xD_x^2L \\
\frac{\partial^2 Q_x}{\partial J_x\partial J_y} &= -\frac{1}{32\pi}K_6\beta_y\beta_x^2L \quad ; \quad & \frac{\partial^2 Q_y}{\partial J_y\partial J_x} &= \frac{1}{32\pi}K_6\beta_y^2\beta_xL \\
\frac{\partial^4 Q_x}{\partial\delta^4} &= \frac{1}{4\pi}K_6\beta_xD_x^4L \quad ; \quad & \frac{\partial^4 Q_y}{\partial\delta^4} &= -\frac{1}{4\pi}K_6\beta_yD_x^4L
\end{aligned}
\tag{B.19}
$$

The contribution of dodecapoles to Chromatic Amplitude Detuning is then the following:

$$
\begin{aligned}
Q_z(\epsilon_x, \epsilon_y, \delta) = Q_{z0} &+ \left[\frac{\partial Q_z}{\partial \epsilon_x}\epsilon_x + \frac{\partial Q_z}{\partial \epsilon_y}\epsilon_y + \frac{\partial Q_z}{\partial \delta}\delta \right] \\
&+ \frac{1}{2!}\left[\frac{\partial^2 Q_z}{\partial \epsilon_x^2}\epsilon_x^2 + \frac{\partial^2 Q_z}{\partial \epsilon_y^2}\epsilon_y^2 + 2\frac{\partial^2 Q_z}{\partial \epsilon_x \partial \epsilon_y}\epsilon_x\epsilon_y + \cdots \right] \\
&+ \frac{1}{3!}\left[3\frac{\partial^3 Q_z}{\partial \epsilon_x \partial \delta^2}\delta^2\epsilon_x + 3\frac{\partial^3 Q_z}{\partial \epsilon_y \partial \delta^2}\delta^2\epsilon_y + \cdots \right] \\
&+ \frac{1}{4!}\left[\frac{\partial^4 Q_z}{\partial \delta^4}\delta^4 \right]
\end{aligned}
\tag{B.20}
$$

B.2. PTC Validation

A simulation has been done with PTC to assess that those equations are correct. A dodecapole has been added to the lattice with a strength $KL = 1e^6$. Here are the results, confirming PTC works as intended.

The ANH numbers refer to the partial derivative relative to J_x, J_y and δ. So ANHX 021 would for example be $\frac{\partial^3 Q_x}{\partial J_y^2 \partial \delta}$.

Term	Analytical	Simulation	Rel. Diff [%]
ANH X 200	4782639.96971	4782639.97	0.0
ANH X 102	86945.930342	86945.93	-0.0
ANH X 020	593469879.552116	593469880.01	0.0
ANH X 012	-1118366.433407	-1118366.433	-0.0
ANH X 110	-92277073.535598	-92277073.6	0.0
ANH X 004	1053.754809	1053.7548	-0.000001
ANH Y 200	-92277073.535598	-92277073.6	0.0
ANH Y 102	-1118366.433407	-1118366.433	-0.0
ANH Y 020	-1272278817.264865	-1272278818.913	0.0
ANH Y 012	3596325.539479	3596325.543	0.0
ANH Y 110	593469879.552116	593469880.01	0.0
ANH Y 004	-6777.108503	-6777.1085	-0.0

C

Resonance Driving Terms

This appendix intends to clarify where Resonance Driving Terms can be seen in the frequency spectrum, what resonance they contribute to and what their action dependance is.

C.1. Expressions

The number of valid RDTs indeed grows rapidly with the magnet order n, as shows Table C.1, and is given by the following combinations:

$$C(n+3,3) - C(n+1,1) - [(n+1) \bmod 2] \cdot C\left(\left\lfloor \frac{n}{2} \right\rfloor + 1, 1\right). \tag{C.1}$$

Multipole	Order	Number of poles	Number of RDTs
Quadrupole	2	4	5
Sextupole	3	6	16
Octupole	4	8	27
Decapole	5	10	50
Dodecapole	6	12	73
Decatetrapole	7	14	112
Decahexapole	8	16	151
Hectopole	50	100	23349
Kilopole	500	1000	2.1×10^7

Table C.1.: Number of valid RDTs for a given multipole order

Several different RDTs can contribute to the same line, which can be observed in the horizontal or vertical spectrum. The tables below describe which RDTs contribute to a specific combination of line and plane. All tables have been computed up to the order 6, for decapoles. The line columns represents (Q_x, Q_y). For example (-1, 2) is $-1Q_x + 2Qy$.

As a reminder, for a given RDT f_{jklm}, we will observe:

$$\begin{aligned} &(j-k)Q_x + (l-m)Q_y = p \in \mathbb{N} && \text{excited resonance} \\ &H(1-j+k, m-l) && \text{horizontal line, if } j \neq 0 \\ &V(k-j, 1-l+m) && \text{vertical line, if } l \neq 0. \end{aligned} \tag{C.2}$$

The amplitude of each line is given by:

$$\begin{aligned} |H_{f_{jklm}}| &= 2j(2I_x)^{\frac{j+k-1}{2}}(2I_y)^{\frac{l+m}{2}}|f_{jklm}| \\ |V_{f_{jklm}}| &= 2l(2I_x)^{\frac{j+k}{2}}(2I_y)^{\frac{l+m-1}{2}}|f_{jklm}|. \end{aligned} \tag{C.3}$$

C

According to Eq. (C.2) and Eq. (C.3), it can be seen that many RDTs will not contribute to any line and thus can not be observed.

C.2. Frequency Spectrum Lines

The following Table C.2 shows which RDTs can be seen at a factor $Q_x \pm Q_y$ in the vertical or horizontal spectrums. This table is mostly useful when trying to identify which multipole or RDT contributes to a specific line that can appear during measurements.

Q_x	Q_y	H-jklm	V-jklm
−5	0	6000	5010
−4	−1	5010	4020
−4	0	5000	4010
−4	1	5001	4011
−3	−2	4020	3030
−3	−1	4010	3020
−3	0	4000, 4011, 5100	3010, 3021, 4110
−3	1	4001	3011
−3	2	4002	3012
−2	−3	3030	2040
−2	−2	3020	2030
−2	−1	3010, 3021, 4110	2020, 2031, 3120
−2	0	3000, 3011, 4100	2010, 2021, 3110
−2	1	3001, 3012, 4101	2011, 2022, 3111
−2	2	3002	2012

Q_x	Q_y	H-jklm	V-jklm
−2	3	3003	2013
−1	−4	2040	1050
−1	−3	2030	1040
−1	−2	2020, 2031, 3120	1030, 1041, 2130
−1	−1	2010, 2021, 3110	1020, 1031, 2120
−1	0	2000, 2011, 3100, 2022, 3111, 4200	1010, 1021, 2110, 1032, 2121, 3210
−1	1	2001, 2012, 3101	1011, 1022, 2111
−1	2	2002, 2013, 3102	1012, 1023, 2112
−1	3	2003	1013
−1	4	2004	1014
0	−5	1050	0060
0	−4	1040	0050
0	−3	1030, 1041, 2130	0040, 0051, 1140
0	−2	1020, 1031, 2120	0030, 0041, 1130
0	−1	1010, 1021, 2110, 1032, 2121, 3210	0020, 0031, 1120, 0042, 1131, 2220
0	0	1011, 2100, 1022, 2111, 3200	0021, 1110, 0032, 1121, 2210
0	1	1001, 1012, 2101, 1023, 2112, 3201	
0	2	1002, 1013, 2102	0012, 0023, 1112
0	3	1003, 1014, 2103	0013, 0024, 1113
0	4	1004	0014
0	5	1005	0015
1	−4	1140	0150
1	−3	1130	0140
1	−2	1120, 1131, 2220	0130, 0141, 1230
1	0		0110, 0121, 1210, 0132, 1221, 2310
1	−1	1110, 1121, 2210	0120, 0131, 1220
1	1	1101, 1112, 2201	0111, 0122, 1211
1	2	1102, 1113, 2202	0112, 0123, 1212
1	3	1103	0113
1	4	1104	0114
2	−3	1230	0240
2	−2	1220	0230
2	−1	1210, 1221, 2310	0220, 0231, 1320
2	0	1200, 1211, 2300	0210, 0221, 1310
2	1	1201, 1212, 2301	0211, 0222, 1311
2	2	1202	0212
2	3	1203	0213
3	−2	1320	0330
3	−1	1310	0320
3	0	1300, 1311, 2400	0310, 0321, 1410
3	1	1301	0311
3	2	1302	0312

Q_x	Q_y	H-jklm	V-jklm
4	−1	1410	0420
4	0	1400	0410
4	1	1401	0411
5	0	1500	0510

Table C.2.: Correspondence of Resonance Driving Terms to the lines seen in the horizontal or vertical frequency spectrum, up to dodecapoles ($n = 6$).

C.3. Amplitude, Resonances and Lines

This part focuses on individual Resonance Drivings Terms, detailing what magnet they originate from, what resonance they excite, how they can be observed and what kicks are needed in order to measure them. The amplitude columns implicitly omits the term $|f_{jklm}|$, which depends on K and J. The color coding helps quickly identifying dependences:

- I_x : depends only on horizontal amplitude
- I_y : depends only on vertical amplitude
- $I_x I_y$: depends on both horizontal and vertical amplitudes

n	jklm	Type	Resonance	H-line	V-line	Amplitude H	Amplitude V
2	0020	normal	(0, 2)		(0, -1)		$4(2I_y)^{1/2}$
2	2000	normal	(2, 0)	(-1, 0)		$4(2I_x)^{1/2}$	
2	0110	skew	(-1, 1)		(1, 0)		$2(2I_x)^{1/2}$
2	1001	skew	(1, -1)	(0, 1)		$2(2I_y)^{1/2}$	
2	1010	skew	(1, 1)	(0, -1)	(-1, 0)	$2(2I_y)^{1/2}$	$2(2I_x)^{1/2}$
3	0111	normal	(-1, 0)		(1, 1)		$2(2I_x)^{1/2}(2I_y)^{1/2}$
3	0120	normal	(-1, 2)		(1, -1)		$4(2I_x)^{1/2}(2I_y)^{1/2}$
3	1002	normal	(1, -2)	(0, 2)		$2(2I_y)$	
3	1011	normal	(1, 0)	(0, 0)	(-1, 1)	$2(2I_y)$	$2(2I_x)^{1/2}(2I_y)^{1/2}$
3	1020	normal	(1, 2)	(0, -2)	(-1, -1)	$2(2I_y)$	$4(2I_x)^{1/2}(2I_y)^{1/2}$
3	1200	normal	(-1, 0)	(2, 0)		$2(2I_x)$	
3	2100	normal	(1, 0)	(0, 0)		$4(2I_x)$	
3	3000	normal	(3, 0)	(-2, 0)		$6(2I_x)$	
3	0012	skew	(0, -1)		(0, 2)		$2(2I_y)$
3	0021	skew	(0, 1)		(0, 0)		$4(2I_y)$
3	0030	skew	(0, 3)		(0, -2)		$6(2I_y)$
3	0210	skew	(-2, 1)		(2, 0)		$2(2I_x)$

n	jklm	Type	Resonance	H-line	V-line	Amplitude H	Amplitude V
3	1101	skew	(0, -1)	(1, 1)		$2(2I_x)^{1/2}(2I_y)^{1/2}$	
3	1110	skew	(0, 1)	(1, -1)	(0, 0)	$2(2I_x)^{1/2}(2I_y)^{1/2}$	$2(2I_x)$
3	2001	skew	(2, -1)	(-1, 1)		$4(2I_x)^{1/2}(2I_y)^{1/2}$	
3	2010	skew	(2, 1)	(-1, -1)	(-2, 0)	$4(2I_x)^{1/2}(2I_y)^{1/2}$	$2(2I_x)$
4	0013	normal	(0, -2)		(0, 3)		$2(2I_y)^{3/2}$
4	0031	normal	(0, 2)		(0, -1)		$6(2I_y)^{3/2}$
4	0040	normal	(0, 4)		(0, -3)		$8(2I_y)^{3/2}$
4	0211	normal	(-2, 0)		(2, 1)		$2(2I_x)(2I_y)^{1/2}$
4	0220	normal	(-2, 2)		(2, -1)		$4(2I_x)(2I_y)^{1/2}$
4	1102	normal	(0, -2)	(1, 2)		$2(2I_x)^{1/2}(2I_y)$	
4	1120	normal	(0, 2)	(1, -2)	(0, -1)	$2(2I_x)^{1/2}(2I_y)$	$4(2I_x)(2I_y)^{1/2}$
4	1300	normal	(-2, 0)	(3, 0)		$2(2I_x)^{3/2}$	
4	2002	normal	(2, -2)	(-1, 2)		$4(2I_x)^{1/2}(2I_y)$	
4	2011	normal	(2, 0)	(-1, 0)	(-2, 1)	$4(2I_x)^{1/2}(2I_y)$	$2(2I_x)(2I_y)^{1/2}$
4	2020	normal	(2, 2)	(-1, -2)	(-2, -1)	$4(2I_x)^{1/2}(2I_y)$	$4(2I_x)(2I_y)^{1/2}$
4	3100	normal	(2, 0)	(-1, 0)		$6(2I_x)^{3/2}$	
4	4000	normal	(4, 0)	(-3, 0)		$8(2I_x)^{3/2}$	
4	0112	skew	(-1, -1)		(1, 2)		$2(2I_x)^{1/2}(2I_y)$
4	0121	skew	(-1, 1)		(1, 0)		$4(2I_x)^{1/2}(2I_y)$
4	0130	skew	(-1, 3)		(1, -2)		$6(2I_x)^{1/2}(2I_y)$
4	0310	skew	(-3, 1)		(3, 0)		$2(2I_x)^{3/2}$
4	1003	skew	(1, -3)	(0, 3)		$2(2I_y)^{3/2}$	
4	1012	skew	(1, -1)	(0, 1)	(-1, 2)	$2(2I_y)^{3/2}$	$2(2I_x)^{1/2}(2I_y)$
4	1021	skew	(1, 1)	(0, -1)	(-1, 0)	$2(2I_y)^{3/2}$	$4(2I_x)^{1/2}(2I_y)$
4	1030	skew	(1, 3)	(0, -3)	(-1, -2)	$2(2I_y)^{3/2}$	$6(2I_x)^{1/2}(2I_y)$
4	1201	skew	(-1, -1)	(2, 1)		$2(2I_x)(2I_y)^{1/2}$	
4	1210	skew	(-1, 1)	(2, -1)	(1, 0)	$2(2I_x)(2I_y)^{1/2}$	$2(2I_x)^{3/2}$
4	2101	skew	(1, -1)	(0, 1)		$4(2I_x)(2I_y)^{1/2}$	
4	2110	skew	(1, 1)	(0, -1)	(-1, 0)	$4(2I_x)(2I_y)^{1/2}$	$2(2I_x)^{3/2}$
4	3001	skew	(3, -1)	(-2, 1)		$6(2I_x)(2I_y)^{1/2}$	
4	3010	skew	(3, 1)	(-2, -1)	(-3, 0)	$6(2I_x)(2I_y)^{1/2}$	$2(2I_x)^{3/2}$
5	0113	normal	(-1, -2)		(1, 3)		$2(2I_x)^{1/2}(2I_y)^{3/2}$
5	0122	normal	(-1, 0)		(1, 1)		$4(2I_x)^{1/2}(2I_y)^{3/2}$
5	0131	normal	(-1, 2)		(1, -1)		$6(2I_x)^{1/2}(2I_y)^{3/2}$
5	0140	normal	(-1, 4)		(1, -3)		$8(2I_x)^{1/2}(2I_y)^{3/2}$

n	jklm	Type	Resonance	H-line	V-line	Amplitude H	Amplitude V
5	0311	normal	(-3, 0)		(3, 1)		$2(2I_x)^{3/2}(2I_y)^{1/2}$
5	0320	normal	(-3, 2)		(3, -1)		$4(2I_x)^{3/2}(2I_y)^{1/2}$
5	1004	normal	(1, -4)	(0, 4)		$2(2I_y)^2$	
5	1013	normal	(1, -2)	(0, 2)	(-1, 3)	$2(2I_y)^2$	$2(2I_x)^{1/2}(2I_y)^{3/2}$
5	1022	normal	(1, 0)	(0, 0)	(-1, 1)	$2(2I_y)^2$	$4(2I_x)^{1/2}(2I_y)^{3/2}$
5	1031	normal	(1, 2)	(0, -2)	(-1, -1)	$2(2I_y)^2$	$6(2I_x)^{1/2}(2I_y)^{3/2}$
5	1040	normal	(1, 4)	(0, -4)	(-1, -3)	$2(2I_y)^2$	$8(2I_x)^{1/2}(2I_y)^{3/2}$
5	1202	normal	(-1, -2)	(2, 2)		$2(2I_x)(2I_y)$	
5	1211	normal	(-1, 0)	(2, 0)	(1, 1)	$2(2I_x)(2I_y)$	$2(2I_x)^{3/2}(2I_y)^{1/2}$
5	1220	normal	(-1, 2)	(2, -2)	(1, -1)	$2(2I_x)(2I_y)$	$4(2I_x)^{3/2}(2I_y)^{1/2}$
5	1400	normal	(-3, 0)	(4, 0)		$2(2I_x)^2$	
5	2102	normal	(1, -2)	(0, 2)		$4(2I_x)(2I_y)$	
5	2111	normal	(1, 0)	(0, 0)	(-1, 1)	$4(2I_x)(2I_y)$	$2(2I_x)^{3/2}(2I_y)^{1/2}$
5	2120	normal	(1, 2)	(0, -2)	(-1, -1)	$4(2I_x)(2I_y)$	$4(2I_x)^{3/2}(2I_y)^{1/2}$
5	2300	normal	(-1, 0)	(2, 0)		$4(2I_x)^2$	
5	3002	normal	(3, -2)	(-2, 2)		$6(2I_x)(2I_y)$	
5	3011	normal	(3, 0)	(-2, 0)	(-3, 1)	$6(2I_x)(2I_y)$	$2(2I_x)^{3/2}(2I_y)^{1/2}$
5	3020	normal	(3, 2)	(-2, -2)	(-3, -1)	$6(2I_x)(2I_y)$	$4(2I_x)^{3/2}(2I_y)^{1/2}$
5	3200	normal	(1, 0)	(0, 0)		$6(2I_x)^2$	
5	4100	normal	(3, 0)	(-2, 0)		$8(2I_x)^2$	
5	5000	normal	(5, 0)	(-4, 0)		$10(2I_x)^2$	
5	0014	skew	(0, -3)		(0, 4)		$2(2I_y)^2$
5	0023	skew	(0, -1)		(0, 2)		$4(2I_y)^2$
5	0032	skew	(0, 1)		(0, 0)		$6(2I_y)^2$
5	0041	skew	(0, 3)		(0, -2)		$8(2I_y)^2$
5	0050	skew	(0, 5)		(0, -4)		$10(2I_y)^2$
5	0212	skew	(-2, -1)		(2, 2)		$2(2I_x)(2I_y)$
5	0221	skew	(-2, 1)		(2, 0)		$4(2I_x)(2I_y)$
5	0230	skew	(-2, 3)		(2, -2)		$6(2I_x)(2I_y)$
5	0410	skew	(-4, 1)		(4, 0)		$2(2I_x)^2$
5	1103	skew	(0, -3)	(1, 3)		$2(2I_x)^{1/2}(2I_y)^{3/2}$	
5	1112	skew	(0, -1)	(1, 1)	(0, 2)	$2(2I_x)^{1/2}(2I_y)^{3/2}$	$2(2I_x)(2I_y)$
5	1121	skew	(0, 1)	(1, -1)	(0, 0)	$2(2I_x)^{1/2}(2I_y)^{3/2}$	$4(2I_x)(2I_y)$
5	1130	skew	(0, 3)	(1, -3)	(0, -2)	$2(2I_x)^{1/2}(2I_y)^{3/2}$	$6(2I_x)(2I_y)$
5	1301	skew	(-2, -1)	(3, 1)		$2(2I_x)^{3/2}(2I_y)^{1/2}$	
5	1310	skew	(-2, 1)	(3, -1)	(2, 0)	$2(2I_x)^{3/2}(2I_y)^{1/2}$	$2(2I_x)^2$

n	jklm	Type	Resonance	H-line	V-line	Amplitude H	Amplitude V
5	2003	skew	(2, -3)	(-1, 3)		$4(2I_x)^{1/2}(2I_y)^{3/2}$	
5	2012	skew	(2, -1)	(-1, 1)	(-2, 2)	$4(2I_x)^{1/2}(2I_y)^{3/2}$	$2(2I_x)(2I_y)$
5	2021	skew	(2, 1)	(-1, -1)	(-2, 0)	$4(2I_x)^{1/2}(2I_y)^{3/2}$	$4(2I_x)(2I_y)$
5	2030	skew	(2, 3)	(-1, -3)	(-2, -2)	$4(2I_x)^{1/2}(2I_y)^{3/2}$	$6(2I_x)(2I_y)$
5	2201	skew	(0, -1)	(1, 1)		$4(2I_x)^{3/2}(2I_y)^{1/2}$	
5	2210	skew	(0, 1)	(1, -1)	(0, 0)	$4(2I_x)^{3/2}(2I_y)^{1/2}$	$2(2I_x)^2$
5	3101	skew	(2, -1)	(-1, 1)		$6(2I_x)^{3/2}(2I_y)^{1/2}$	
5	3110	skew	(2, 1)	(-1, -1)	(-2, 0)	$6(2I_x)^{3/2}(2I_y)^{1/2}$	$2(2I_x)^2$
5	4001	skew	(4, -1)	(-3, 1)		$8(2I_x)^{3/2}(2I_y)^{1/2}$	
5	4010	skew	(4, 1)	(-3, -1)	(-4, 0)	$8(2I_x)^{3/2}(2I_y)^{1/2}$	$2(2I_x)^2$
6	0015	normal	(0, -4)		(0, 5)		$2(2I_y)^{5/2}$
6	0024	normal	(0, -2)		(0, 3)		$4(2I_y)^{5/2}$
6	0042	normal	(0, 2)		(0, -1)		$8(2I_y)^{5/2}$
6	0051	normal	(0, 4)		(0, -3)		$10(2I_y)^{5/2}$
6	0060	normal	(0, 6)		(0, -5)		$12(2I_y)^{5/2}$
6	0213	normal	(-2, -2)		(2, 3)		$2(2I_x)(2I_y)^{3/2}$
6	0222	normal	(-2, 0)		(2, 1)		$4(2I_x)(2I_y)^{3/2}$
6	0231	normal	(-2, 2)		(2, -1)		$6(2I_x)(2I_y)^{3/2}$
6	0240	normal	(-2, 4)		(2, -3)		$8(2I_x)(2I_y)^{3/2}$
6	0411	normal	(-4, 0)		(4, 1)		$2(2I_x)^2(2I_y)^{1/2}$
6	0420	normal	(-4, 2)		(4, -1)		$4(2I_x)^2(2I_y)^{1/2}$
6	1104	normal	(0, -4)	(1, 4)		$2(2I_x)^{1/2}(2I_y)^2$	
6	1113	normal	(0, -2)	(1, 2)	(0, 3)	$2(2I_x)^{1/2}(2I_y)^2$	$2(2I_x)(2I_y)^{3/2}$
6	1131	normal	(0, 2)	(1, -2)	(0, -1)	$2(2I_x)^{1/2}(2I_y)^2$	$6(2I_x)(2I_y)^{3/2}$
6	1140	normal	(0, 4)	(1, -4)	(0, -3)	$2(2I_x)^{1/2}(2I_y)^2$	$8(2I_x)(2I_y)^{3/2}$
6	1302	normal	(-2, -2)	(3, 2)		$2(2I_x)^{3/2}(2I_y)$	
6	1311	normal	(-2, 0)	(3, 0)	(2, 1)	$2(2I_x)^{3/2}(2I_y)$	$2(2I_x)^2(2I_y)^{1/2}$
6	1320	normal	(-2, 2)	(3, -2)	(2, -1)	$2(2I_x)^{3/2}(2I_y)$	$4(2I_x)^2(2I_y)^{1/2}$
6	1500	normal	(-4, 0)	(5, 0)		$2(2I_x)^{5/2}$	
6	2004	normal	(2, -4)	(-1, 4)		$4(2I_x)^{1/2}(2I_y)^2$	
6	2013	normal	(2, -2)	(-1, 2)	(-2, 3)	$4(2I_x)^{1/2}(2I_y)^2$	$2(2I_x)(2I_y)^{3/2}$
6	2022	normal	(2, 0)	(-1, 0)	(-2, 1)	$4(2I_x)^{1/2}(2I_y)^2$	$4(2I_x)(2I_y)^{3/2}$
6	2031	normal	(2, 2)	(-1, -2)	(-2, -1)	$4(2I_x)^{1/2}(2I_y)^2$	$6(2I_x)(2I_y)^{3/2}$
6	2040	normal	(2, 4)	(-1, -4)	(-2, -3)	$4(2I_x)^{1/2}(2I_y)^2$	$8(2I_x)(2I_y)^{3/2}$
6	2202	normal	(0, -2)	(1, 2)		$4(2I_x)^{3/2}(2I_y)$	

n	jklm	Type	Resonance	H-line	V-line	Amplitude H	Amplitude V
6	2220	normal	(0, 2)	(1, -2)	(0, -1)	$4(2I_x)^{3/2}(2I_y)$	$4(2I_x)^2(2I_y)^{1/2}$
6	2400	normal	(-2, 0)	(3, 0)		$4(2I_x)^{5/2}$	
6	3102	normal	(2, -2)	(-1, 2)		$6(2I_x)^{3/2}(2I_y)$	
6	3111	normal	(2, 0)	(-1, 0)	(-2, 1)	$6(2I_x)^{3/2}(2I_y)$	$2(2I_x)^2(2I_y)^{1/2}$
6	3120	normal	(2, 2)	(-1, -2)	(-2, -1)	$6(2I_x)^{3/2}(2I_y)$	$4(2I_x)^2(2I_y)^{1/2}$
6	4002	normal	(4, -2)	(-3, 2)		$8(2I_x)^{3/2}(2I_y)$	
6	4011	normal	(4, 0)	(-3, 0)	(-4, 1)	$8(2I_x)^{3/2}(2I_y)$	$2(2I_x)^2(2I_y)^{1/2}$
6	4020	normal	(4, 2)	(-3, -2)	(-4, -1)	$8(2I_x)^{3/2}(2I_y)$	$4(2I_x)^2(2I_y)^{1/2}$
6	4200	normal	(2, 0)	(-1, 0)		$8(2I_x)^{5/2}$	
6	5100	normal	(4, 0)	(-3, 0)		$10(2I_x)^{5/2}$	
6	6000	normal	(6, 0)	(-5, 0)		$12(2I_x)^{5/2}$	
6	0114	skew	(-1, -3)		(1, 4)		$2(2I_x)^{1/2}(2I_y)^2$
6	0123	skew	(-1, -1)		(1, 2)		$4(2I_x)^{1/2}(2I_y)^2$
6	0132	skew	(-1, 1)		(1, 0)		$6(2I_x)^{1/2}(2I_y)^2$
6	0141	skew	(-1, 3)		(1, -2)		$8(2I_x)^{1/2}(2I_y)^2$
6	0150	skew	(-1, 5)		(1, -4)		$10(2I_x)^{1/2}(2I_y)^2$
6	0312	skew	(-3, -1)		(3, 2)		$2(2I_x)^{3/2}(2I_y)$
6	0321	skew	(-3, 1)		(3, 0)		$4(2I_x)^{3/2}(2I_y)$
6	0330	skew	(-3, 3)		(3, -2)		$6(2I_x)^{3/2}(2I_y)$
6	0510	skew	(-5, 1)		(5, 0)		$2(2I_x)^{5/2}$
6	1005	skew	(1, -5)	(0, 5)		$2(2I_y)^{5/2}$	
6	1014	skew	(1, -3)	(0, 3)	(-1, 4)	$2(2I_y)^{5/2}$	$2(2I_x)^{1/2}(2I_y)^2$
6	1023	skew	(1, -1)	(0, 1)	(-1, 2)	$2(2I_y)^{5/2}$	$4(2I_x)^{1/2}(2I_y)^2$
6	1032	skew	(1, 1)	(0, -1)	(-1, 0)	$2(2I_y)^{5/2}$	$6(2I_x)^{1/2}(2I_y)^2$
6	1041	skew	(1, 3)	(0, -3)	(-1, -2)	$2(2I_y)^{5/2}$	$8(2I_x)^{1/2}(2I_y)^2$
6	1050	skew	(1, 5)	(0, -5)	(-1, -4)	$2(2I_y)^{5/2}$	$10(2I_x)^{1/2}(2I_y)^2$
6	1203	skew	(-1, -3)	(2, 3)		$2(2I_x)(2I_y)^{3/2}$	
6	1212	skew	(-1, -1)	(2, 1)	(1, 2)	$2(2I_x)(2I_y)^{3/2}$	$2(2I_x)^{3/2}(2I_y)$
6	1221	skew	(-1, 1)	(2, -1)	(1, 0)	$2(2I_x)(2I_y)^{3/2}$	$4(2I_x)^{3/2}(2I_y)$
6	1230	skew	(-1, 3)	(2, -3)	(1, -2)	$2(2I_x)(2I_y)^{3/2}$	$6(2I_x)^{3/2}(2I_y)$
6	1401	skew	(-3, -1)	(4, 1)		$2(2I_x)^2(2I_y)^{1/2}$	
6	1410	skew	(-3, 1)	(4, -1)	(3, 0)	$2(2I_x)^2(2I_y)^{1/2}$	$2(2I_x)^{5/2}$
6	2103	skew	(1, -3)	(0, 3)		$4(2I_x)(2I_y)^{3/2}$	
6	2112	skew	(1, -1)	(0, 1)	(-1, 2)	$4(2I_x)(2I_y)^{3/2}$	$2(2I_x)^{3/2}(2I_y)$
6	2121	skew	(1, 1)	(0, -1)	(-1, 0)	$4(2I_x)(2I_y)^{3/2}$	$4(2I_x)^{3/2}(2I_y)$

n	jklm	Type	Resonance	H-line	V-line	Amplitude H	Amplitude V
6	2130	skew	(1, 3)	(0, -3)	(-1, -2)	$4(2I_x)(2I_y)^{3/2}$	$6(2I_x)^{3/2}(2I_y)$
6	2301	skew	(-1, -1)	(2, 1)		$4(2I_x)^2(2I_y)^{1/2}$	
6	2310	skew	(-1, 1)	(2, -1)	(1, 0)	$4(2I_x)^2(2I_y)^{1/2}$	$2(2I_x)^{5/2}$
6	3003	skew	(3, -3)	(-2, 3)		$6(2I_x)(2I_y)^{3/2}$	
6	3012	skew	(3, -1)	(-2, 1)	(-3, 2)	$6(2I_x)(2I_y)^{3/2}$	$2(2I_x)^{3/2}(2I_y)$
6	3021	skew	(3, 1)	(-2, -1)	(-3, 0)	$6(2I_x)(2I_y)^{3/2}$	$4(2I_x)^{3/2}(2I_y)$
6	3030	skew	(3, 3)	(-2, -3)	(-3, -2)	$6(2I_x)(2I_y)^{3/2}$	$6(2I_x)^{3/2}(2I_y)$
6	3201	skew	(1, -1)	(0, 1)		$6(2I_x)^2(2I_y)^{1/2}$	
6	3210	skew	(1, 1)	(0, -1)	(-1, 0)	$6(2I_x)^2(2I_y)^{1/2}$	$2(2I_x)^{5/2}$
6	4101	skew	(3, -1)	(-2, 1)		$8(2I_x)^2(2I_y)^{1/2}$	
6	4110	skew	(3, 1)	(-2, -1)	(-3, 0)	$8(2I_x)^2(2I_y)^{1/2}$	$2(2I_x)^{5/2}$
6	5001	skew	(5, -1)	(-4, 1)		$10(2I_x)^2(2I_y)^{1/2}$	
6	5010	skew	(5, 1)	(-4, -1)	(-5, 0)	$10(2I_x)^2(2I_y)^{1/2}$	$2(2I_x)^{5/2}$

Table C.3.: Amplitude dependence, associated resonance and spectrum correspondence of Resonance Driving Terms up to dodecapoles ($n = 6$).

Bibliography

[1] P.J. Bryant. "A brief history and review of accelerators". In: *CAS - CERN Accelerator School : 5th General Accelerator Physics Course* (1994). DOI: 10.5170/CERN-1994-001.1. URL: https://cds.cern.ch/record/261062.

[2] Mike Poole, John Dainton, and Swapan Chattopadhyay. "Cockcroft's subatomic legacy: splitting the atom". In: *CERN Courier* (2007). URL: https://cerncourier.com/a/cockcrofts-subatomic-legacy-splitting-the-atom/.

[3] Matthieu Lebois. *Rapport d'Activité pour la Plateforme ALTO*. Tech. rep. 2020. URL: https://www.in2p3.cnrs.fr/sites/institut_in2p3/files/page/2020-04/3-Doc-LEBOIS.pdf.

[4] F Hinterberger. "Electrostatic accelerators". In: (2006). DOI: 10.5170/CERN-2006-012.95. URL: https://cds.cern.ch/record/1005042.

[5] M Vretenar. "Radio frequency for particle accelerators: evolution and anatomy of a technology". In: (2011). DOI: 10.5170/CERN-2011-007.1. URL: https://cds.cern.ch/record/1415638/.

[6] Bryant Philip and Kurt Hübner. "CERN's ISR: the world's first hadron collider". In: (2011). URL: https://cerncourier.com/a/cerns-isr-the-worlds-first-hadron-collider/.

[7] *The CERN accelerator complex, layout in 2022*. 2022. URL: https://cds.cern.ch/record/2800984.

[8] *CERN Resources Website*. URL: https://home.cern/resources.

[9] J Gareyte, J P Koutchouk, and F Ruggiero. *Landau Damping, Dynamic Aperture and Octupoles in LHC*. LHC Project Report 91. CERN, 1997. URL: https://cds.cern.ch/record/321824.

[10] Oliver Sim Brüning et al. *LHC Design Report*. 2004. DOI: 10.5170/CERN-2004-003-V-1.

[11] Jorg Wenniger. *LHC Modes*. Tech. rep. LHC-OP-ES-0022. 2019. URL: https://edms.cern.ch/ui/file/1070479/2.1/LHC-OP-ES-0022-V2.1.pdf.

[12] L Bottura et al. *Pre-Cycles of the LHC Magnets during Operation*. Tech. rep. CERN-ATS-2010-174. 2010. URL: https://cds.cern.ch/record/1283477.

[13] Félix Soubelet. “Local Interaction Region Coupling Correction for the LHC”. PhD thesis. 2023. URL: https://cds.cern.ch/record/2891759.

[14] Joschua Dilly. “Corrections of High-Order Nonlinear Errors in the LHC and HL-LHC Beam Optics”. To Be Submitted. Humboldt University of Berlin, 2022.

[15] Helmut Wiedemann. *Particle Accelerator Physics*. 4th. Graduate Texts in Physics. Cham: Springer International Publishing, 2015. DOI: 10.1007/978-3-319-18317-6. URL: http://link.springer.com/10.1007/978-3-319-18317-6.

[16] Rob Wolf. *Engineering Specification: Field Error Naming Conventions for LHC Magnets*. Tech. rep. LHC-M-ES-001.00. CERN, 2001. URL: https://lhc-div-mms.web.cern.ch/lhc-div-mms/tests/MAG/FiDeL/Documentation/lhc-m-es-0001-30-00.pdf.

[17] B. J. Holzer et al. “Design and Principles of Synchrotrons and Circular Colliders”. In: *Particle Physics Reference Library : Volume 3: Accelerators and Colliders*. Ed. by Stephen Myers and Herwig Schopper. Cham: Springer International Publishing, 2020. DOI: 10.1007/978-3-030-34245-6_6. URL: https://doi.org/10.1007/978-3-030-34245-6_6.

[18] Andrzej Wolski. *Beam Dynamics in High Energy Particle Accelerators*. London : Singapore ; Hackensack, NJ: Imperial College Press ; Distributed by World Scientific, 2014.

[19] Laurent Deniau. *Magnetic model of Main Dipoles*. Technology Department. CERN, 2009.

[20] P. Hagen et al. *Wise: An adaptive simulation of the LHC optics*. Tech. rep. 2006. URL: https://cds.cern.ch/record/977794/files/lhc-project-report-971.pdf.

[21] *FiDeL - the magnetic model of the LHC*. 2021. URL: https://lhc-div-mms.web.cern.ch/tests/MAG/Fidel/.

[22] E. D Courant and H. S Snyder. “Theory of the Alternating-Gradient Synchrotron”. In: *Annals of Physics* 3.1 (1958). DOI: 10.1016/0003-4916(58)90012-5. URL: http://www.sciencedirect.com/science/article/pii/0003491658900125.

[23] S. Y. Lee. *Accelerator Physics*. Second. Hackensack, N.J: World Scientific, 2004.

[24] A J Dragt. “An Overview of Lie Methods for Accelerator Physics”. In: *Proceedings of PAC*. Pasadena, CA USA: JACoW, 2013.

[25] Ghislain J Roy. “Analysis of the optics of the Final Focus Test Beam using Lie algebra based techniques”. PhD thesis. 1992.

[26] Etienne Forest. *Beam dynamics: a new attitude and framework*. The physics and technology of particle and photon beams 8. Amsterdam: Harwood Academic, 1998.

[27] Fernando Casas and Ander Murua. “An efficient algorithm for computing the Baker-Campbell-Hausdorff series and some of its applications”. In: *Journal of Mathematical Physics* 50.3 (2009). DOI: 10.1063/1.3078418. URL: http://arxiv.org/abs/0810.2656.

[28] Felix Simon Carlier. "A Nonlinear Future: Measurements and Corrections of Nonlinear Beam Dynamics Using Forced Transverse Oscillations". PhD Thesis. 2020. URL: http://cds.cern.ch/record/2715765/.

[29] Andrea Franchi. "Studies and Measurements of Linear Coupling and Nonlinearities in Hadron Circular Accelerators". Doctoral Thesis. Johann Wolfgang Goethe-Universität, 2006. URL: https://publikationen.ub.uni-frankfurt.de/frontdoor/index/index/year/2006/docId/2270.

[30] Werner Herr. *Mathematical and Numerical Methods for Non-linear Beam Dynamics*. Tech. rep. CERN Accelerator School, 2018. URL: http://arxiv.org/abs/2006.09052.

[31] Keintzel Jacqueline. "Beam Optics Design, Measurement and Correction Strategies for Circular Colliders at the Energy and Luminosity Frontier". PhD thesis.

[32] Joschua Dilly and Mael Le Garrec. *On the derivation of Amplitude Detuning and Chromaticity Formulas for Particle Accelerators*. 2023. URL: http://arxiv.org/abs/2301.09132.

[33] Jacqueline Keintzel et al. "Second-Order Dispersion Measurement in LHC". In: *IPAC'19*. Melbourne, Australia, 2019. DOI: 10.18429/JACoW-IPAC2019-MOPMP027.

[34] R. Bartolini and F. Schmidt. "Normal Form via Tracking or Beam Data". In: *Part. Accel.* 59.LHC-Project-Report-132 (1997).

[35] M. Wendt. "BPM Systems: A Brief Introduction to Beam Position Monitoring". In: *ArXiv200514081 Phys.* (2020). URL: http://arxiv.org/abs/2005.14081.

[36] S Redaelli et al. "LHC Collimator Controls for a Safe LHC Operation". In: vol. C111010. Grenoble, France, 2011. URL: https://cds.cern.ch/record/1562636.

[37] R Schmidt. *Machine Protection*. 2014. DOI: 10.5170/CERN-2014-009.221. URL: https://cds.cern.ch/record/1982423.

[38] P Odier, M Ludwig, and S Thoulet. "The DCCT for the LHC Beam Intensity Measurement". In: Basel, Switzerland, 2009. URL: https://epaper.kek.jp/d09/papers/mopd45.pdf.

[39] A. Boccardi et al. *First Results from the LHC BBQ Tune and Chromaticity Systems*. 2009. URL: http://cds.cern.ch/record/1156349/.

[40] M. Gasior and R. Jones. *High Sensitivity Tune Measurement by Direct Diode Detection*. Tech. rep. CERN-AB-2005-060. 2005. URL: https://cds.cern.ch/record/895142.

[41] R. Miyamoto et al. "Parametrization of the driven betatron oscillation". In: *Physical Review Special Topics - Accelerators and Beams* 11.8 (2008). DOI: 10.1103/PhysRevSTAB.11.084002. URL: https://link.aps.org/doi/10.1103/PhysRevSTAB.11.084002.

[42] Javier Serrano and Matthieu Cattin. *The LHC AC Dipole system: an introduction*. 2010.

[43] Laurent Deniau et al. *MAD-X User Guide*. URL: http://cern.ch/madx/releases/last-rel/madxuguide.pdf.

[44] Laurent Deniau, Joschua Gray, and Riccardo De Maria. *MAD-NG*. 2020. URL: https://github.com/MethodicalAcceleratorDesign/MAD-NG.

[45] G. Iadarola et al. *Xsuite*. URL: https://github.com/xsuite/xsuite.

[46] M. Le Garrec. *Non-linear Chromaticity GUI*. 2022. URL: https://gitlab.cern.ch/mlegarre/nl-chroma-gui.

[47] OMC-Team. *Beta-Beat GUI*. 2008. URL: https://gitlab.cern.ch/acc-co/lhc/lhc-app-beta-beating.

[48] OMC-Team et al. *OMC3*. 2021. DOI: 10.5281/ZENODO.5705625. URL: https://github.com/pylhc/omc3.

[49] OMC-Team. *Beta-Beat.src*. 2018. URL: https://github.com/pylhc/Beta-Beat.src.

[50] OMC-Team. *OMC Website*. 2020. URL: https://pylhc.github.io/.

[51] N. Catalan-Lasheras, Stéphane David Fartoukh, and Jean-Pierre Koutchouk. *Linear Optics Measurements Using an AC-Dipole Excitation*. Tech. rep. 2004. URL: http://cds.cern.ch/record/712136.

[52] Michiko G. Minty and Frank Zimmermann. *Measurement and Control of Charged Particle Beams*. Particle Acceleration and Detection. Berlin, Heidelberg: Springer Berlin Heidelberg, 2003. DOI: 10.1007/978-3-662-08581-3. URL: http://link.springer.com/10.1007/978-3-662-08581-3.

[53] A. Langner et al. “Utilizing the N Beam Position Monitor Method for Turn-by-Turn Optics Measurements”. In: *Phys. Rev. Accel. Beams* 19.9 (2016). DOI: 10.1103/PhysRevAccelBeams.19.092803. URL: https://link.aps.org/doi/10.1103/PhysRevAccelBeams.19.092803.

[54] A. Wegscheider et al. “Analytical N beam position monitor method”. In: *Physical Review Accelerators and Beams* 20.11 (2017). DOI: 10.1103/PhysRevAccelBeams.20.111002. URL: https://link.aps.org/doi/10.1103/PhysRevAccelBeams.20.111002.

[55] Ana García-Tabarés Valdivieso and Rogelio Tomas. “Optics-Measurement-Based Beam Position Monitor Calibrations in the LHC Insertion Regions”. In: *Phys. Rev. Accel. Beams* 23.4 (2020). DOI: 10.1103/PhysRevAccelBeams.23.042801. URL: https://link.aps.org/doi/10.1103/PhysRevAccelBeams.23.042801.

[56] A. Franchi, Rogelio Tomás, and G. Vanbavinkhove. *Computation of the Coupling Resonance Driving Term F1001 and the Coupling Coefficient C from Turn-by-Turn Single-BPM Data*. Tech. rep. 2010. URL: http://cds.cern.ch/record/1264111.

[57] R. Tomás et al. “CERN Large Hadron Collider Optics Model, Measurements, and Corrections”. In: *Phys. Rev. ST Accel. Beams* 13.12 (2010). DOI: 10.1103/PhysRevSTAB.13.121004. URL: https://link.aps.org/doi/10.1103/PhysRevSTAB.13.121004.

[58] Félix Simon Carlier. “A nonlinear future: measurements and corrections of nonlinear beam dynamics using forced transverse oscillations”. PhD thesis. 2020.

[59] Ewen Hamish Maclean et al. *Commissioning of the nonlinear chromaticity at injection for LHC Run II.* Accelerators & Technology Sector Note 2016-0013. 2016. URL: https://cds.cern.ch/record/2121333.

[60] E H Maclean et al. "Non-linear Chromaticity Studies of the LHC at Injection". In: *Proc. IPAC'11.* San Sebastian, Spain, Sep. 2011: JACoW Publishing, Geneva, Switzerland, 2011. URL: https://jacow.org/IPAC2011/papers/WEPC078.pdf.

[61] Ewen Hamish Maclean, Felix Simon Carlier, and Jaime Coello de Portugal. "Commissioning of Non-linear Optics in the LHC at Injection Energy". In: *Proc. IPAC.* Busan, Korea, 2016. DOI: 10.18429/JACoW-IPAC2016-THPMR039. URL: https://cds.cern.ch/record/2207446.

[62] Ewen Hamish Maclean et al. "Measurement of Nonlinear Observables in the Large Hadron Collider Using Kicked Beams". In: *Phys. Rev. ST Accel. Beams* 17.8 (2014). DOI: 10.1103/PhysRevSTAB.17.081002. URL: https://link.aps.org/doi/10.1103/PhysRevSTAB.17.081002.

[63] W. Venturini Delsolaro and R Wolf. *Magnetic Behavior of LHC Superconducting Correctors: Issues for Machine Operation.* Tech. rep. 2005. URL: https://cds.cern.ch/record/987834/.

[64] *Ten out of ten for LHC decapole magnets.* Tech. rep. BUL-NA-2001-041. 2001. URL: https://cds.cern.ch/record/45154.

[65] Yannis Papaphilippou. "Detecting chaos in particle accelerators through the frequency map analysis method". In: *arXiv:1406.1545* (2014). DOI: https://doi.org/10.48550/arXiv.1406.1545. URL: https://cds.cern.ch/record/1708155/.

[66] A. Franchi et al. "First Simultaneous Measurement of Sextupolar and Octupolar Resonance Driving Terms in a Circular Accelerator from Turn-by-Turn Beam Position Monitors Data". In: *Phys. Rev. Spec. Top. - Accel. Beams* 17.7 (2014). DOI: 10.1103/PhysRevSTAB.17.074001.

[67] Riccardo de Maria. "LHC Interaction region upgrade". PhD thesis. 2008. URL: https://cds.cern.ch/record/1127611.

[68] Ewen H. Maclean et al. "Prospects for beam-based study of dodecapole nonlinearities in the CERN High-Luminosity Large Hadron Collider". In: *The European Physical Journal Plus* 137.11 (2022). DOI: 10.1140/epjp/s13360-022-03367-2. URL: https://link.springer.com/10.1140/epjp/s13360-022-03367-2.

[69] Laurent Deniau. *Private communication.* 2024.

[70] Sergey Antipov et al. "Single-Collimator Tune Shift Measurement of the Three-Stripe Collimator at the LHC". In: *Proceedings of the 9th Int. Particle Accelerator Conf.* IPAC2018 (2018). DOI: 10.18429/JACOW-IPAC2018-THPAF035. URL: http://jacow.org/ipac2018/doi/JACoW-IPAC2018-THPAF035.html.

[71] A Kurtulus et al. *LHC Collimators Tune Shift Measurements and the Modelling of Collimator Impedances.* 2022. URL: https://indico.cern.ch/event/1224097/#4-modeling-of-collimator-imped.

[72] Rogelio Tomás. "Direct Measurement of Resonance Driving Terms in the Super Proton Synchrotron (SPS) of CERN Using Beam Position Monitors". PhD Thesis. 2003. URL: http://cds.cern.ch/record/615164.

[73] Helmut Wiedemann. *Particle accelerator physics*. 2nd ed. Berlin ; New York: Springer, 1999.

[74] Joschua Dilly et al. "First operational dodecapole correction in the LHC". In: *Physical Review Accelerators and Beams* 26.12 (2023). DOI: 10.1103/PhysRevAccelBeams.26.121001. URL: https://link.aps.org/doi/10.1103/PhysRevAccelBeams.26.121001.

[75] Mael Le Garrec et al. "Measurement and modelling of decapole errors in the LHC from beam-based studies". In: *IPAC'23*. Venice, Italy, 2023. DOI: 10.18429/JACOW-IPAC2023-MOPL024. URL: https://jacow.org/ipac2023/doi/jacow-ipac2023-mopl024.

[76] Mael Le Garrec et al. "First measurement of fourth and fifth order chromaticity in the LHC". In: *IPAC'23*. Venice, Italy, 2023. DOI: 10.18429/JACOW-IPAC2023-MOPL027. URL: https://jacow.org/ipac2023/doi/jacow-ipac2023-mopl027.

[77] Tobias Persson et al. "LHC Optics Commissioning in 2023 and 2024". In: *IPAC'24*. Nashville, Tennessee, USA, 2024.

[78] Vittorio Ferrentino et al. "LHC 2023 Ion Optics Commissioning". In: *IPAC'24*. Nashville, Tennessee, USA, 2024.

[79] Sasha J. Horney et al. "Sextupole RDTs in The LHC at Injection and in the Ramp". In: *IPAC'24*. Nashville, Tennessee, USA, 2024.

[80] Tuuli Nissinen et al. "LHC Optics Measurements from Transverse Damper for the High Intensity Frontier". In: 2023. DOI: 10.18429/JACOW-HB2023-THBP14. URL: https://jacow.org/hb2023/doi/JACoW-HB2023-THBP14.html.

[81] Rogelio Tomás García et al. "Optics for Landau Damping with Minimized Octupolar Resonances in the LHC". In: 2023. DOI: 10.18429/JACOW-HB2023-THBP20. URL: https://jacow.org/hb2023/doi/JACoW-HB2023-THBP20.html.

[82] Jacqueline Keintzel et al. "60° phase advance optics measurements in the Large Hadron Collider at CERN". In: *IPAC'23*. Venice, Italy, 2023. DOI: 10.18429/JACOW-IPAC2023-MOPL026. URL: https://jacow.org/ipac2023/doi/jacow-ipac2023-mopl026.

[83] Felix Carlier et al. "Challenges of K-modulation measurements in the LHC Run 3". In: *IPAC'23*. Venice, Italy, 2023. DOI: 10.18429/JACOW-IPAC2023-MOPL014. URL: https://jacow.org/ipac2023/doi/jacow-ipac2023-mopl014.

[84] Felix Carlier et al. "LHC Run 3 optics corrections". In: *IPAC'23*. Venice, Italy, 2023. DOI: 10.18429/JACOW-IPAC2023-MOPL015. URL: https://jacow.org/ipac2023/doi/jacow-ipac2023-mopl015.

[85] Elena Fol et al. "Experimental Demonstration of Machine Learning Application in LHC Optics Commissioning". In: *Proc. 13th Int. Part. Accel. Conf. IPAC22*. Vol. IPAC2022. Bangkok, Thailand: JACoW, 2022. DOI: 10.18429/JACOW-IPAC2022-MOPOPT047.

[86] Tobias Persson et al. "Optics Correction Strategy for Run 3 of the LHC". In: *Proc. 13th Int. Part. Accel. Conf. IPAC22*. Vol. IPAC2022. Bangkok, Thailand: JACoW, 2022. DOI: 10.18429/JACOW-IPAC2022-WEPOST008.

[87] Tobias Persson et al. "Optics Measurements and Correction Plans for the HL-LHC". In: *IPAC'21*. Campinas, Brazil: JACOW Publishing, Geneva, Switzerland, 2021. DOI: 10.18429/JACoW-IPAC2021-WEPAB026. URL: https://accelconf.web.cern.ch/ipac2021/doi/JACoW-IPAC2021-WEPAB026.html.

[88] Tobias Persson et al. "Optics Correction Strategy for Run 3 of the LHC". In: *IPAC'21*. Campinas, Brazil: JACOW Publishing, Geneva, Switzerland, 2021. DOI: 10.18429/JACoW-IPAC2021-WEPAB027. URL: https://accelconf.web.cern.ch/ipac2021/doi/JACoW-IPAC2021-WEPAB027.html.

[89] Ewen Maclean et al. "Optics Measurement by Excitation of Betatron Oscillations in the CERN PSB". In: *IPAC'21*. Campinas, Brazil: JACOW Publishing, Geneva, Switzerland, 2021. DOI: 10.18429/JACoW-IPAC2021-THPAB168.

[90] Maël Le Garrec et al. *MD6864 — Decapole studies at injection*. Accelerators & Technology Sector Note CERN-ACC-NOTE-2023-0018. CERN, 2023. URL: https://cds.cern.ch/record/2879070.

[91] Xavier Buffat et al. *Optics Measurement and Correction Strategies for HL-LHC*. Accelerators & Technology Sector Note CERN-ACC-2022-0004. CERN, 2022. URL: https://cds.cern.ch/record/2808650.

[92] O. Aberle et al. *High-Luminosity Large Hadron Collider (HL-LHC): Technical Design Report*. CERN Yellow Reports: Monographs CERN-2020-010. Geneva: CERN, 2020. DOI: 10.23731/CYRM-2020-0010. URL: https://cds.cern.ch/record/2749422.

[93] Maël Le Garrec. *Correction of Decapolar Resonances in the LHC*. Goethe Universität, Frankfurt, 2023.

[94] Maël Le Garrec. *Les champs décapolaires du LHC*. Roscoff, France, 2023. URL: https://indico.ijclab.in2p3.fr/event/9312/contributions/30982/.

List of Publications

Journal Publications (co-author)

(1) Ewen H. Maclean et al. "Prospects for beam-based study of dodecapole nonlinearities in the CERN High-Luminosity Large Hadron Collider". In: *The European Physical Journal Plus* 137.11 (2022). DOI: 10.1140/epjp/s13360-022-03367-2. URL: https://link.springer.com/10.1140/epjp/s13360-022-03367-2

(2) Joschua Dilly et al. "First operational dodecapole correction in the LHC". in: *Physical Review Accelerators and Beams* 26.12 (2023). DOI: 10.1103/PhysRevAccelBeams.26.121001. URL: https://link.aps.org/doi/10.1103/PhysRevAccelBeams.26.121001

Conference Proceedings

(1) Mael Le Garrec et al. "Measurement and modelling of decapole errors in the LHC from beam-based studies". In: *IPAC'23*. Venice, Italy, 2023. DOI: 10.18429/JACOW-IPAC2023-MOPL024. URL: https://jacow.org/ipac2023/doi/jacow-ipac2023-mopl024

(2) Mael Le Garrec et al. "First measurement of fourth and fifth order chromaticity in the LHC". in: *IPAC'23*. Venice, Italy, 2023. DOI: 10.18429/JACOW-IPAC2023-MOPL027. URL: https://jacow.org/ipac2023/doi/jacow-ipac2023-mopl027

Conference Proceedings (co-author)

(1) Tobias Persson et al. "LHC Optics Commissioning in 2023 and 2024". In: *IPAC'24*. Nashville, Tennessee, USA, 2024

(2) Vittorio Ferrentino et al. "LHC 2023 Ion Optics Commissioning". In: *IPAC'24*. Nashville, Tennessee, USA, 2024

(3) Sasha J. Horney et al. "Sextupole RDTs in The LHC at Injection and in the Ramp". In: *IPAC'24*. Nashville, Tennessee, USA, 2024

(4) Tuuli Nissinen et al. "LHC Optics Measurements from Transverse Damper for the High Intensity Frontier". In: 2023. DOI: 10.18429/JACOW-HB2023-THBP14. URL: https://jacow.org/hb2023/doi/JACoW-HB2023-THBP14.html

(5) Rogelio Tomás García et al. "Optics for Landau Damping with Minimized Octupolar Resonances in the LHC". in: 2023. DOI: 10.18429/JACOW-HB2023-THBP20. URL: https://jacow.org/hb2023/doi/JACoW-HB2023-THBP20.html

(6) Jacqueline Keintzel et al. "60° phase advance optics measurements in the Large Hadron Collider at CERN". in: *IPAC'23*. Venice, Italy, 2023. DOI: 10.18429/JACOW-IPAC2023-MOPL026. URL: https://jacow.org/ipac2023/doi/jacow-ipac2023-mopl026

(7) Felix Carlier et al. "Challenges of K-modulation measurements in the LHC Run 3". In: *IPAC'23*. Venice, Italy, 2023. DOI: 10.18429/JACOW-IPAC2023-MOPL014. URL: https://jacow.org/ipac2023/doi/jacow-ipac2023-mopl014

(8) Felix Carlier et al. "LHC Run 3 optics corrections". In: *IPAC'23*. Venice, Italy, 2023. DOI: 10.18429/JACOW-IPAC2023-MOPL015. URL: https://jacow.org/ipac2023/doi/jacow-ipac2023-mopl015

(9) Elena Fol et al. "Experimental Demonstration of Machine Learning Application in LHC Optics Commissioning". In: *Proc. 13th Int. Part. Accel. Conf. IPAC22*. Vol. IPAC2022. Bangkok, Thailand: JACoW, 2022. DOI: 10.18429/JACOW-IPAC2022-MOPOPT047

(10) Tobias Persson et al. "Optics Correction Strategy for Run 3 of the LHC". in: *Proc. 13th Int. Part. Accel. Conf. IPAC22*. Vol. IPAC2022. Bangkok, Thailand: JACoW, 2022. DOI: 10.18429/JACOW-IPAC2022-WEPOST008

(11) Tobias Persson et al. "Optics Measurements and Correction Plans for the HL-LHC". in: *IPAC'21*. Campinas, Brazil: JACOW Publishing, Geneva, Switzerland, 2021. DOI: 10.18429/JACoW-IPAC2021-WEPAB026. URL: https://accelconf.web.cern.ch/ipac2021/doi/JACoW-IPAC2021-WEPAB026.html

(12) Tobias Persson et al. "Optics Correction Strategy for Run 3 of the LHC". in: *IPAC'21*. Campinas, Brazil: JACOW Publishing, Geneva, Switzerland, 2021. DOI: 10.18429/JACoW-IPAC2021-WEPAB027. URL: https://accelconf.web.cern.ch/ipac2021/doi/JACoW-IPAC2021-WEPAB027.html

(13) Ewen Maclean et al. "Optics Measurement by Excitation of Betatron Oscillations in the CERN PSB". in: *IPAC'21*. Campinas, Brazil: JACOW Publishing, Geneva, Switzerland,

2021. DOI: 10.18429/JACoW-IPAC2021-THPAB168

Notes and Reports

(1) Maël Le Garrec et al. *MD6864 — Decapole studies at injection.* Accelerators & Technology Sector Note CERN-ACC-NOTE-2023-0018. CERN, 2023. URL: https://cds.cern.ch/record/2879070

(2) Joschua Dilly and Mael Le Garrec. *On the derivation of Amplitude Detuning and Chromaticity Formulas for Particle Accelerators.* 2023. URL: http://arxiv.org/abs/2301.09132

(3) Xavier Buffat et al. *Optics Measurement and Correction Strategies for HL-LHC.* Accelerators & Technology Sector Note CERN-ACC-2022-0004. CERN, 2022. URL: https://cds.cern.ch/record/2808650

(4) O. Aberle et al. *High-Luminosity Large Hadron Collider (HL-LHC): Technical Design Report.* CERN Yellow Reports: Monographs CERN-2020-010. Geneva: CERN, 2020. DOI: 10.23731/CYRM-2020-0010. URL: https://cds.cern.ch/record/2749422

Seminars and Conferences

(1) Maël Le Garrec. *Correction of Decapolar Resonances in the LHC.* Goethe Universität, Frankfurt, 2023

(2) Maël Le Garrec. *Les champs décapolaires du LHC.* Roscoff, France, 2023. URL: https://indico.ijclab.in2p3.fr/event/9312/contributions/30982/

Curriculum vitæ